Optical Measurements of Strong Radio-Frequency Fields Using Rydberg Atoms

by

Stephanie Anne Miller

A dissertation submitted in partial fulfillment
of the requirements for the degree of
Doctor of Philosophy
(Physics)
in the University of Michigan
2017

Doctoral Committee:

Professor Georg A. Raithel, Chair
Associate Professor Hui Deng
Professor Luming Duan
Professor Alex Kuzmich
Professor Theodore B. Norris

Stephanie A. Miller

samil@umich.edu

ORCID iD: 0000-0001-7944-3979

For those who gave me strength when I didn't have any,

thank you.

ACKNOWLEDGEMENTS

First, I would like to thank my advisor, Georg Raithel, for mentoring me and aiding the development of my scientific intuition and increasing my understanding of atomic physics. His enthusiasm and vast knowledge of the material have been inspirational. I appreciate all the insight he provided when I was tackling experimental difficulties, particularly those which I was initially skeptical about. I will never forget the fixes we did for the vacuum chamber, including fixing the water cooling, moving it between rooms, and drilling into it, all while it was under vacuum.

Next, I would like to thank former members of the Raithel lab, including David Anderson, Sarah Anderson, Andrew Cadotte, Yun-Jhih Chen, Luis Felipe Conclaves, Eric Paradis, Rachel Sapiro, Andrew Schwarzkopf, and Mallory Traxler, all of whom helped me and provided insight and knowledge gained through their experience in the lab. In particular, I would like to thank David for mentoring and working with me both while he was a grad student and after completing his degree. Thank you to Rachel for designing and helping to set up BEC2. Thank you to the current members of the lab: Stephen DiIorio, Lu Ma, Jamie MacLennan, Kaitlin Moore, Eric Peterson, Robert Powel, Andira Ramos, Nithiwadee (Pound) Thaicharoen, and Michael Viray. Showing them how to do various things in the lab solidified my understanding of the material. Specifically, I would like to thank Kaitlin and Pound for continually bouncing ideas back and forth and helping troubleshoot malfunctioning equipment, as well as the lunch and coffee breaks we took to clear our heads. Good luck to Michael in taking over BEC2 with all the quirks that chamber has. Thank you to the

current and former group members who proofread this thesis.

I would like to acknowledge the other researchers who contributed to some of the work included in this thesis. Christopher Holloway and Joshua Gordon from the National Institute of Standards and Technology (NIST), in addition to David Anderson, Andrew Schwarzkopf, Nithiwadee Thaicharoen, and Georg Raithel from the University of Michigan all contributed to the work of Chapter IV. The work of Chapter V includes contributions from David and Georg as well.

Thank you to my committee members Georg Raithel, Hui Deng, Luming Duan, Alex Kuzmich, and Theodore Norris for agreeing to serve on my committee.

A big thank you to my friends Jenna Walrath and Julia Bourg for the endless hours we spent together and all the adventures we had. Additionally, for all the support we provided to each other during the hard times.

To my family for their support and encouragement. Thank you to my sister, Brenda, for reading through my thesis and giving me feedback on such short notice.

Finally, thank you to my fiancé, Patrick Bobek. You helped me keep everything in perspective and take a step back when I really needed it.

TABLE OF CONTENTS

LIST OF FIGURES

Figure

LIST OF TABLES

Table

ABSTRACT

Optical Measurements of Strong Radio-Frequency Fields Using Rydberg Atoms

by

Stephanie Anne Miller

Chair: Georg Raithel

There has recently been an initiative toward establishing atomic measurement standards for field quantities, including radio-frequency, millimeter-wave, and micro-wave electric fields. Current measurement standards are obtained using dipole antennas, which are fundamentally limited in frequency bandwidth (set by the physical size of the antenna) and accuracy (due to the metal perturbing the field during the measurement). Establishing an atomic standard rectifies these problems. My thesis work contributes to an ongoing effort towards establishing the viability of using Rydberg electromagnetically induced transparency (EIT) to perform atom-based measurements of radio-frequency (RF) fields over a wide range of frequencies and field strengths, focusing on strong-field measurements. Rydberg atoms are atoms with an electron excited to a high principal quantum number, resulting in a high sensitivity to an applied field. A model based on Floquet theory is implemented to accurately describe the observed atomic energy level shifts from which information about the field is extracted. Additionally, the effects due to the different electric field domains within the measurement volume are accurately modeled. Absolute atomic measurements of fields up to 296 V/m within a $\pm 0.35\%$ relative uncertainty are demonstrated.

This is the strongest field measured at the time of data publication. Moreover, the uncertainty is over an order of magnitude better than that of current standards.

A vacuum chamber setup that I implemented during my graduate studies is presented and its unique components are detailed. In this chamber, cold-atom samples are generated and Rydberg atoms are optically excited within the ground-state sample. The Rydberg ion detection and imaging procedure are discussed, particularly the high magnification that the system provides. By analyzing the position of the ions, the spatial correlation $g^{(2)}(\mathbf{r})$ of Rydberg-atom distributions can be extracted. Aside from ion detection, EIT is implemented in the cold-atom samples. By measuring the timing of the probe photons exiting the EIT medium, the temporal correlation function $g^{(2)}(\tau)$ can be extracted, yielding information about the timing between two different arbitrary photons. An experimental goal using this setup is to look at $g^{(2)}(\tau)$ in conjunction with $g^{(2)}(\mathbf{r})$ for Rydberg atoms. Progress and preliminary measurements of ion detection and EIT spectra are presented including observed qualitative behaviors.

CHAPTER I

Introduction

Recently, there has been an increased interest in the field of quantum optics. Within this broad field, one particular focus is Rydberg atoms and their applications to many areas. Rydberg atoms are atoms with an electron excited to a high principal quantum number ($n > 10$). Because this electron is far from the ionic core, the atoms have many exaggerated properties that scale with the effective principal quantum number $n^* = n - \delta$ where δ is the quantum defect. Such properties include large sizes [radius $\sim (n^*)^2$], long lifetimes [$\sim (n^*)^3$ to $\sim (n^*)^5$, depending on the angular momentum quantum number ℓ], large polarizabilities [$\sim (n^*)^7$], and large transition electric dipole moments $\sim (n^*)^2$] [7]. The large dipole moments lead to strong atomic responses to electric fields [7, 8]. This sensitivity allows for more precise measurement of atomic properties and quantities.

There have been many studies in quantum optics, including the development of efficient single-photon sources [9, 10] and all-optical quantum processing by manipulation of Rydberg polaritons states [11] using microwaves [12]. While there have been many investigation on interactions between Rydberg atoms [13–15], there has also been interest in investigating the interaction between Rydberg states and radiation fields [7, 16, 17].

A technique that has also increased in recent interest is electromagnetically in-

duced transparency (EIT), and more specifically, EIT using Rydberg atoms, known as Rydberg-EIT [18–20].

EIT is an all-optical technique that results in the transmission of a laser through an atom sample over a small frequency range only when another laser is applied. This thesis considers with two-photon Rydberg-EIT in a ladder configuration. Other types of EIT include three-photon EIT [21], as well as Λ- and V-configuration EIT [22]. The first observation of EIT was in 1991 in a Λ-configuration in strontium [23]. Rydberg-EIT uses two laser beams of different frequencies and significantly different powers applied to an atom sample. When the weak laser that drives the lower transition is applied to the atom sample and the resulting transmission is detected, an absorption curve is seen. However, when the second laser is applied, an increase in transmission of the first beam appears over a small frequency range. This increase is due to the strong coupling of the atomic states; quantum interference of the two excitation amplitudes results in transmission of the lower excitation laser beam.

1.1 Atomic Standard and Vapor Cell Measurements

There has been a push from different scientific groups, particularly those at the National Institute of Standards and Technology (NIST), toward establishing an atomic standard for every fundamental unit of measurement [24–27]. The current accepted standard for measuring electric fields is the use of a dipole antenna (see Fig. 1.1). In order to calibrate the sensor, the field is carefully modeled based on the performance of the RF components and the dipole antenna output is recorded for known distances from the source. Thus, the calibration is very circular: in order to measure a field, an accurate device (*i.e.* the antenna) is needed, but the device is calibrated using a "known" field. Therefore, the accuracy of the two components (the field and the antenna) depend on each other. This circularity is demonstrated in Fig. 1.1. The current accuracy of field measurements is only within about 0.5 dB, corresponding to

$\sim 5\%$ [28, 29].

Aside from this circular calibration problem, the dipole antenna is not a great tool for measuring a field because it is frequency dependent, takes a spatial average over the antenna length, and perturbs the field. The antennas are frequency dependent due to the wavelength of the RF radiation, meaning that different length antennas are used for different frequency ranges. Table 1.1 lists some of the RF bands that are of particular interest [30]. The bands that are shaded indicate frequencies considered in this thesis. In order to measure a range of fields, multiple antennas are needed. Because the antenna spans a few centimeters, an average field value is measured regardless of the frequency being measured. Moreover, the antenna has metallic components near the measurement region, and any metal perturbs the RF field. Thus, all of these features limit the sensitivity and accuracy of measuring an RF electric field.

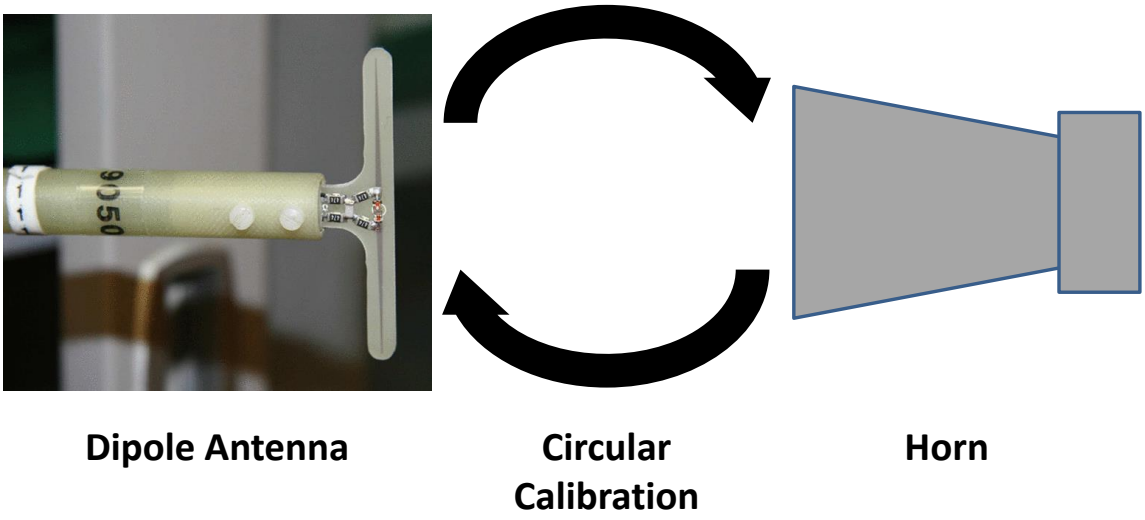

Figure 1.1: Typical dipole antenna used for measuring RF electric fields is shown on the left. This probe is 5 cm long and is used to measure frequencies up to about 2 GHz [1]. A horn antenna is shown on the right, and the arrows between the two represent the circular calibration that occurs (see text for details).

The all-optical technique of using Rydberg atoms and EIT mitigates the problems that using a dipole antenna introduces. Many atomic properties are known with much

greater accuracy than the current electric field standard. Many separate experiments are able to test and measure atomic properties in order to obtain independent, accurate values. Using Rydberg states and transitions provides a wide range of frequency possibilities for field measurements using the same system. Hence, using atoms results in a very broadband tool for measuring fields.

In a room-temperature EIT setup, the atoms are in a vapor cell and focused laser beams are used to probe the atoms, resulting in a very simple experimental setup. The size of the vapor cell and optical beams can be much less than the wavelength of the RF radiation, allowing for sub-wavelength imaging of the RF radiation [4, 31]. Finally, since the atoms are in a glass vapor cell, this eliminates the use of any metal near the measurement region. Thus, the atom-system is non-perturbative to the surrounding field. For these reasons, the all-optical technique of Rydberg-EIT to measure RF electric fields has many advantages over the currently accepted dipole antenna.

The behavior of the Rydberg-EIT line in the presence of an RF field is used to determine the value of the field. Under the application of a weak RF field, the EIT line begins to decrease in amplitude and increase in width. For sufficient RF power, the EIT peak splits into two separate peaks, which is known as Autler-Townes splitting. The separation between the two peaks gives a direct measurement of the Rabi frequency of the RF transition, which is proportional to the applied RF field. This leads to a convenient, calibration-free method of fast RF electric field measurements. When a stronger field is applied, non-linear behavior begins to occur due to higher-order state mixing, resulting in additional peaks and features, as well as complicated spectral structures. This is described theoretically using Floquet spectral maps. In this case, the field is determined by comparison of a measured spectrum with a calculated Floquet spectral map. The theory for both the Autler-Townes and the Floquet regimes is presented in Chapter III.

Band	***Frequency***
HF	3 Hz - 30 MHz
VHF	30 - 300 MHz
UHF	300 MHz - 1 GHz
L	1 - 2 GHz
S	2 -4 GHz
C	4 - 8 GHz
X	8 - 12 GHz
Ku	12 - 18 GHz
K	18 - 27 GHz
Ka	27 - 40 GHz
V	40 - 75 GHz
W	75 - 110 GHz
mm	110 - 300 GHz

Table 1.1: Radio-frequency bands. The bands that considered in this thesis are shaded.

The capabilities and sensitivity of this technique are still being investigated and their range expanded. Currently, fields ranging from ~ 1 mV/m [32] to over 300 V/m [2, 5] have been measured and published, the latter of which is presented in this thesis. Additionally, other properties of RF electric fields including microwave polarization [33], subwavelength imaging [4, 31], and the effect that RF detuning has on spectra in weak fields [34] and very strong fields [35] have also been investigated. In the future, Rydberg-EIT may become the new standard to measure RF electric fields. Rydberg-EIT has also recently been used to measure static electric fields [36] for precise determinations of quantum defects [37].

1.2 Cold Atom EIT

The concept of EIT measurements in a sample of cold atoms has been around for a while [10, 38–40]. Although using a vapor cell is much simpler in terms of experimental setup, as well as much more portable, there are certain advantages of using cold atoms. This includes much narrower linewidths due to the smaller velocity

distribution of the atoms.

This thesis makes use of both vapor-cell and cold-atom EIT to investigate different atomic properties. Previously, the difference between a thermal and a cold-atom sample has been investigated [39]. Some similar measurements are presented in this thesis to ensure the setup used here is understood and all its associated components are functioning as expected.

1.3 Thesis Outline

This thesis can be broken into three main parts: overview and backgroun (Chapters II and III), room-temperature experiments in a vapor cell (Chapters IV and V), and cold-atom-sample experiments in a vacuum chamber (Chapter VI). The overarching tie between the different experiments is the use of EIT under different configurations and applications.

In Chapter II, an overview of the vapor cell experimental setup is given. The equipment, lasers, energy transitions, and other components are described. An introduction to electromagnetically induced transparency (EIT) is given, as well as how the application of RF radiation affects the signal.

Chapter III goes into more detail about the physics and mathematics behind EIT and Autler-Townes splitting. Perturbation theory and Floquet theory are outlined for modeling the experimental spectra that will be presented in later chapters.

In Chapters IV and V, multiple situations are presented where a RF field is applied to an EIT signal. Chapter IV deals with RF at frequencies in the GHz range, driving $|Rydberg\rangle \rightarrow |Rydberg\rangle$ transitions. Moreover, three different regimes are investigated: weak-field regime, intermediate regime, and strong-field regime. Different effects arise in each of these categories which are experimentally investigated and modeled using the methods of Chapter III. One- and two-photon transitions are investigated, as well as transitions involving S, P, and D states. The strong-field

regime is a particular focus of this thesis.

Chapter V also presents measurements and modeling of RF radiation of MHz frequencies applied to an EIT line over a range of field strengths. In this case, the RF modulates the Rydberg state and induces sidebands of the main line. Moreover, the measured fields are strong enough to see substantial mixing with the adjacent fan of hydrogenic states.

Chapter VI shifts focus from room-temperature EIT in a vapor cell to a vacuum chamber setup and the implementation of cold-atom EIT. The cold-atom-sample production in a vacuum chamber is described, and all of the unique features of the chamber are detailed. Cold-atom EIT is discussed in contrast to the vapor cell experiments. Additionally, the field ionization and imaging capabilities of the setup are discussed. This chapter also presents progress in this setup toward utilizing all-optical EIT in conjunction with ion imaging to better understand atom dynamics. In particular, the second-order correlation functions $g^{(2)}(\mathbf{r})$ and $g^{(2)}(\tau)$ are discussed in terms of their implication to the atomic behaviors.

Finally, a summary and outlook for both the vapor cell experiments and the cold-atom setup are presented.

CHAPTER II

EIT Experimental Apparatus and Techniques

Figure 2.1(a) shows the basic setup that can be used to perform RF electric field measurements using electromagnetically induced transparency. A room-temperature cylindrical vapor cell sits at the center of the setup. The cell used for this thesis is 25 mm in diameter and 75 mm long. There are two overlapped, counter-propagating laser beams along the center of the cell that are used to optically excite the Rydberg atoms. They are called the probe and the coupler beam, and they create the EIT window at the proper laser frequencies and powers. Here, the probe is 780 nm and the coupler is 480 nm. The probe beam is the readout beam, and it is much weaker than the coupler beam. The mirror that combines the two optical beams is a dichroic mirror. The probe beam passes through the dichroic mirror and is incident on a photodiode. The signal is then sent to an oscilloscope (sometimes after passing through a lock-in amplifier) where it is then averaged and recorded.

After the EIT peak is seen, an RF electric field is applied to the cell. For the basic setup, this is done with an RF horn, and the distance of the horn from the cell is varied depending on the measurement performed. It is important that the cell is held in place by non-metallic components in order to limit the reflections of the applied radio-frequency radiation.

All of these components, including their importance and variations between ex-

periments, will be discussed in the following sections and chapters. Throughout this thesis, the following terms will be used interchangeably to describe the laser beams: probe/780 nm/red/lower-transition, as well as coupler/480 nm/blue/upper-transition.

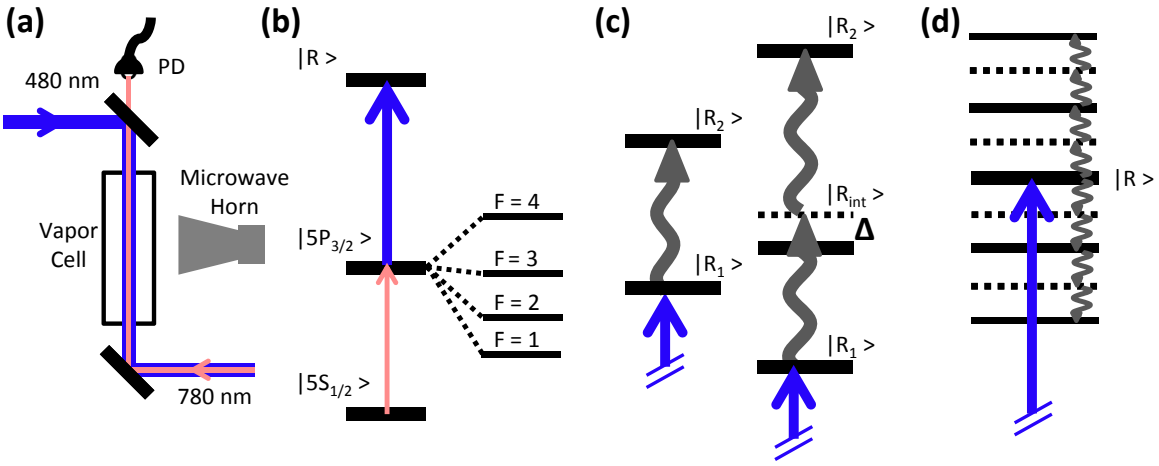

Figure 2.1: (a) Experimental setup (not to scale). (b) Two-photon transition for both the creation of Rydberg atoms and EIT. Hyperfine states of the $|5P_{3/2}\rangle$ are shown for ^{85}Rb. (c) One- and two-photon $|Rydberg\rangle \rightarrow |Rydberg\rangle$ transitions driven with GHz radiation used in Chapter IV. $|R_{int}\rangle$ denotes the intermediate Rydberg state and Δ is the detuning of a microwave photon from $|R_{int}\rangle$. (d) Sidebands created by RF radiation with MHz frequencies used in Chapter V. Note that the energy scales are different between (a)-(c). See Chapters IV and V for more details of the transitions.

2.1 Optical Excitation

For the EIT vapor-cell experiments of this work, 85-rubidium is used since it is the more abundant isotope of rubidium (72%, compared to 28% for ^{87}Rb [41]), resulting in a stronger signal. Although this isotope is used, ^{87}Rb and other elements such as cesium [39, 42, 43] work as well. The energy level diagram for ^{85}Rb can be seen in Fig. 2.1(b). A 780-nm (probe) laser is used for the lower transition $|5S_{1/2}\rangle \rightarrow |5P_{3/2}\rangle$ and a 480-nm (coupling) laser is used to drive the $|5P_{3/2}\rangle \rightarrow |Rydberg\rangle$ transition. Depending on the experiment, either the probe laser is scanned and the coupling laser is locked, or vice versa. Specific cases are discussed as they arise. The lasers that

provide each beam are commercial lasers that can be amplitude and/or frequency modulated with either the laser controls or an acousto-optic modulator (AOM) in the beam path.

The two laser beams are counter-propagating and focused at the same location. Both beams are focused to a waist of $\sim 50-100$ μm at the center of the cell, with the focus of the probe beam slightly smaller than that of the coupling beam so that all of the atoms in the intermediate $|5P_{3/2}\rangle$ state get excited to Rydberg atoms. The power of the 780-nm beam for the lower transition depends on the measurement performed. The power is adjusted to optimize the amplitude of the EIT signal for either the signal strength or sensitivity and is typically only a few micro-Watts. The power for the coupling beam is maximized to a few tens of milli-Watts, also resulting in a stronger EIT signal. Both laser beams are linearly polarized along the same axis. The lasers have a linewidth of ~ 1 MHz. After the vapor cell, the 780-nm beam passes through a dichroic mirror (used to combine the coupling beam with the probe beam) and is incident on a photodiode. The signal from the photodiode is sent to an oscilloscope where it is monitored, averaged, and recorded.

The measurement volume is given by the region in which the beams overlap within the cell. In order to maximize the signal, the beams are exactly overlapping within the cell and optimized once the EIT signal is obtained. However, since the cell is rather large, this results in an averaging of the signal over the length of the cell. This becomes important when an electric field is applied, and it will be discussed in future sections (in particular, Sections 4.2.2 and 4.4).

2.2 Electromagnetically Induced Transparency

Rydberg-EIT occurs when a weak probe beam and a strong coupling beam are on-resonant with the Rydberg transition. This results in two dressed states that are separated in frequency and are symmetric about the probe resonance. The energy

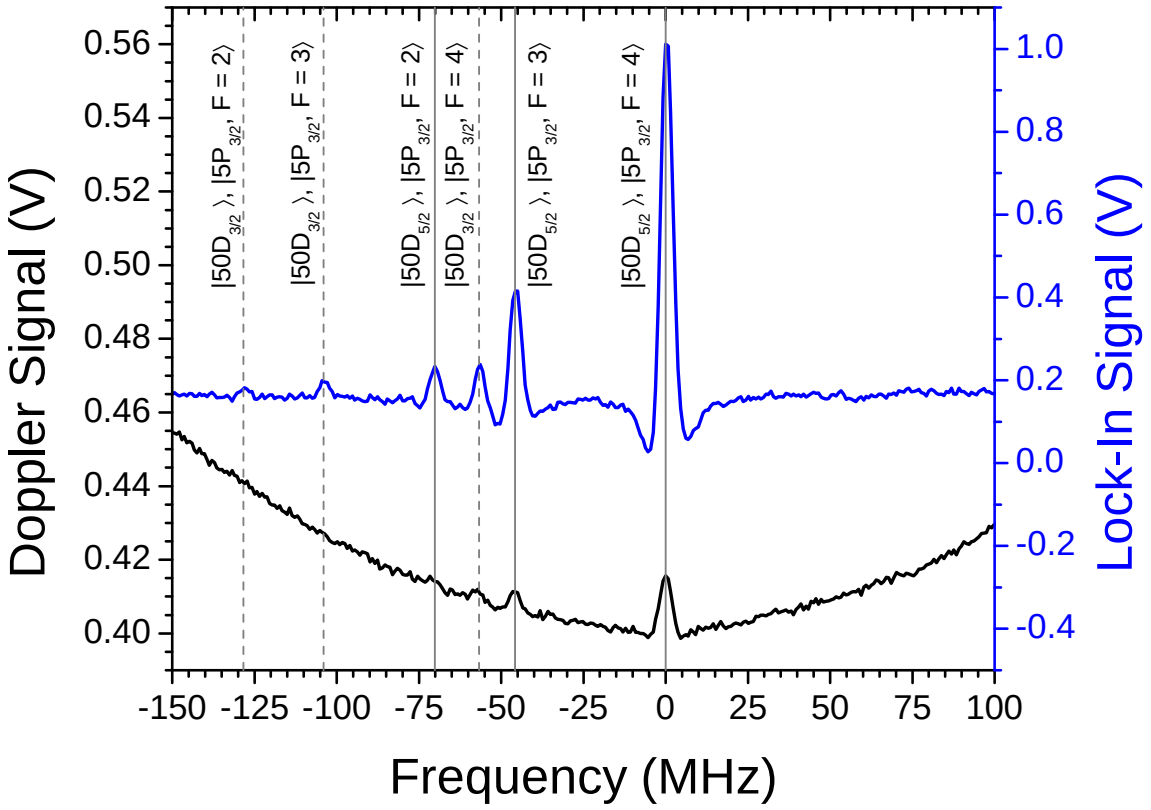

Figure 2.2: EIT signals of the $|50D\rangle$ state with the Doppler background (black curve, left axis) and the signal after a lock-in amplifier (blue curve, right axis). The axes are given in voltage to compare the two curves. Note that the full Doppler profile of the thermal sample (partially shown) for the black curve is much larger in amplitude than the EIT signals shown. See text for more detail about the use of the lock-in. The solid gray lines correspond to the $|50D_{5/2}\rangle$ state and the dashed lines correspond to the $|50D_{3/2}\rangle$ state. For each Rydberg state, the three peaks are for excitation from the $|5P_{3/2}, F = 4, 3, 2\rangle$ hyperfine levels from right to left, respectively. Note that to obtain the correct energy splittings, the corresponding Doppler factor must be applied (see Section 2.2.2). Both signals are averages of 25 traces with ~ 160 nW of probe power and 24 mW of coupler power.

level that is on-resonant for the probe beam becomes "dark," so the probe is transmitted through the atom sample over a small frequency window. Further discussion about EIT and the theory behind it will be given in the next chapter.

For the present case, consider the situation where the probe beam is scanning over the $|5S_{1/2}, F = 3\rangle \rightarrow |5P_{3/2}, F = 4\rangle$ transition. Application of the probe beam without the coupling beam generates a decrease in the amount of light transmitted, which is known as the Doppler profile [44, 45]. This is due to the atom sample having

a thermal distribution. When the coupling beam is turned on and is resonant with the $|5P_{3/2}\rangle \rightarrow |Rydberg\rangle$ transition, a peak appears in the Doppler profile, indicating an increase in the probe transmission. This is known as the electromagnetically induced transparency window. Figure 2.2 shows two EIT curves for the $|50D\rangle$ state. The black curve (left axis) shows the EIT peaks against the Doppler profile of the thermal sample. The blue curve (right axis) shows the same signal going through a lock-in (see Section 2.2.3).

One requirement for this window to occur is that the probe beam must be significantly weaker than the coupling beam. Ideally, the probe beam has an intensity less than one I_{sat} so that full absorption of the probe beam is achieved without the presence of the coupler beam. The coupling beam often has as much power as the experimental setup allows, at least in the experiments presented here.

The EIT linewidth is typically quoted as $(\Omega_c^2 + \Omega_p^2)/\Gamma_2 \approx \Omega_c^2/\Gamma_2$ where $\Omega_{p,c}$ are the Rabi frequencies of the probe and coupling beams (respectively), and Γ_2 is the decay rate of the intermediate state [10]. The approximation is made because the coupling Rabi frequency is usually much greater than that of the probe. However, this equation is only true for cold atoms at low Rabi frequencies. There does not appear to be a clear scaling for both room-temperature and cold-atom EIT over a range of Rabi frequencies. Despite this, the linewidth is greater for larger Rabi frequencies, as well as being larger for thermal samples than cold samples.

2.2.1 Frequency Reference and Laser Locking

As mentioned above, either the probe or the coupling laser is locked while the other is scanned across the Rydberg transition. This is done in order to easily record a spectrum over a frequency range. However, a known frequency reference is needed for the scans in order to calibrate from time (given on the oscilloscope) to frequency. Additionally, there is a slight drift in the laser frequency over time, so the frequency

marker provides a reference point for each scan.

In the experiments of Chapter IV, the probe laser is scanned and the coupling laser is locked. In contrast, the experiments of Chapter V use a locked probe laser and scanned coupling laser. Finally, in Chapter VI, the probe laser is once again scanned while the coupling laser is locked. However, in the last situation, the setup and methods are significantly different than the other two chapters and will be discussed then.

For the probe laser, part of the beam gets split off before the fiber leading to the EIT setup. This component is used for a saturation spectroscopy setup [44, 46]. When the probe is scanned, all of the hyperfine levels, as well as the crossover peaks, of the lower transition ($|5S_{1/2}, F = 3\rangle \rightarrow |5P_{3/2}, F' = 2, 3, 4\rangle$) are seen. This signal is sent to the oscilloscope to be recorded simultaneously with each EIT signal. The splitting of the hyperfine states is known [41], giving the frequency calibration. The traces of the saturation spectroscopy peaks are shifted to line up with each other from scan to scan, and each corresponding EIT scan is shifted by the same amount to account for any laser frequency drift over the course of the experimental measurements. This results in cleaner spectral maps with less jitter and correct level shifts in frequency when looking at the spectral map. There is still a slight frequency drift due to the blue laser over time, but it is much less significant than the probe fluctuations. The power of the probe beam is controlled by manually setting the level of the AOM that is located after the saturation spectroscopy setup and before the fiber.

The coupling laser is a frequency-doubled laser from a 960 nm diode to a 480 nm beam output. A small part of the 960-nm beam is sent through a Fabry-Pérot cavity [47]. The laser is locked to one of the transmission peaks of the cavity. By changing the cavity length, the transmission peak shifts in frequency, and in turn controllably tunes the laser frequency.

In the case where the probe laser is locked, the laser frequency is fixed, so the

hyperfine peaks are not available for use as a frequency reference and a substitute is needed. The locked frequency of the probe is chosen to be at the on-resonant with the $|5S_{1/2}, F = 3\rangle \rightarrow |5P_{3/2}, F' = 4\rangle$ transition once the laser passes through the AOM. This selects the atoms that are in the most probable velocity class so the resulting signal is stronger. The transmission peaks of the coupling laser Fabry-Pérot cavity output provide the frequency reference for this situation. The cavity transmission peaks are recorded and used in a similar manner to that of the saturated spectroscopy peaks when the probe is scanned.

For experiments that examine atomic spectra over a small frequency range, either option will work. However, when the frequency range being investigated is a significant fraction of the width of the Doppler profile, the second method is better. If the probe is scanned, the edges of the Doppler profile result in a lower signal strength since fewer atoms are in these velocity classes. Scanning the coupling beam eliminates this issue since the velocity class that produces the strongest signal is selected by locking the probe laser.

2.2.2 Doppler Factor

For every scan, the detected probe beam signal is recorded from the oscilloscope, and the spectral reference is used to convert from time to frequency. However, the atoms in the EIT configuration experience a Doppler mismatch from the frequency difference of the laser beams, resulting in spectral peaks appearing at frequencies other than what is expected. In order to account for this, an additional Doppler factor is needed, and the exact factor depends on which beam is scanned and which peaks are in question (*i.e.* fine structure (FS) or hyperfine structure (HFS) peaks) [18]. The factors are shown in Table 2.1 and their derivations can been seen in Appendix A. For each case, the measured frequency is the correction factor times the actual frequency.

To illustrate implementing the Doppler factor, consider the spectra of Fig. 2.2.

Probe	Coupler	FS	HFS
scanned	locked	$\frac{\lambda_c}{\lambda_p}$	$1 - \frac{\lambda_c}{\lambda_p}$
locked	scanned	1	$\frac{\lambda_p}{\lambda_c} - 1$

Table 2.1: Doppler correction factors for various conditions and states. FS denotes the fine structure states and HFS denotes the hyperfine states. The measured frequency is the correction factor times the actual frequency. The derivations of these factors can be seen in Appendix A

.

The main EIT peak at 0 MHz corresponds to the $|50D_{5/2}\rangle$ state excited through the $|5P_{3/2}, F = 4\rangle$ state. The first peak that is red-detuned corresponds to the $|50D_{5/2}\rangle$ state excited through the $|5P_{3/2}, F = 3\rangle$ state. This frequency separation is known to be 120 MHz. When the Doppler factor is applied, the measured peak is expected to appear at a separation of 120 MHz $\times$ $(1 - \frac{480}{780}) = 46$ MHz, which is indeed where it is seen. The next peak is for the $|50D_{3/2}\rangle$ state excited through the $|5P_{3/2}, F = 4\rangle$ state. The zero-field fine-structure splitting for the $|50D\rangle$ state is 93 MHz, meaning that the apparent peak separation is 93 MHz $\times$ $\frac{480}{780} = 57$ MHz. The true frequency separation of the remaining peaks can be calculated in a similar manner.

Even in the simple case of EIT without the application of RF radiation, the importance of the Doppler factor is seen in understanding what states the spectral peaks correspond to. These peaks are used for additional verification of frequencies and comparison between experimental and calculated spectral maps. For specific measured transitions in this thesis, the auxiliary peaks are sometimes labeled as well.

2.2.3 Lock-In Amplifier and Enhanced Absorption Dips

When looking at the EIT signal against the thermal Doppler background (see the black curve of Fig. 2.2), the peak is relatively small against the background. By putting the PD signal through a lock-in amplifier, the Doppler background is removed from the signal on the oscilloscope. Moreover, by adjusting the settings on

the amplifier, including the sensitivity and frequency filters, the EIT peaks appear stronger. Because of this, the peaks corresponding to $|50D_{3/2}\rangle$ state excited through the $|5P_{3/2}, F = 2, 3\rangle$ become visible. In order to use the lock-in, the coupling laser light is modulated on and off at a rate of tens of kHz with a square pulse having a 50% duty cycle.

A noteworthy feature present in the lock-in signal but not with the Doppler background signal is the appearance of enhanced absorption dips. These are called enhanced absorption dips because they go below the background level (*i.e.* the absorption level without the coupler beam present). The presence of these dips depends on the probe beam power. Figure 2.3 shows the normalized EIT line for the $|26D_{5/2}\rangle$ state excited through the $|5P_{3/2}, F = 2, 3, 4\rangle$ for four different probe powers: 300 nW, 600 nW, 6 μW, and 30 μW. The two lowest powers have the dips present but with different strengths. For the higher powers, the dips disappear, and the line broadens as expected. Additionally, it is of note that the relative height of the EIT peaks corresponding to the $F = 2$ and $F = 3$ hyperfine states is significantly smaller than the main $F = 4$ peak.

Using the lock-in amplifier allows for less probe power to be used while still obtaining a strong signal. For measurements in the weak-field regime, as well as for the use of this technique as an atomic standard, very low probe powers are required in order to achieve high frequency resolution of the EIT line.

For some of the measurements presented in this thesis, the need to have sufficient signals in the strong-RF-field regime (where the EIT signal amplitude is greatly diminished) outweighs the need to have a narrow EIT line.

2.2.4 Broadening Effects

There are multiple effects that cause the EIT line to broaden in frequency. First, the laser linewidths ($\sim$ 1 MHz here) can cause an increase. Second, increasing

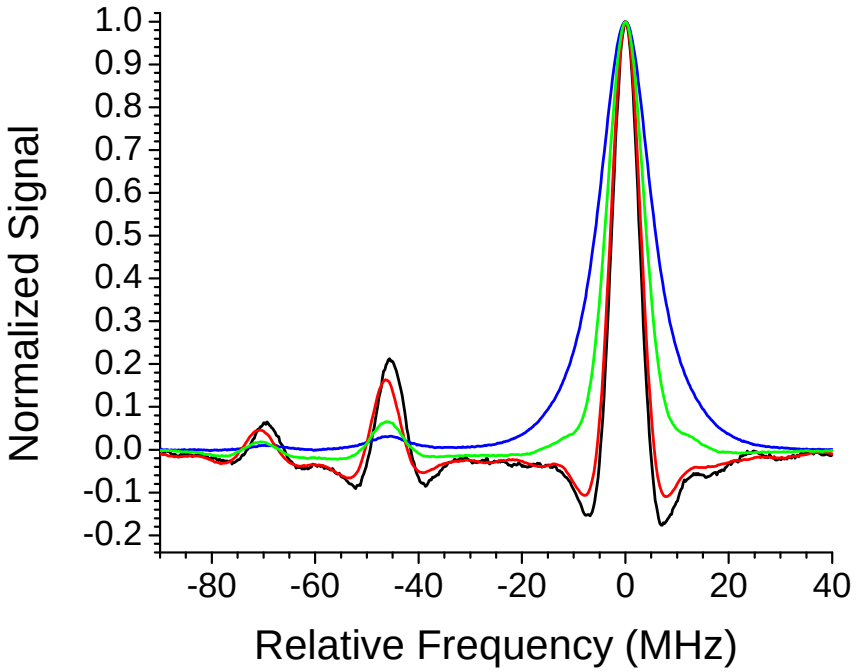

Figure 2.3: Normalized EIT signals vs. frequency for $|26D_{5/2}\rangle$ with probe powers of 300 nW (black), 600 nW (red), 6 μW (green), and 30 μW (blue). From right to left, the peaks correspond to the transitions through the $|5P_{3/2}\rangle$ hyperfine states $F = 4$, $F = 3$, and $F = 2$.

the probe power resulting in power broadening [44], which is sometimes desired for stronger signals. Third, transit-time broadening affects the linewidth due to the finite interaction time an atom has with the radiation field. For the thermal samples at 300 Kelvin, the atoms have a mean velocity of $\langle v \rangle = 273$ m/s. For a beam of diameter $d = 80$ μm, the transit time τ is $d/\langle v \rangle = 293$ ns. This corresponds to a frequency uncertainty of $1/\tau \sim 3$ MHz.

Although all these broadening effects that contribute to the EIT linewidth, the most substantial contribution is due to the drift of the lasers over the course of a data-taking sequence.

More details about broadening effects can be seen in Refs. [45, 48]

2.3 RF Field Application

Throughout this thesis, the RF radiation is created from a commercial source. In some cases, an amplifier is used for stronger fields. The power is adjusted using the source or an attenuator, whichever is applicable to the equipment for the utilized frequency.

One concern for these experiments is reflections from metal surfaces including the cell mount, optics mounts, optics table, and any nearby equipment. To mitigate this effect, only essential components are in the vicinity of the cell, the cell is mounted with materials transparent to RF fields, and RF absorbing foam is placed around the setup, including on the open spaces of the optics table.

In this thesis, three different regimes are investigated: weak-fields, intermediate-fields and strong-fields. These regimes refer to the amount of RF field at the location of the atoms where the measurements are taken. Different effects manifest in the spectral maps of each of these regimes. Moreover, the features that are present are RF-frequency dependent. The regimes are discussed in detail for GHz frequencies in Chapter IV. For these frequencies, two Rydberg states are coupled via the RF radiation, and an example of such a transition is shown in Fig. 2.1(c).

When a RF field is applied to the atom sample, the EIT curve begins to change shape; it begins to decrease in amplitude and increase in width. Figure 2.4(a) illustrates the beginning of this process. For sufficient field strengths (still in the weak-field regime), the EIT line begins to split into two peaks which is known as Autler-Townes (AT) splitting (see Section 3.2). Figure 2.4(b) shows a sample EIT curve without the application of an RF field (black), where there is an RF field applied but the line is not yet split (light blue), and where the two AT peaks are clearly resolved (pink). The separation between these two peaks gives a direct measurement of the applied field and will be discussed in future sections. Fields in the intermediate regime cause higher order mixing and non-linear splitting. Strong fields induce substantial state

mixing.

Chapter V discusses the application of MHz frequencies over a wide range of field strengths, including those above the Inglis-Teller limit [49]. The energy level diagram for this situation is shown in Fig. 2.1(d), where the important spectral feature of RF sidebands is illustrated.

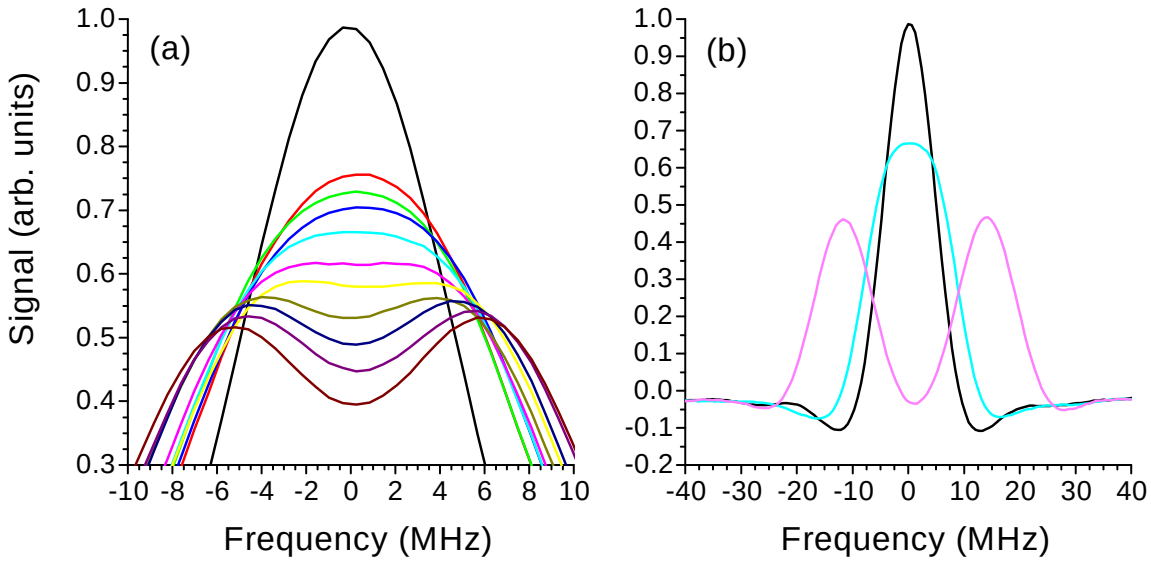

Figure 2.4: Sample normalized spectra showing the (a) emergence and (b) progression of Autler-Townes splitting for an EIT line under the application of a weak RF field. The black curve in both (a) and (b) is an EIT line without the application of any RF radiation. In (b) the light blue curve is with the application of enough RF radiation to cause a visible effect on the line, but not enough to cause any dip [such as that of part (a)]. The pink curve is with even more RF radiation applied to the atoms to create a clear splitting in the EIT line.

2.4 Other Setups

The setup shown in Fig. 2.1 is used for the experiments described in Chapter IV. However, other experiments presented in this thesis use different setups. The experiments in Chapter V apply RF radiation via two metal plates surrounding a room-temperature vapor cell instead of via a horn. This is done in order to generate RF with long wavelengths, as well as to create stronger, more homogeneous fields. The

details of scanning and detection were slightly modified and will be discussed in that chapter.

In contrast to the vapor cell experiments, other measurements are performed in a vacuum chamber with laser-cooled, trapped atoms. This setup will be discussed in Chapter VI.

CHAPTER III

Background

One aim of using the all-optical technique of electromagnetically induced transparency (EIT) is to measure a wide range of RF electric fields. In order to do this, the spectra need to be modeled accurately. In this chapter, the background theory required to model the spectra is presented. In subsequent chapters, specific details in implementing this formalism are discussed in order to account for features of the measured spectra.

Electromagnetically induced transparency (EIT) can be accurately modeled using density matrix equations. When a weak, resonant RF electric field is applied to the system, the EIT line gets split into two peaks whose separation is proportional to the Rabi frequency of the measured RF field. This is known as Autler-Townes splitting [50]. The splitting can be modeled well using a two-level model and perturbation theory.

When sufficiently strong RF fields are applied, the splitting becomes non-linear due to higher-order couplings. Here, perturbation theory becomes invalid and Floquet theory must be used. Floquet theory is an exact means to model the energy levels that result from the application of an RF electric field. Depending on the frequency of the RF radiation, slight modifications of this theory need to be made in terms of the time step and the size of the basis state used in the calculation.

As mentioned in Chapter I, electric fields are measured for RF sources with frequencies ranging from 50 MHz to 130 GHz. Frequencies in the MHz range result in modulation of the Rydberg state since they are far-off-resonant from transitions between Rydberg states in the zero-field condition. RF frequencies in the GHz range drive $|Rydberg\rangle \rightarrow |Rydberg\rangle$ transitions. For now, only consider the latter situation.

3.1 Electromagnetically Induced Transparency (EIT)

EIT can occur in various 3-level atom systems, namely Λ, V, and cascade (or ladder) configurations. The configurations differ in energy of the levels with respect to each other, which in turn affects the decay channels. A comparison of these three types of EIT can be seen in Refs. [22, 51]. The first observation of EIT was in a Λ configuration in strontium [23]. However, it was later found that the EIT signal in a cascade configuration is stronger than that of the other two [51]. In this thesis, only the cascade configuration is used, which can be seen in Fig. 3.1(a). States $|1\rangle$, $|2\rangle$, and $|3\rangle$ correspond to $|5S_{1/2}\rangle$, $|5P_{3/2}\rangle$, and $|Rydberg\rangle$, respectively.

Consider a 3-level atom in a cascade configuration [Fig. 3.1(a)] with a weak probe beam driving the $|1\rangle \rightarrow |2\rangle$ transition. When a strong coupling beam is applied at the $|2\rangle \rightarrow |3\rangle$ transition frequency, these two states mix to form two dressed states close in energy ($|+\rangle$ and $|-\rangle$), as shown in Fig. 3.1(b). The excitation amplitudes from state $|1\rangle$ to each of these dressed states form destructive quantum interference. As a result, the transparency window appears and the probe beam passes through the atom sample. Comparing S and D states, the dipole coupling to the intermediate $|5P_{3/2}\rangle$ state is stronger for D states. Hence, for a given probe power, the amplitude of the EIT signal is stronger for the D state rather than the S state [52].

The density matrix equations that describe EIT have been previously given elsewhere [45, 53, 54] and will not be given here.

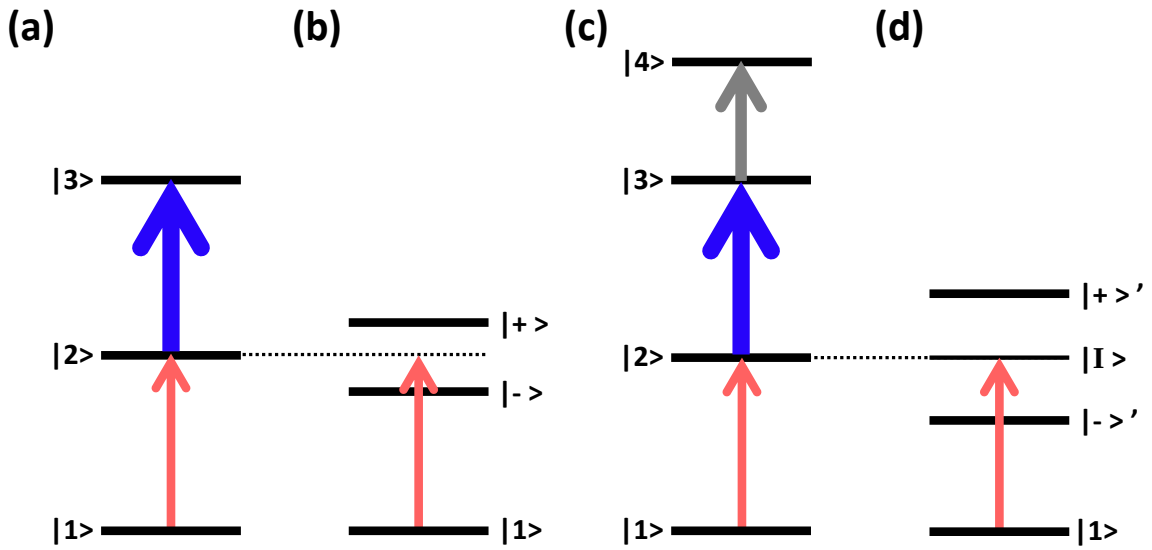

Figure 3.1: (a) Energy level diagram for a 3-level atomic system in a cascade configuration with a weak probe beam (red arrow) and a strong coupling beam (blue arrow). (b) Dressed state picture of part (a). (c) Energy level diagram for a 4-level atomic system with strong coupling between states $|2\rangle$ and $|3\rangle$, as well as between states $|3\rangle$ and $|4\rangle$. (d) Dressed state picture of part (c).

3.2 Autler-Townes Splitting and Perturbation Theory

When RF radiation is applied to the EIT system to couple in an additional state [Fig. 3.1(c)], the interference state $|I\rangle$ results in the dressed state picture [Fig. 3.1(d)]. Constructive interference between the dressed states $|+\rangle'$ and $|-\rangle'$ result in the absorption of the probe beam and the EIT window is split. The separation of the two transparencies is given by the Rabi frequency of the RF field.

In this thesis, degenerate perturbation theory is used to model the measured spectra for an applied RF field in the weak-field regime presented in Chapter IV. In the weak-field regime and for detuning $\delta = 0$, the splitting between the dressed states is linear in field (power) for one-photon (two-photon) RF transitions. The process involves calculating the AC stark shift of the states involved in the RF transition. To

do this, the eigenvalues of the Hamiltonian in the dressed state picture

$$\begin{pmatrix} \delta/2 & \Omega_0/2 \\ \Omega_0/2 & -\delta/2 \end{pmatrix} \tag{3.1}$$

are found to be $\lambda = \pm\frac{1}{2}\sqrt{\delta^2 + \Omega_0^2}$ [44]. Here, δ is the detuning of the RF frequency that couples the two states and Ω_0 is the Rabi frequency of the RF radiation. Thus, the energies of the two dressed states are separated by $\sqrt{\delta^2 + \Omega_0^2}$.

The atomic measurement of the RF field is obtained by determining the separation of the two transparencies that are created. The measured frequency splitting divided by the appropriate Doppler factor is equal to the effective Rabi frequency $\Omega = \sqrt{\delta^2 + \Omega_0^2}$. For most measurements in this thesis, $\delta = 0$. The equation for the electric field is given by

$$E_z = \frac{\hbar\Omega_0}{d_z}. \tag{3.2}$$

The density matrix equations that describe RF dressed states in a 4-level atom system have been previously given elsewhere [53, 54] and will not be given here.

The sensitivity of Rydberg-EIT depends on the ability to resolve the AT splitting. In order to observe the splitting of the EIT peak, a sufficient RF field must be applied to the atoms, and the exact amount depends on various factors. For the weak-field measurements, the amount of RF power required to split the EIT line is of significant concern since one goal is to measure the weakest fields possible. The amount of probe power affects the linewidth of the EIT (see Fig. 2.3). If the EIT line is too broad, a stronger field is required to resolve an AT splitting. One feature that was noted in Chapter II is the appearance of enhanced absorption around the EIT window for low probe beam powers [20]. These enhancements also affect the splitting of the EIT peak since there is an enhanced absorption dip on each side of the AT peaks as well. One possibility that has been shown to extend the sensitivity of this all-optical

measurement technique is measuring the EIT line for a fixed RF power as a function of RF detuning (*i.e.* $\delta \neq 0$) [34]. Further work is being done elsewhere to improve the sensitivity of this all-optical technique.

3.3 Near and Far Field

One thing to consider when applying an electric field to the atom sample is if the measurement volume is in the near field or the far field of the RF source. In the near field of the RF source, the polarization of the field does not have a clear direction. Therefore, instead of driving only the intended transition, other transitions also occur, resulting in additional lines in the spectra.

Another issue with measurements in the near field is electric-field inhomogeneities along the axis of optical-beam propagation. Because the RF field is not yet a plane wave, the wavefront has curvature, so the atoms along the optical beam path experience different values of the electric field. When measuring the probe transmission at the vapor cell output, the resulting transmissions are a result of all of the atoms, so multiple electric field domains are observed in the spectra.

The equation for being in the near-field is

$$d \lesssim \frac{2D^2}{\lambda} \tag{3.3}$$

where d is the beginning of the far-field region, D is the dimension of the radiator, and λ is the wavelength of the RF.

In order to get a clean spectrum, and an accurate measurement of the field, there are two approaches that mitigate field inhomogeneities: being in the far field or using a vapor cell that is smaller than the wavelength of the RF radiation. For weak-field and sensitivity measurements, being in the far field of the horn is not a problem. When it is desirable to measure moderate to strong electric fields, the RF source is

often limited in output power [55]. In order to achieve a stronger field, the source is put adjacent to the cell, which is well within the near-field regime. By having the two components as close to each other as possible, the RF radiation is more directed into the cell because it has not yet spread out in space. For the experiments of this thesis, the desire to reach the strong-field regime outweighed the concerns about effects due to inhomogeneities. Instead, additional peaks in the spectra as a result of multiple electric field values along the measurement volume are modeled as well. The second method of using a small vapor cell works because the measurement volume is smaller, so there are fewer field variations along the optical beam direction. For the measurements of this work, a standard spectroscopic vapor cell was used due to availability.

3.4 Floquet Theory

For sufficiently strong electric fields, perturbation theory is no longer valid because higher-order couplings to other states become significant, and another method must be used to model the spectra. Non-perturbative Floquet theory is used instead. Floquet theory accounts for couplings between many Rydberg states, while allowing for the absorption or emission of an arbitrary number of RF photons during the optical excitation. Spectra that can be modeled well with perturbation theory can also be modeled with Floquet theory (but it is unnecessary in the weak-field case).

Solutions to the time-periodic Schrödinger's equation for $\hat{H}(t) = \hat{H}(t+T)$ where T is the period of the RF field are of the form

$$\Psi_\nu(t) = \mathrm{e}^{-iW_\nu t/\hbar}\psi_\nu(t). \tag{3.4}$$

with quasienergies W_ν and periodic Floquet modes $\psi_\nu(t) = \psi_\nu(t+T)$. The subscript ν is an arbitrary mode label. The Floquet modes are represented using basis states

$|n,l,j,m_j\rangle = |k\rangle$ and time-periodic coefficients $C_{\nu,k}(t)$. This is given by

$$\Psi_\nu(t) = \mathrm{e}^{-iW_\nu t/\hbar} \sum_k C_{\nu,k}(t)|k\rangle. \tag{3.5}$$

The energies and wavefunction (at $t = 0$) are obtained by finding the eigenvalues and vectors of $\hat{U}(t, T + t)$. $C_{\nu,k}(t)$ are then found by integrating the wavefunction over one RF cycle. In order for reasonable completion time, Δt must be chosen just small enough such that $|W_k - W_{k'}|\Delta t/\hbar \leq 2\pi$ holds for all energy differences $W_k - W_{k'}$ for basis states $|k\rangle$ and $|k'\rangle$. If this condition is violated, basis states far away from the states of interest generate aliases in the investigated region, resulting in wrong Floquet spectra. The choice of basis size depends on the field strength and frequency used. For example, the strong-field measurements of Section 4.4 are modeled using a basis of $56 \leq n^* \leq 73$ and $\ell \leq 10$. Additionally, RF photons up to $N = \pm 8$ are used.

The excitation line strengths are computed by Fourier-expanding $C_{\nu,k}(t)$:

$$\Psi_\nu(t) = \mathrm{e}^{-iW_\nu t/\hbar} \sum_k \sum_{N=-\infty}^{\infty} \tilde{C}_{\nu,k,N} \mathrm{e}^{-iN\omega_{RF}t}|k\rangle, \tag{3.6}$$

$$\tilde{C}_{\nu,k,N} = \frac{1}{T}\int_0^T C_{\nu,k}(t)\mathrm{e}^{iN\omega_{RF}t}dt. \tag{3.7}$$

where N is the number of RF photons of frequency ω_{RF} added or subtracted from the microwave field associated with the bare atomic state $|k\rangle$. The Floquet levels are resonantly excited from the $|5P_{3/2}\rangle$ state. The laser frequencies and corresponding line strengths $S_{\nu,N}$ are then given by

$$\begin{aligned} \hbar\omega_{\nu,N} &= W_\nu + N\hbar\omega_{RF} \\ S_{\nu,N} &= (eF_L/\hbar)^2 \left| \sum_k \tilde{C}_{\nu,k,N}\, \hat{\epsilon} \cdot \langle k|\hat{\mathbf{r}}|5P_{3/2}, m_j\rangle \right|^2, \end{aligned} \tag{3.8}$$

Here, F_L is the amplitude of the laser electric field, $\hat{\epsilon}$ is the laser polarization vector,

and $\langle k|\hat{\mathbf{r}}|5P_{3/2}, m_j\rangle$ are the electric-dipole matrix elements of the basis states with $|5P_{3/2}, m_j\rangle$. Since the RF fields are π-polarized, calculations are done separately for the allowed (fixed) m_j-values. Because the coupler-laser excitation is from the $|5P_{3/2}\rangle$ state, $|m_j| = 1/2$ and $3/2$ are allowed (the sign is irrelevant). Each Floquet level W_ν leads to multiple resonances which are associated with the microwave photon number N. A similar procedure is used by Yoshida et al. [56].

3.4.1 RF Radiation of MHz Frequencies

When smaller RF frequencies are used (*i.e.* those in the MHz range), the above formalism still holds. However, modifications in the basis size need to be made. The information in this section is specific to the work in Chapter V where RF radiation with MHz frequencies is applied to Rydberg states. Radiation of this frequency does not couple two Rydberg states in weak fields, but it instead introduce sidebands to the main line. In this work, a strong enough field is applied to couple in the adjacent fan of hydrogenic states.

Each Floquet level (energy W_ν) carries RF-dressed sidebands in the spectrum, which are associated with the exchange of a number of N RF photons during the excitation. A large enough basis $\{|k\rangle\}$ must be chosen to cover important couplings to accessible states. However, it must also be small enough for the calculation to be completed within a reasonable amount of time. Because of the mixing with the hydrogenic states, all possible values of ℓ and j [*i.e.* $\ell = 0, ..., n-1$ and $j = \ell \pm 1/2$ (for $\ell = 0$ only $j = 1/2$) are included in the basis]. For the spectra presented in Chapter V, the basis can be limited to states with energies corresponding to effective principal quantum numbers $55.05 \leq n^* \leq 57.95$ and 20 RF photons.

3.5 Comparing Experimental and Calculated Spectra

In the following chapters, experimental spectra are primarily given in dBm since that is the unit given by the RF source. Energy levels are calculated using either perturbation theory or Floquet theory and the calculated spectral maps are obtained. Units of the calculation are either given in V/m or dBi, as appropriate for the situation. Here, 1 dBi $= 10\log_{10}[I/I_0]$ where I_0 is typically 1 W/m^2. By overlaying the experimental and calculated maps, the true value of the measured field can be determined. In some measurements presented, the error is given by half the experimental step size due to the coarse interval.

For the measurements of Chapter V, the errors in power (in Watts) are given by

$$\frac{\Delta I}{I} = \frac{10^{P'/10} - 10^{P/10}}{10^{P/10}} \times 100\% \tag{3.9}$$

where P is the maximum power (in dBi) reached. P' is the maximum power (in dBi) that is visually acceptable by shifting the calculated spectral map to the left with respect to the experimental map. Note that $P < P'$. The uncertainty in field is approximately half the uncertainty of power since $P \propto E^2$. Alternatively, the error for field is given by

$$\frac{\Delta E}{E} = \frac{10^{P'/20} - 10^{P/20}}{10^{P/20}} \times 100\%. \tag{3.10}$$

This method of comparison gives the upper bounds on the error based on visual comparison of the experimental and calculated spectral maps. If a greater precision is needed, then an algorithm could be written to mathematically compare the overlap of the maps. This could be done by implementing the cross-correlation between the experimental and calculated spectral maps.

CHAPTER IV

Microwave and Millimeter Wave Measurements

The work discussed in this chapter consists of material published in Refs. [3] and [2]

One of the main goals of measuring Rydberg-EIT lines under the application of RF electric fields (E-fields) is to use this all-optical technique to replace antenna-based detectors used for this application. When a radio-frequency field is applied to an EIT line, the line will shift and possibly split depending on the RF power. In this chapter, three different field regimes are investigated experimentally and modeled theoretically. First, there is the weak-field regime where the EIT line undergoes Autler-Townes (AT) splitting and perturbation theory is valid. Next, there is the intermediate regime where the coupling to other states becomes important and perturbation theory begins to become inadequate. Finally, there is the strong-field regime where there is strong coupling to other states and Floquet theory must be used. For all regimes there are field inhomogeneities in the setup, an issue that is discussed and quantified for each situation. All of the measurements of this chapter are for $|Rydberg\rangle \rightarrow |Rydberg\rangle$ transitions driven by RF fields with GHz frequencies. Both one- and two-photon RF transitions are investigated. Throughout these sections, "RF" refers to microwave (MW) and millimeter (mm) waves. The measurements presented in this chapter demonstrate a subset of the capabilities of this measurement technique and act as a

proof-of-principle over a wide range of field strengths.

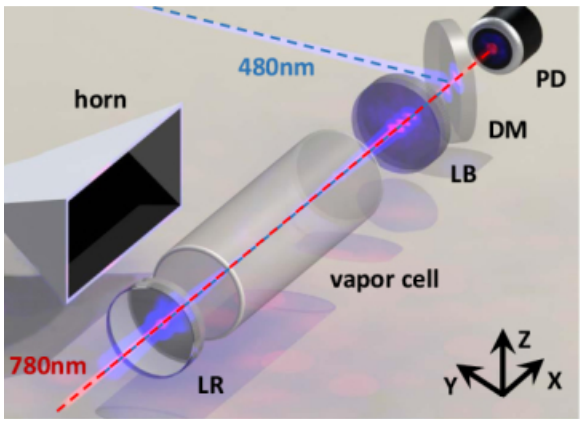

Figure 4.1: Illustration of the experimental setup showing the vapor cell, 480-nm and 780-nm laser beams (dashed lines), photodiode (PD), blue lens (LB), red lens (LR), dichroic mirror (DM), and microwave horn. [2]

4.1 Setup

The experimental setup is shown in Fig. 4.1, and is the same as the basic setup shown in Fig. 2.1(a). Only details about the setup that are specific to this chapter are given here.

Both the probe beam and coupling beam are linearly polarized and focused at the center of the cell. The probe laser is scanned over the $|5S_{1/2}, F = 3\rangle \rightarrow |5P_{3/2}, F = 4\rangle$ transition at a $\sim$ 1 Hz repetition rate and detected on a single photodiode. The coupling laser frequency is fixed near a $|5P_{3/2}, F = 4\rangle \rightarrow |Rydberg\rangle$ transition, and the intensity is modulated with a square wave at a rate of tens of kHz and a 50% duty cycle.

Microwaves are produced by a signal generator and are emitted from a horn. The microwaves are linearly polarized parallel to the optical-beam polarization. For these experiments, the RF field drives $|Rydberg\rangle \rightarrow |Rydberg\rangle$ transitions [Fig. 2.1(b)]. The distance between the horn and the atoms is varied to access the different field regimes. For the low-field measurements, the horn is in the far field of the cell (tens of

centimeters from the optical beams). For the intermediate-field and the strong-field measurements, the horn is placed adjacent to the cell.

4.2 Weak-Field Regime

In the weak-field regime, when RF power is applied to the atoms in the EIT configuration, the atoms undergo Autler-Townes splitting. Here, the EIT line splits linearly and the spectra can be modeled with perturbation theory. For more details, see Section 3.2.

4.2.1 One-Photon Transition

A Rydberg-EIT spectrum for the $|62S_{1/2}\rangle$ Rydberg state (without the application of microwaves) is shown in the top panel of Fig. 4.2(a). The plot is centered on the EIT signal of the $|5P_{3/2}, F = 4\rangle$ hyperfine state. The smaller peak at about -48 MHz is an EIT signal of the $|5P_{3/2}, F = 3\rangle$ hyperfine state. The central EIT resonance has a linewidth of $2\pi \times (3.4 \pm 0.3)$ MHz.

First, the one-photon $|62S_{1/2}\rangle \rightarrow |62P_{3/2}\rangle$ transition is driven with the microwave source set at $\nu_{MW} = 15.590464$ GHz, which is within 1 MHz of the calculated transition frequency (using the quantum defects from [7]). For this transition, the calculated electric dipole matrix element $d_z = 1854ea_0$ (with $m_j = 1/2$ for both states). Figure 4.2(a) shows a series of Rydberg-EIT spectra for this transition for increasing MW powers from top to bottom. As the power is increased, the EIT resonance is split into two symmetric EIT-AT peaks. Since the probe laser is scanned and the MW is effectively on-resonance, the separation of the two peaks is given by $\lambda_c/\lambda_p \times \Omega_{RF}$ where Ω_{RF} is the Rabi frequency of the microwaves (see Section 3.2).

The AT peaks become broader as the MW power is increased. Since the cell is a few inches long, atoms at different points along the path experience different field strengths. The detected EIT-AT signal is the result of all of the atoms in these

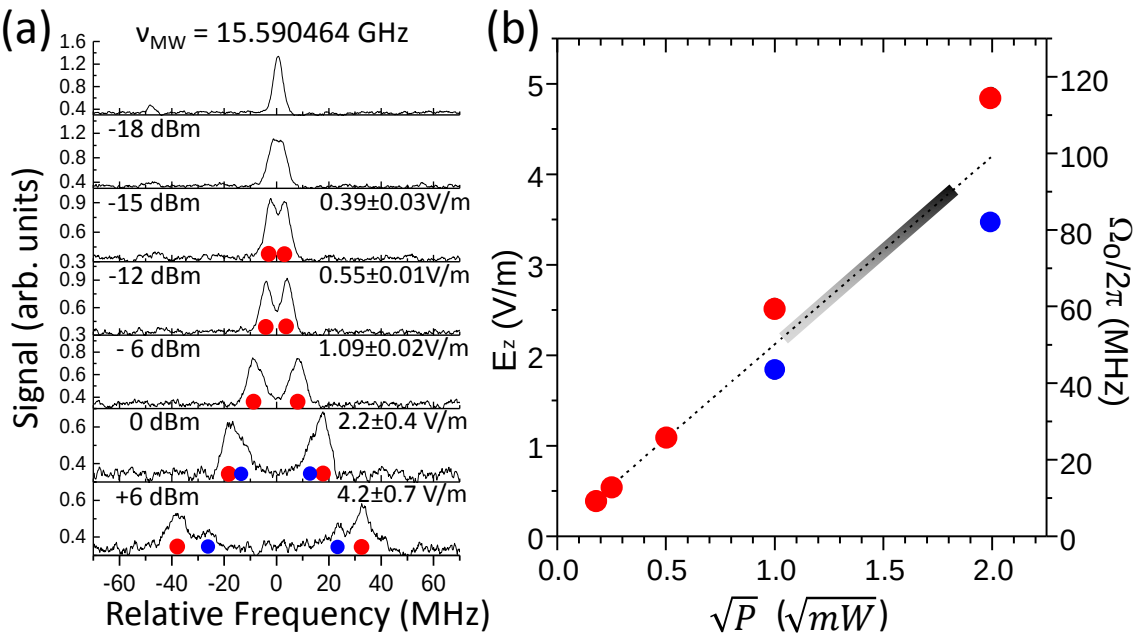

Figure 4.2: (a) Rydberg EIT-AT spectra for the one-photon $|62S_{1/2}\rangle \rightarrow |62P_{3/2}\rangle$ Rydberg transition for increasing microwave power (top to bottom). (b) Measured Rabi frequency and electric field strength for the inner (blue) and outer (red) maxima of (a) are plotted versus the square root of applied microwave power. Line centers are determined by Gaussian fits to the peaks. Uncertainty bars, given by the fit error, are smaller than the data points. The dashed line is a linear fit to the average measured field strength. The shaded region indicates the microwave field range for the $|62S_{1/2}\rangle \rightarrow |63S_{1/2}\rangle$ measurement in Fig. 4.5. [3]

different fields. The field inhomogeneity manifests as broadening and additional peaks in the spectra. This issue will become particularly important in Section 4.4 and will be discussed in more detail. At the highest powers in Fig. 4.2(a) there are two peaks, indicated by red and blue circles. These are attributed to local maxima within the cell (see Ref. [4] for example).

Figure 4.2(b) shows the average electric field (and Rabi frequency) measured from Fig. 4.2(a) as a function of the square root of microwave power. The values determined from the local maxima are noted by the circles and the dashed line is a fit to the average field. The uncertainty of each data point (given by the AT peak fit) is smaller than the plotted data point. However, the uncertainty in the field strength is estimated to be ±15%. As expected for a one-photon transition, the electric field

scales linearly as the square root of microwave power (recall Eqn. 3.2: $E_z = \Omega_0\hbar/d_z$).

Field-induced state mixing must generally be considered in the interpretation of Figs. 4.2(a) and (b). Floquet calculations show that the electric dipole moment of the $|62S_{1/2}\rangle \rightarrow |62P_{3/2}\rangle$ transition drops by $\sim 6\%$ from its zero-field value of $d = 1854ea_0$ over the measured field range in Fig. 4.2(a). Accounting for this would result in a slight nonlinear correction to the electric-field axis of Fig. 4.2(b). For the spectra presented here, this effect is ignored since it is less than the electric-field uncertainty.

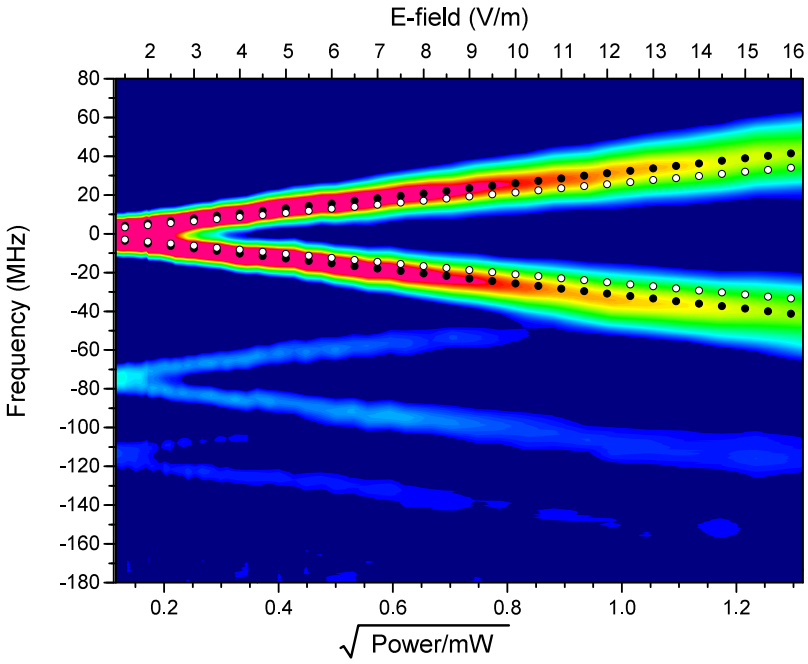

Figure 4.3: Experimental spectra of the one-photon $|26D_{5/2}\rangle \rightarrow |27P_{3/2}\rangle$ transition driven by 132.6495 GHz mm-waves in the weak-field regime plotted versus $\sqrt{\text{Power/mW}}$. Each spectrum is an average of 25 traces, and the signal is represented on a color scale from 0 to 1.25 in arbitrary units. A calculated spectrum is overlaid with relative excitation rates from $|5P_{3/2}, m_j = 1/2$ (black) and $3/2$ (white)$\rangle$, given by the dot areas, and electric-field values on the top axis. [2]

As previously mentioned, this technique is not unique to a specific state or transition. Figure 4.3 shows the $|26D_{5/2}\rangle \rightarrow |27P_{3/2}\rangle$ microwave transition driven by 132.6495 GHz, which is in the WR-6 band (see Table 1.1). The dominant AT pair in the spectrum corresponds to the $|5P_{3/2}, F = 4\rangle$ state. The faint level pairs centered at -74 and -113 MHz correspond to spectra associated with the intermediate

$|5P_{3/2}, F = 3, 2\rangle$ hyperfine components, respectively. These values are different than what was plotted in Chapter II because the measured frequency of the spectra plotted in Fig. 4.3 are scaled by λ_p/λ_c to match the true frequency of the levels of interest.

A noticeable broadening of the $|5P_{3/2}, F = 4\rangle$ state occurs at higher microwave powers due to the degeneracy of the $|m_j|$ components being lifted. Using the known values for the dipole moments ($405ea_0$ for $|m_j| = 1/2$ and $331ea_0$ for $|m_j| = 3/2$), a maximum field of 16 V/m is reached experimentally. The microwave ionization limits for Rydberg states is known [7]. A field of 16 V/m is only 0.02% of the ionization limit, reiterating that this measurement is well within the weak-field regime. These two transitions show that the technique of measuring electric fields using Rydberg-EIT is applicable to multiple RF frequencies over a wide range of Rydberg states.

4.2.2 Inhomogeneity

One issue that is apparent even in the weak-field regime is inhomogeneity in the electric field, and there are multiple causes for this. First, some of the measurements that will be presented are taken in the near-field, where the field is not a pure plane wave (see Sec. 3.3). Another contributing factor contributing to the inhomogeneity is the dielectric cell [57]. When the wavelength of the RF radiation is small, standing waves are created in the cell. Multiple regions are sampled if one or more of the following are true: if the beams are at a slight angle with respect to the cell, if the horn is at a slight angle with respect to the cell, or if the beams are larger than $\lambda_{RF}/2$. To illustrate the standing waves, Fig. 4.4 is a simulation of the $|E|$ field of 104.77 GHz radiation ($\lambda = 2.86$ mm) incident on a 25 mm cell. This figure is in the plane through the center of the cell with the field incident from the right. Standing waves are visible within the cell, as well as inhomogeneous regions at the edges. Even for small beams, inhomogeneity effects due to the edge of the cell are present, so any beam traveling through the cell experiences variations along both the longitudinal

and transverse directions.

These effects also explain why there is more inhomogeneity seen in the spectra of Fig. 4.2 than in Fig. 4.3. These two sets of measurements were taken at separate times and minor modifications were made between the sets. The alignment (*i.e.* the angle of the optical beams and/or the horn with respect to the cell) was slightly better for the $|26D_{5/2}\rangle \rightarrow |27P_{3/2}\rangle$ case, so there were fewer inhomogeneities.

In future measurements, the inhomogeneity effects could be reduced by using cells that are smaller than the RF wavelength. Currently, other groups are working on developing smaller cells [58], as well as hollow-core fibers [59, 60], for this purpose. One drawback of using a smaller cell is a reduced signal strength due to the lower number of atoms within the cell. One thing that mitigates this effect is heating the cell because this increases the vapor pressure [41]. This technique is being implemented, but it also introduces its own issues [61].

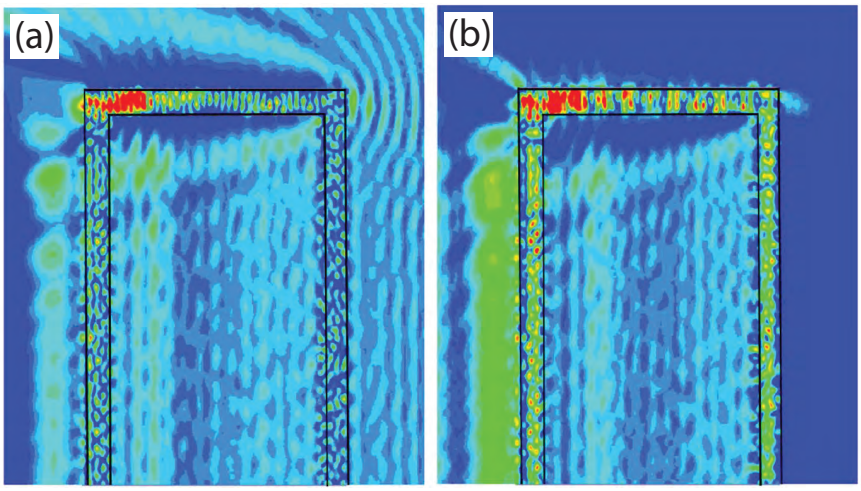

Figure 4.4: Simulation of electric-field amplitude $|E|$ for a plane wave of 104.77 GHz radiation incident onto a 25 mm diameter vapor cell from the right: (a) incident + scattered, and (b) scattered. The region shown in the figure is a horizontal planar cut through the center of the cell, with half of the cell shown. The electric field is on a linear colorscale ranging from 0.7 V/m (blue) to 5 V/m (red). [4]

4.2.3 Two-Photon Transition

The investigation of the one-photon $|62S_{1/2}\rangle \rightarrow |62P_{3/2}\rangle$ transition is extended to investigate the two-photon $|62S_{1/2}\rangle \rightarrow |63S_{1/2}\rangle$ transition. This transition is driven with microwaves of frequency $\nu_{MW} = 15.728909$ GHz and powers over the range indicated by the gray-shaded region in Fig. 4.2(b). This drive frequency is blue detuned by $\delta_{2MW}/2\pi = 10$ MHz, where δ_{2MW} is the detuning from the two-photon MW transition. The resulting spectra can be seen in Fig. 4.5. In this figure, the experimental spectra have been scaled by λ_p/λ_c.

This two-photon transition has the near-resonant intermediate state $|62P_{3/2}\rangle$ which leads to large two-photon Rabi frequencies and considerable state mixing even at small microwave electric-field strengths. The two-photon Rabi frequency can be expressed as $\Omega_{2MW} = \Omega_1\Omega_2/(2\Delta)$, where Ω_1 and Ω_2 are the single photon $|62S_{1/2}\rangle \rightarrow |62P_{3/2}\rangle$ and $|62P_{3/2}\rangle \rightarrow |63S_{1/2}\rangle$ Rabi frequencies, respectively, and Δ is the detuning of the microwave frequency from the $|62P_{3/2}\rangle$ intermediate state. Here, $\Omega_1 \simeq \Omega_2$ to within 3%.

Accounting for the Rabi frequencies and intermediate state detuning, it is calculated that a field of 2.12 to 3.74 V/m is measured for this transition. Since the Rabi frequency has a quadratic dependence on the field, the uncertainty here is $\sim \pm 30\%$.

4.2.4 Modeling

Initially, the energy-level shifts of the two-photon case are modeled using perturbation theory (see Section 3.2), considering off-resonant transitions through the intermediate $|62P_{1/2}\rangle$ and $|62P_{3/2}\rangle$ levels. The levels are detuned from the intermediate state by ∼500 MHz and ∼150 MHz, respectively. The Rabi frequency through the latter state is about a factor of 6 larger than that through the former.

Using second order perturbation theory, the AC stark shifts of the $|62S_{1/2}\rangle$, $|62P_{1/2}\rangle$, $|62P_{3/2}\rangle$, and $|63S_{1/2}\rangle$ states are calculated [62]. The $|62S_{1/2}\rangle$ and $|63S_{1/2}\rangle$

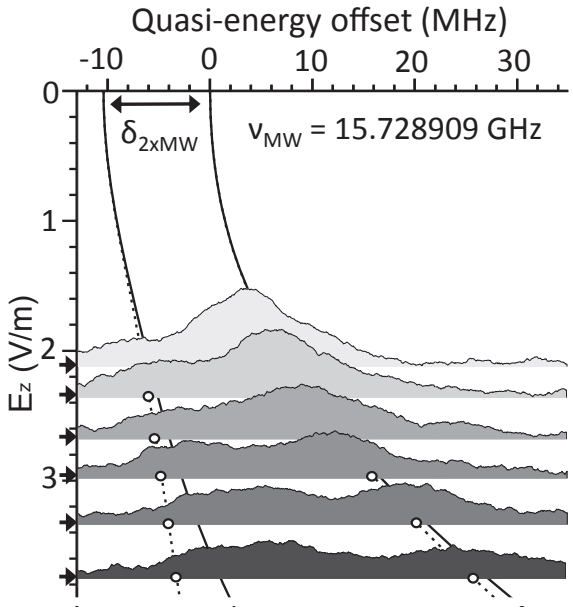

Figure 4.5: $|62S_{1/2}\rangle \rightarrow |63S_{1/2}\rangle$ spectra at average field strengths indicated by the arrows on the left axis. These field values correspond to the fields used in the shaded region of Fig. 4.2(b) for the one-photon transition. State energies obtained from second-order perturbation theory are plotted as a function of average microwave field (solid lines); also plotted are quasi-energies from a Floquet analysis for the $|62S_{1/2}\rangle$ and $|63S_{1/2}\rangle$ state pair (dashed lines). Spectra are averages of 15 traces. Experimental line broadening is due to field-inhomogeneity effects. [3]

energies shift by about +1.34 and +1.40 MHz/(V/m)^2, respectively, resulting in a total differential shift of (0.06 MHz/(V/cm)^2)$\times(E_{RF}^2)$. Over the measured field range of Fig. 4.5, δ_{2MW} changes by < 1 MHz. In contrast, the intermediate $|62P_{3/2}\rangle$ energy shifts by about 2.09 MHz/(V/m)^2, while the $|62P_{1/2}\rangle$ energy does not shift significantly. The $|62P_{3/2}\rangle$ level shifts by an absolute amount of ≈9 to 29 MHz over the field range measured in Fig. 4.2. Consequentially, Δ increases by about 25% over the same range. Figure. 4.5 shows the results of the calculation plotted as solid lines. The two lines do not intersect at $|E| = 0$ because $\delta_{2MW} \neq 0$.

The AC Stark shifts and two-photon couplings in the Hamiltonian are proportional to $|E|^2$. When $\delta_{2MW} = 0$ for the two-photon $|62S_{1/2}\rangle \rightarrow |63S_{1/2}\rangle$ interaction, the eigenvalues and AT splittings would scale approximately as $|E|^2$ as well. However, when $\delta_{2MW} \neq 0$ the behavior is more complex. In the limit $\delta_{2MW} > \Omega_{2MW}$, the

AT levels have a near-constant energy splitting of $\hbar \times \delta_{2MW}$. At slightly larger field strengths ($\Omega_{2MW} > \delta_{2MW}$), the splitting approaches the $|E|^2$ scaling of the $\delta_{2MW} = 0$ case. The measurements presented here are in the limit where $\delta_{2MW} \approx \Omega_{2MW}$. As a result, the splitting does not exhibit a clear scaling behavior.

While perturbation theory sufficiently models the measured spectral shifting, a non-perturbative Floquet analysis (see Section 3.4) is performed in order to investigate the higher-order state mixing that is present with the stronger fields. The results of this calculation are seen in Fig. 4.5 as dashed lines. When comparing the results from perturbation theory and Floquet theory, there is good agreement up to about 2 V/m. For slightly stronger fields, the calculated energy of the lower AT state is lower for Floquet theory than perturbation theory by a few MHz because of the higher order couplings that are included in the calculation. While the results from the Floquet calculation should be more accurate than those of perturbation theory, the spectra appear to match better with the results of the latter. This is attributed to drift of the coupling laser frequency over the duration of the measurements. Additional uncertainty arises due to the inhomogeneity of the electric field.

The state character of each of the components of the AT states depends on the microwave field strength as well as the frequency detuning from the two-photon optical transition. This effect is evident in Fig. 4.5 since the ratio of the EIT-AT peak areas change as a function of field strength. The upper EIT-AT state is preferentially excited for smaller fields and is predominantly $|62S_{1/2}\rangle$ character. The lower EIT-AT state is preferentially excited for higher fields, and the $|62S_{1/2}\rangle$ and $|63S_{1/2}\rangle$ states are more strongly mixed. Moreover, in strong fields, the $|62S_{1/2}\rangle$ character becomes evenly distributed between the two EIT-AT states. Floquet analysis reveals that the signal-strength ratio of the lower and upper EIT-AT signals should vary from about 1/6 at the low-field end to about 2/3 at the high-field end over the field scan range of Fig. 4.5. Table 4.1(a) shows the mixing of $\ell > 0$ states into the relevant Floquet

(a) $|62S\rangle \rightarrow |63S\rangle$

E (V/m)	$\lvert m_j\rvert = 1/2$	Character
2	2.75	$\ell \neq 0$
4	7.44	in $\lvert 62S_{1/2}\rangle$ and $\lvert 63S_{1/2}\rangle$
2	0.08	$\ell \neq 0$ excluding $\lvert 62P\rangle$
4	0.29	in $\lvert 62S_{1/2}\rangle$ and $\lvert 63S_{1/2}\rangle$

(b) $|61D\rangle \rightarrow |62D\rangle$

E (V/m)	$\lvert m_j\rvert = 1/2$	3/2	5/2	Character
13	0.37	0.36	0.12	$\ell \neq 2$, $\lvert 61D_{3/2}\rangle$, $\lvert 62D_{3/2}\rangle$
37	3.88	11.24	0.96	in $\lvert 61D_{5/2}\rangle$ and $\lvert 62D_{5/2}\rangle$
13	0.36	0.22	0.15	$\ell \neq 2$
37	2.90	1.75	0.96	in $\lvert 61D_j\rangle$ and $\lvert 62D_j\rangle$

Table 4.1: Admixture percentages into AT-split levels from states identified in the right column. (a) For the $|62S_{1/2}\rangle \rightarrow |63S_{1/2}\rangle$ transition and fields as in Fig. 4.2. The total admixture percentages are shown, as well as admixture percentages excluding the mixing with the near-resonant intermediate $|62P\rangle$ levels. (b) For the $|61D_{5/2}\rangle \rightarrow |62D_{5/2}\rangle$ transition and fields as in Fig. 4.6. The total admixture percentages are shown, as well as admixture percentages excluding fine-structure mixing. [3]

levels. The admixing results largely from the intermediate state detuning (Δ) from the $|62P_{3/2}\rangle$ level. As a result, this state is substantially mixed with the other two states, even at these low field strengths. Additionally, the admixture percentages of the $\ell \neq 0$ states other than $|62P\rangle$ are very small, as one would expect at these field strengths.

4.2.5 Sensitivity

Benefits of investigating the weak-field regime include showing this all-optical method to measure RF electric fields works, as well quantifying minor inhomogeneity effects. Further work is being done by other groups to increase the sensitivity of this measurement technique, as well as toward measuring weaker fields [25, 32, 34]. In contrast the work presented in the remainder of this chapter is working toward the other direction: measuring strong fields. Before making this jump in field strength, the intermediate-field regime is first investigated.

4.3 Intermediate-Field Regime

When more RF power is applied to the atoms, stronger state mixing begins to occurs, and Floquet theory must be used to model the spectra. When sufficient microwave power is applied, the atoms transition from a fine-structure-dominant (FS) regime to a microwave-coupling-dominant regime where the electron and orbital spins are decoupled (*i.e.* m_s and m_ℓ quantum numbers become separately conserved relative to the quantization axis given by the RF E-field).

In this section, the two-photon $|61D_{5/2}\rangle \rightarrow |62D_{5/2}\rangle$ transition is driven with 15.11635 MHz microwaves (within 0.5 MHz of the calculated transition frequency). In this case, there is no near-resonant intermediate state; the nearest dipole-allowed intermediate states are the $|63P\rangle$ and $|60F\rangle$ states from which the microwave frequency is detuned by ≈ 6 and $+5$ GHz, respectively. Hence, sufficiently strong electric fields are required to observe AT splitting. In this case, fields that are 10 times stronger than in the $|62S_{1/2}\rangle \rightarrow |63S_{1/2}\rangle$ case are used. In order to achieve such a high field, the microwave horn is placed directly against the vapor cell. Additionally, since D states are being driven instead of S states, the fine structure (FS) must be considered. At higher fields, this structure has a significant effect on the level mixings.

Figure 4.6 is an experimental density plot of the EIT-AT spectra in 1 dBm steps. The overlaid lines are the calculated Floquet energies in units of dBi (*i.e.* $10\log_{10}[I/I_0]$ where $I_0 = 1$ mW/cm^2). A field of 36.5 V/m is reached in the experiment, and Floquet energies in a field up to 87 V/m are plotted. There is good agreement between the two plots. Since all of the fields are z-polarized and the $|5S_{1/2}\rangle$ ground state only has a $|m_j| = 1/2$ component, it would be expected that only Rydberg states with $m_j = 1/2$ character would be seen experimentally. However, both $m_j = 1/2$ and 3/2 components are seen (short and long dashed lines, respectively) because most $|5P_{3/2}, F, m_F\rangle$ hyperfine levels contain multiple m_j components (with amplitudes given by Clebsch-Gordan coefficients). At the high-intensity end of the spectrum,

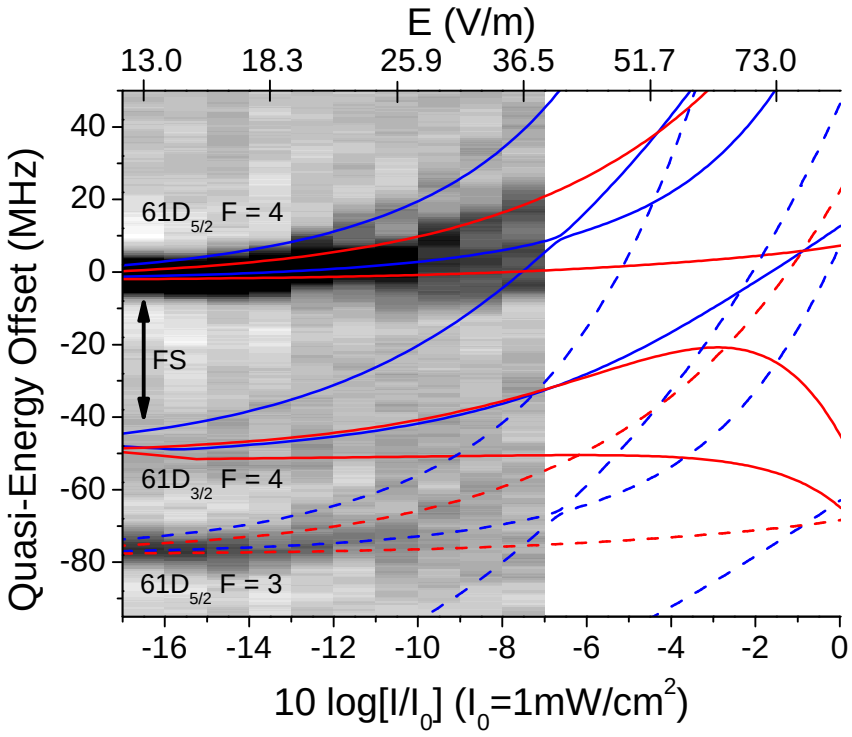

Figure 4.6: Density plot of experimental two-photon $|61D_{5/2}\rangle \rightarrow |62D_{5/2}\rangle$ EIT-AT spectra versus microwave intensity and field strength. The signal strength is represented on a linear gray scale from < 0.26 (white) to > 0.6 (black) in arbitrary units of the probe transmission. The fine-structure splitting at zero field of the $|61D\rangle$ state is indicated on the plot (FS). Calculated Floquet quasienergies for states with significant $|m_j| = 1/2$ (red) and $|m_j| = 3/2$ (blue) character are overlaid for the hyperfine EIT resonances $|5P_{3/2}\rangle$, $F = 4$ (solid) and $F = 3$ (dotted). [3]

the degeneracy of the $|m_j|$ levels are lifted. The break-up occurs at lower fields for $|m_j| = 3/2$ ($\sim$ 40 V/m) than it does for $|m_j|$=1/2 ($\sim$ 100 V/m). The FS mixing at 37 V/m is about three times as large for $|m_j| = 3/2$ as it is for $|m_j| = 1/2$ [see Table 4.1(a)].

Two-photon transitions scale as $|E|^2$ for low fields, with deviations reflecting the influence of higher order couplings in the system. At 40 V/m the system begins to enter the microwave-coupling-dominant regime. For the lower components of the $|m_j| = 1/2$ AT pairs, the positive AC Stark shifts are nearly canceled by the AT level repulsions, leading to near-stationary level energies with allometric-fit exponents substantially different from 2. Above $\sim$ 50 V/m, the deviations from $|E|^2$ become

more significant due to the more substantial higher-order couplings. Additionally, some dynamic electric dipole moments undergo a sign change as well.

Floquet analysis allows us to differentiate between mixing including and excluding fine-structure. Table 4.1(b) shows the different admixture components of the $|61D_{5/2}\rangle$ and $|62D_{5/2}\rangle$ AT pairs. The upper rows show the total admixture percentages of the $|61D_{5/2}\rangle$ and $|62D_{5/2}\rangle$ AT pair (including $D_{3/2}$ states), for the lowest and highest field strengths probed in the experiment. These states have a zero-field FS splittings of only ≈ 50 MHz, so the admixture percentages due to FS mixing are significant. The bottom rows of Table 4.1(b) shows admixture percentages from states with $\ell \neq 2$ into all $|61D_j\rangle$ and $|62D_j\rangle$ AT pairs with $j = 3/2$ or $5/2$.

Comparing the $|62S_{1/2}\rangle \rightarrow |63S_{1/2}\rangle$ study to the stronger-field $|61D_{5/2}\rangle \rightarrow |62D_{5/2}\rangle$ study, Table 4.1 shows that the mixing of $\ell \neq 2$ states into the $|61D_j\rangle$ and $|62D_j\rangle$ states is less than the mixing of $\ell \neq 0$ states into the $|62S_{1/2}\rangle$ and $|63S_{1/2}\rangle$ states. This is due to the larger detuning from the dipole-allowed transitions into intermediate states for the D case than the S case.

4.4 Strong-Field Regime

While the intermediate regime begins to provide interesting spectroscopic features and mixings, stronger fields result in more mixing and a plethora of unique features. Furthermore, the setup used for this set of measurements exhibits significant field inhomogeneity, and these effects are accurately modeled.

For these measurements, the probe beam has a power of 100 μW and is focused to a FWHM of 94 μm. The coupling laser had a power of 37 mW and was focused to a FWHM of 144 μm. The microwave horn was placed adjacent to the vapor cell ($\sim$1 cm from the optical beam foci), which is in the near field of the horn. The microwave frequency was set to 12.4611548 GHz (in the Ku band) to drive the zero-field $|65D_{5/2}\rangle \rightarrow |66D_{5/2}\rangle$ two-photon transition.

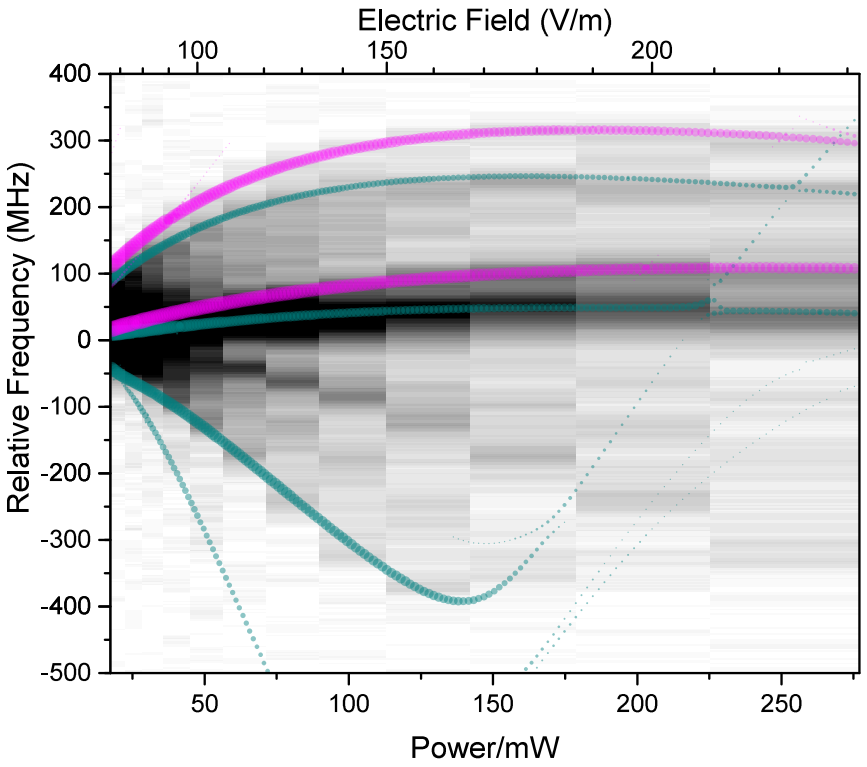

Figure 4.7: Experimental strong-field spectra measurement of 12.4611548 GHz microwaves on the $|65D\rangle \rightarrow |66D\rangle$ two-photon transition versus power. Each spectrum is an average of 20 traces and the signal is represented on a linear gray scale. The Floquet calculation is overlaid with excitation rates from $|5P_{3/2}, |m_j| = 1/2, 3/2\rangle$, given by the dot areas in teal and magenta, respectively. The electric-field values are given by the top axis. Background signal and additional features in the experimental strong-field spectrum are due to the microwave electric-field inhomogeneity within the cell. [2]

Figure 4.7 shows the experimental spectra for injection microwave powers of 13-24 dBm in steps of 1 dBm plotted as a function of power. Due to the substantial amount of level mixing, Floquet analysis must be used. Doing so, it is determined that a field of 230 V/m is achieved, which is about 20% of the microwave ionization limit for this state [7, 63] and about 6 times stronger than that measured in the intermediate regime. Additionally, this was the strongest RF electric field measured using this technique when this result was published.

The zero-field fine structure of the $|65D\rangle$ and $|66D\rangle$ states ($\sim$ 40 MHz) is broken up in the strong-field regime because it is small compared to the microwave-induced

shifts. Moreover, at the lowest power in Fig. 4.7, the $|65D\rangle$ EIT line is already broadened by the microwave power. The EIT resonance has a FWHM of $2\pi \times 50 \pm 1$ MHz, which is a factor of 2 larger than that of the microwave-free EIT resonance. The linewidth was intentionally enlarged to obtain a stronger signal.

In Fig. 4.7, the lines exhibit a linear shift as a function of power up to ~ 70 mW, as expected for a two-photon transition in the weak-field regime. Also in this range, as the microwave power is increased the signal strength begins to diminish because higher-order couplings lead to a redistribution of oscillator strength between many field-perturbed Rydberg states. This is reflected in the rapid initial decrease in the signal strength; over the first 30 mW increase in microwave power, the peak signal strengths of the individual spectral lines are reduced by more than an order of magnitude. At microwave powers above ~ 70 mW, the lines become non-linear, signifying the increase of state mixing and higher-order couplings.

Figure 4.8 shows calculated Floquet energies and excitation rates $S_{\nu,N}$ (see Eqn. 3.8) in the vicinity of the $65D$ Rydberg level for a microwave frequency of 12.4611548 GHz and field strengths ranging from 0 to 400 V/m. The region in the gray box is the region where the experimental spectra was taken. The field is plotted on a quadratic scale to show the dependence of the atomic level shifts on power, and for direct comparison with Fig. 4.7.

It is noted that there are additional spectral lines in the experimental map (Fig. 4.7) that are not seen in the calculation. This is due to inhomogeneity of the field within the measurement volume due to the dielectric cell and the proximity of the microwave horn. Overall, there is excellent agreement between dominant features in the experimental and theoretical Floquet maps. However, to properly quantify the electric field, the inhomogeneous effects need to be accounted for in the modeling.

While the weak-field regime allows for direct measurements of the electric field based on the splitting (see Eqn. 3.2), it is only by comparing sections of measured

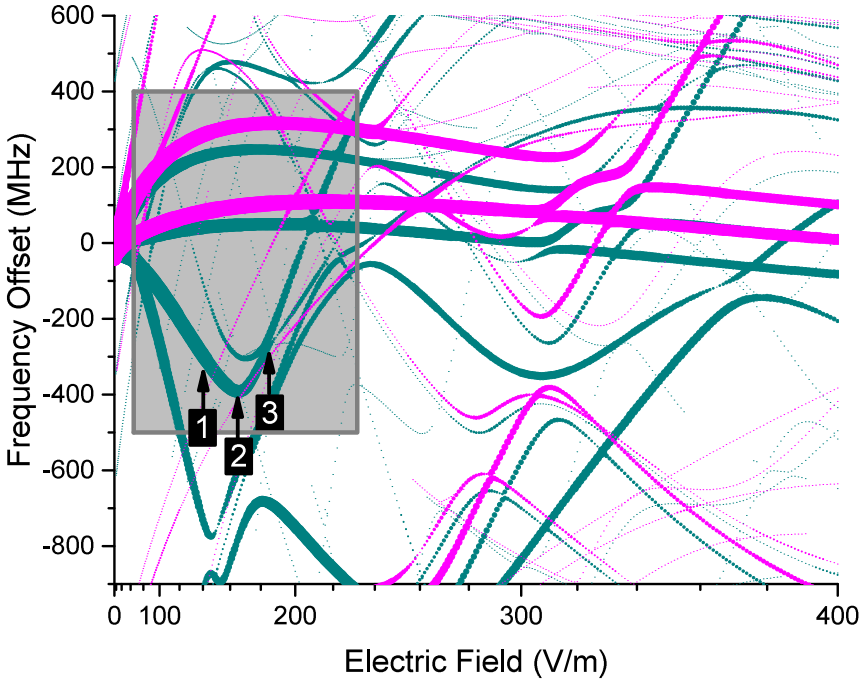

Figure 4.8: Calculated Floquet quasi-energies corresponding to the experimental spectral map of Fig. 4.7. The area of each dot is proportional to the excitation rate from $|5P_{3/2}\rangle$ with $|m_j| = 1/2$ (teal), $3/2$ (magenta). Boxed region indicates parameter space covered in Fig. 4.7. Labels indicate the regions for Fig. 4.11. [2]

maps and calculated Floquet maps that strong-field measurements can be determined. In this strong-field regime, avoided crossings provide convenient markers for spectroscopic determination of the RF E-field on an absolute scale. A notable feature for the states used here is the avoided crossing at 165 V/m (see point 2 of Fig. 4.8). There are several matching locations in the experimental spectrum (Fig. 4.7). These can be better seen in Fig. 4.9(a), which shows the data on a dBm scale. Each of the dominant microwave field domains provides its own rendering of the avoided crossing. The rendering at the lowest injected microwave power corresponds to the electric-field domain with the highest field at a given injected power. The avoided crossing is observed first at 130 mW, at which point the domain that has the highest field reaches 165 V/m. Hence, at a microwave power of 250 mW, the strongest RF field measured is 230 ± 14 V/m where the uncertainty is given by half the experimental step size (± 0.5 dB, corresponding to $\pm 6\%$ in field).

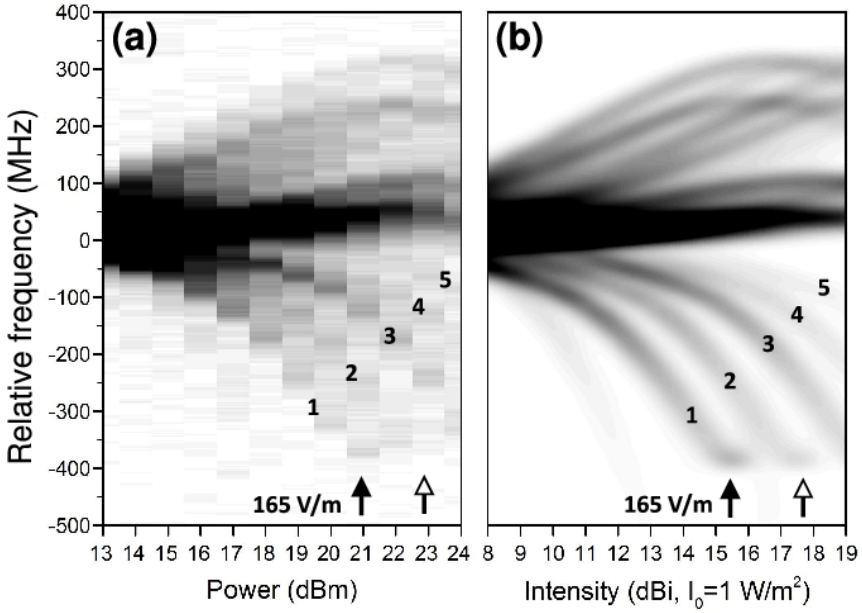

Figure 4.9: (a) Experimental spectra of the $|65D\rangle \rightarrow |66D\rangle$ two-photon transition versus microwave power. The signal is represented on a linear gray scale in arbitrary units. The arrows indicate coordinates that correspond to the same avoided crossing in the theoretical Floquet map, marked 2 in Fig. 4.8. The solid arrow corresponds to the spatial region with the highest microwave intensity along the probe beam. The labels 1-5 mark the renderings of the same level in Fig. 4.8 observed in the five different intensity domains (see text). (b) Composite Floquet map model of (a). [2]

As a result of the inhomogeneity within the cell, the RF field can be pictured as a speckle pattern, such as those seen for scattered coherent fields. The number of speckles is expected to be on the order of $\frac{\text{Cell Length}}{\text{Wavelength}} = \frac{75\text{ mm}}{24\text{ mm}} \approx 3$. Experimentally, five downward spectral lines are observed [labeled in Fig. 4.9(a)] corresponding to one calculated downward line (feature 1 in Fig. 4.8). The experimental spectrum is modeled, accounting for these five dominant RF E-field domains. In the model, the probability distribution for intensity on a decibel scale is give by

$$P_{dBi}(s) = \sum_{|m_j|=1/2}^{3/2} \sum_{k=1}^{5} w_{m_j}(|m_j|) w_k(k) P_{dBi0}(s + \Delta s_k). \tag{4.1}$$

In this equation, k is an index for the five microwave field domains, $w_k(k)$ is the probability that an atom contributing to the signal resides within domain k, $w_{m_j}(|m_j|)$

k	Δs_k (dB)	w_k
1	0.0	0.39
2	-2.0	0.21
3	-4.17	0.27
4	-6.0	0.09
5	-8.0	0.04

Table 4.2: Parameters extracted from Fig. 4.7 for modeling. These values are used in Eqns. 4.1 and 4.2 to generate the plot of Fig. 4.9(b).

is the probability that an atom contributing to the signal has a magnetic quantum number $|m_j|$, and P_{dBi0} is a Gaussian point-spread function that accounts for inhomogeneous spectral broadening within the five domains. Additionally, Δs_k is the amount (in dB) the central microwave intensity within the k^{th} microwave field region is shifted relative to the highest-intensity ($k = 1$) domain. The fit parameters in the model are Δs_k, w_{m_j}, w_k, and the standard deviation σ_{dBi} for P_{dBi0}. Optical EIT broadening and laser line drifts are accounted for by an additional Gaussian spread function in frequency, $P_\nu(\nu)$, which has a standard deviation σ_ν. From the theoretical spectrum $S_T(s, \nu)$ (from the Floquet calculation), the model spectrum $S_E(s_0, \nu_0)$ is then given by the convolution

$$S_E(s_0, \nu_0) = \int S_T(s_0 - s', \nu_0 - \nu') P_\nu(\nu') P_{dBi}(s') d\nu' ds' \tag{4.2}$$

where the intensities in the arguments of S_E and S_T are measured in dBi, defined as $10 \log_{10}[I/(1\ \mathrm{W/m^2})]$, where I is the RF field intensity.

Analysis of the experimental map (Fig. 4.7) yields Δs_k and w_k, which are given in Table 4.2. The weighting factor w_{m_j} for $|m_j| = 1/2$ and $3/2$ states is 0.7 and 0.3, respectively. The larger weighting for the $|m_j| = 1/2$ states is most likely due to optical pumping by the EIT probe field. These values are significant to within about 0.5 dB for Δs_k, ± 0.04 for w_k, and 0.1 for w_{m_j}. Additionally, $\sigma_{dBi} = 1$ dBi and $\sigma_\nu = 30$ MHz. The resulting map given from $S_E(s_0, \nu_0)$ is shown in Fig. 4.9(b)

in dBi. Comparison of the experimental and modeled spectral maps [Figs. 4.9(a) and (b)] show excellent agreement despite the complex features that arise due to the field inhomogeneity within the cell. Moreover, the empirical model used is rather straightforward.

4.5 Wavefunction Coefficients and Dipole Moments

In strong fields, the wavefunction coefficients and dipole moments vary significantly throughout the microwave-field cycle. As a result, the Floquet modes exhibit non-trivial wave-packet motion, and the equation for line strength $S_{v,N}$ (Eqn. 3.8) must be used. It is incorrect to associate the excitation rates of the Floquet modes with the $|65D\rangle$ probabilities the modes carry. In weak fields, the dressed-state coefficients and dipole moments have fixed amplitudes and phases relative to the field (in the field picture and using the rotating-wave approximation), but this is not the case for strong fields. The Floquet modes are time-periodic wave packets that are synchronized with the driving RF field.

Figure 4.10 shows snapshots of the wavefunction probability distribution at quarter intervals of the microwave cycle and Fig. 4.11 shows the $n-\ell$ distributions at the these same times. The columns are distributions for states at three different electric field values are shown (as indicated in Fig. 4.8). The first row for each figure is where the microwave field is maximal along the $z-$axis. The $n-\ell$ distribution (Fig. 4.11) for point 1 of Fig. 4.8 is more concentrated around $|65D\rangle$ and $|66D\rangle$. In contrast, that of point 3 is more spread out with the central peak around $|63P\rangle$. Point 2 is a superposition of the other two.

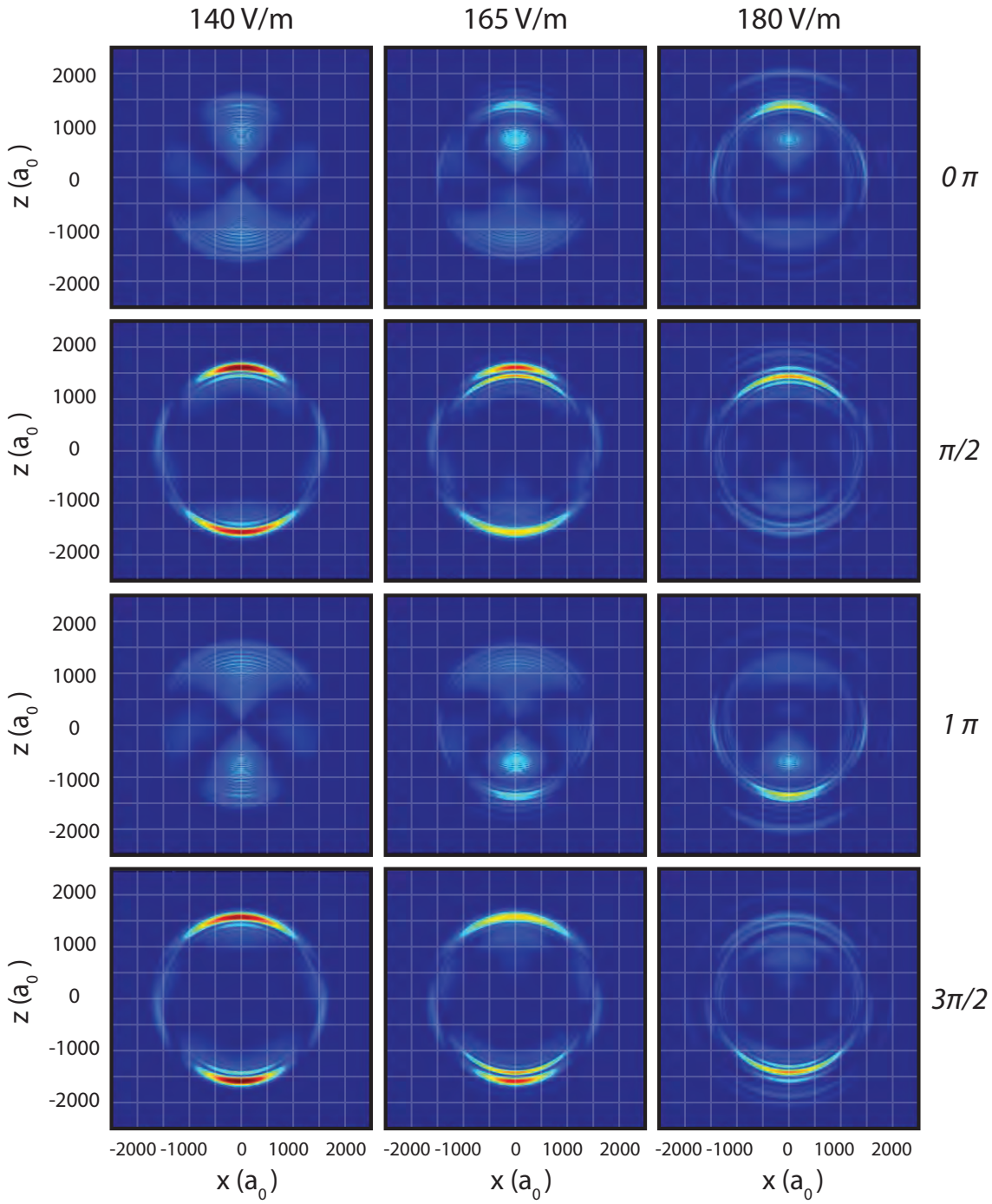

Figure 4.10: Wavefunction probability distributions of Floquet states associated with the $|65D_{5/2}\rangle \rightarrow |66D_{5/2}\rangle$ transition. The columns left to right correspond to 140 (point 1), 160 (point 2), and 180 V/m (point 3) of Fig. 4.8 over the course of one microwave period. Each row corresponds to quarter intervals of the microwave period from top to bottom row respectively. The $|E|$-field is maximal and points along $+z$ at 0π for all columns.

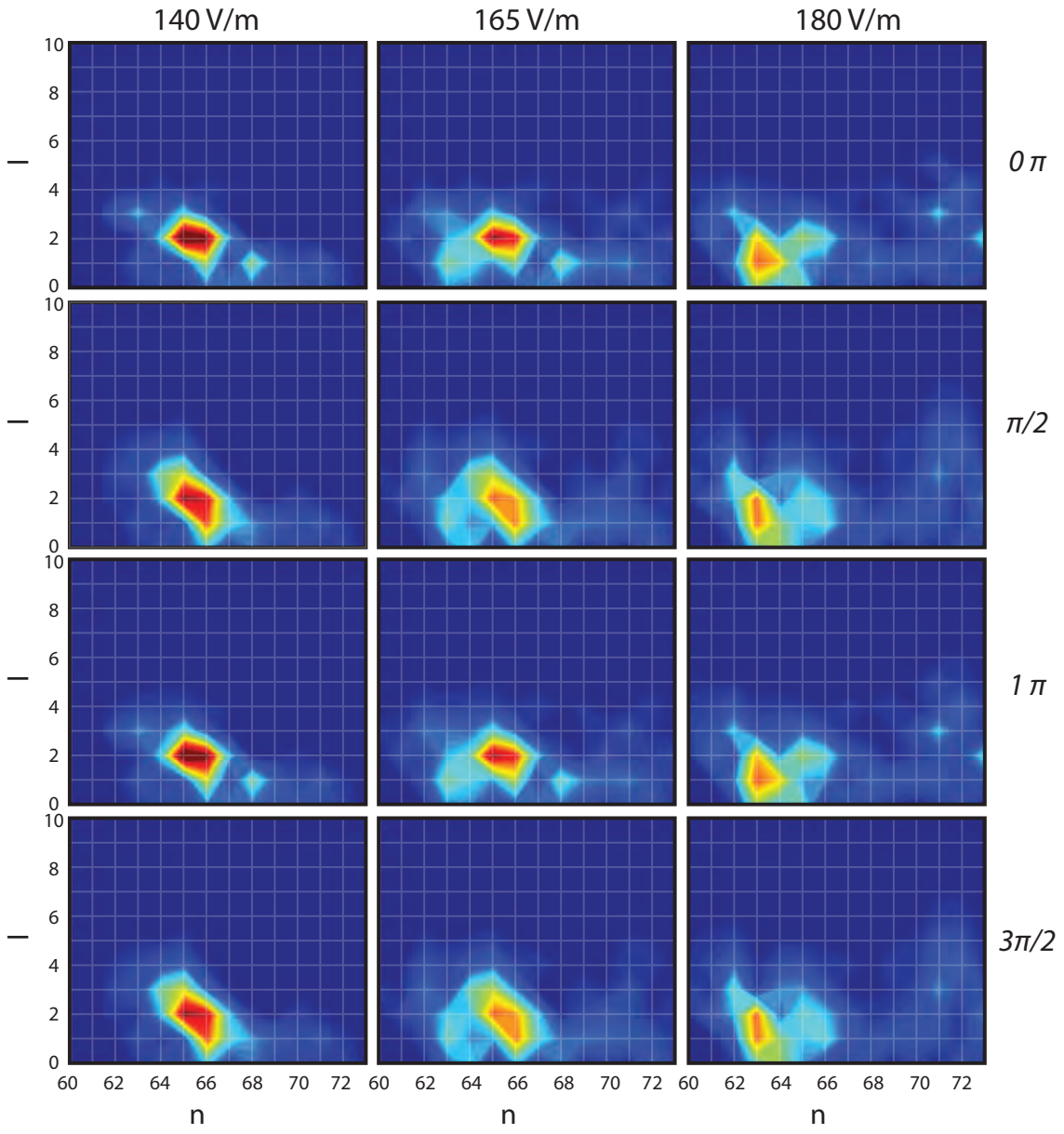

Figure 4.11: Distributions of the $n-$ and $\ell-$character of Floquet states associated with the $|65D_{5/2}\rangle \rightarrow |66D_{5/2}\rangle$ transition. The columns left to right correspond to 140 (point 1), 160 (point 2), and 180 V/m (point 3) of Fig. 4.8 over the course of one microwave period. Each row corresponds to quarter intervals of the microwave period from top to bottom row respectively. The $|E|$-field is maximal and points along $+z$ at 0π for all columns.

4.6 Conclusion

In this chapter, measurements were presented for one- and two-photon transitions of room-temperature ^{85}Rb atoms using Rydberg EIT-AT in a wide range of RF elec-

tric fields spanning three regimes. For the first regime, the one-photon transitions $|62S_{1/2}\rangle \rightarrow |62P_{3/2}\rangle$ and $|26D_{5/2}\rangle \rightarrow |27P_{3/2}\rangle$ were investigated in the presence of a weak-field. Next, the $|61D_{5/2}\rangle \rightarrow |62D_{5/2}\rangle$ transition was used to measure stronger electric fields in the intermediate regime where more substantial mixing with higher-order states begins to occur. At the higher end of the measurement range, the system begins to enter into the fine-structure mixing regime. The third regime that was investigated was the strong-field regime where there is strong higher-order mixing.

The intermediate- and strong-field regimes require Floquet theory for accurate modeling. In the strong-field case, there was substantial inhomogeneity within the measurement volume since the cell was in the near-field of the horn, in addition to previously mentioned effects. A relatively simple model is able to account for the different field regimes within the measurement volume. The uncertainty of these measurements is given by how well the spectral features can be resolved. For the strong-field case, the anti-crossing (see point 2 of Fig. 4.8) can be resolved with ± 0.5 dBi uncertainty, corresponding to an absolute field uncertainty of $\pm 6\%$, which is a good error for RF measurements.

All of these transitions illustrate that the method of using Rydberg-EIT to measure RF electric fields is a broadband technique that spans a range of GHz frequencies (based on the choice of Rydberg states and transitions) and a wide range of powers (< 1 V/m to > 230 V/m). The work presented here extends the dynamic range of the technique of Rydberg-EIT RF-field sensing as well. Further extension of this range is currently being made in both directions by various groups. On the upper end of the range, fundamental limitations due to the underlying atomic physics will eventually occur when the Rydberg atoms experience substantial microwave ionization rates [7, 63].

CHAPTER V

Rydberg State RF Modulation

The work discussed in this chapter consists of material published in Ref. [5].

In the previous chapter, the spectral maps presented primarily involved low angular momentum ℓ-states. Couplings to high-ℓ states were not included because the RF fields were not strong enough to couple them to the Rydberg states. The spectra in this chapter begin to deal with hydrogenic Rydberg states (states with high angular momentum ℓ and very small quantum defects). When these states are exposed to a DC field, they are Stark shifted and their degeneracies are lifted, resulting in a spectral map that resembles a fan [7, 64]. Recently, this spectral fan has been measured in a room-temperature cell using EIT [37]. For sufficiently high electric fields, the fan intersects Rydberg states with low angular momentum (in Rb $\ell \leq 2$) that are initially outside the fan of hydrogenic states. At the point where the levels intersect, there are many level crossings, as well as substantial mixing of high- and low-ℓ Rydberg states. When a RF field is applied, similar behavior occurs. However, there is now an added complexity due to the presence of dense sets of RF-dressed states.

Recent work in other groups has investigated the effects of AC and DC fields in Rydberg atoms and employed low-order perturbation theory to describe the behavior of the atoms [65, 66]. However, for strong fields, perturbation theory cannot adequately describe the system and a full Floquet calculation is required. Elsewhere,

Floquet treatment has also been employed to describe the effects of AC and DC fields in hydrogenic Rydberg states of sodium in the limit of weak field amplitudes [67].

In the experiments presented in Chapter IV, RF fields with GHz frequencies were applied to Rydberg states, driving $|Rydberg\rangle \rightarrow |Rydberg\rangle$ transitions. In contrast, the experiments of this chapter use MHz frequency fields applied to Rydberg states. Here, at low fields the Rydberg level undergoes an AC Stark shift proportional to the RF intensity. As the RF power is increased, sidebands of the main EIT line are introduced at sufficient field strengths. For purely harmonic fields, only even sidebands appear (*i.e.* sidebands separated by an even multiple of the RF driving frequency) due to electric dipole selection rules. When there is an additional DC field component, odd sidebands (*i.e.* sidebands separated by an odd multiple of the RF driving frequency) are present as well.

For the work presented in this chapter, $|60S_{1/2}\rangle$ and $|58D_{5/2}\rangle$ states are investigated in strong fields of 50 and 100 MHz frequencies, respectively. The applied fields span a range that includes fields above the Inglis-Teller limit, where the level shifts are no longer quadratic and where the driven states intersect with the fan of hydrogenic states [49]. Again, Floquet theory is used to model the spectral maps. There is excellent agreement between the measured and calculated maps. Using this method, it is determined that RF electric field amplitudes up to 296 V/m to within an uncertainty of $\pm 0.35\%$ are measured. This is almost an order of magnitude better than the uncertainty of standard RF electric field calibration probes [28, 29]. Finally, the DC shielding effect of the glass vapor cell is discussed, which is important in low-frequency field measurements.

5.1 Low-Field Modeling

Previous work has been done investigating the effects of AC and DC fields on Rydberg atoms [65, 66]. In these cases, low-order perturbation theory was used

to describe the behavior of the atomic energy levels. The modeling included the quadratic Stark effect and a first-order correction to the wavefunction. The excitation line strengths of the RF bands are given by the equation

$$B_N = \sum_{M=-\infty}^{\infty} i^{N-2M} J_{2M-N}\left(\frac{\alpha E_{DC} E_{AC}}{\hbar\omega}\right) J_M\left(\frac{\alpha E_{AC}^2}{8\hbar\omega}\right) \tag{5.1}$$

where ω is the frequency of the RF field, α is the static dipole polarizability of the Rydberg state, N is the number of RF photons involved in the transition, and J_i are Bessel functions [65]. A prominent feature that follows from Equation 5.1 are dropouts of the RF bands which occur at the zeros of the Bessel functions. Additionally, this equation describes why only even sidebands appear in the presence of a purely harmonic field. If $E_{DC} = 0$, then $J_{2M-N}(0) \neq 0$ only when $(2M - N) = 0$. Since M is an integer and N is the number of RF photons, only an exchange of an even number of photons is allowed.

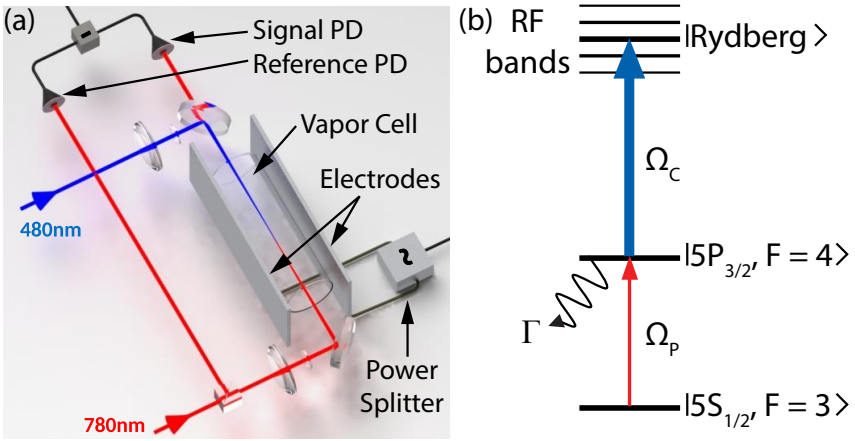

Figure 5.1: (a) Experimental setup of the electrode plate configuration including a vapor cell, 780-nm probe and reference beams (through and outside the vapor cell, respectively), 480-nm coupling beam, photodiodes for detection, RF power splitter (with a 180° phase difference between the outputs), and electrode plates. (b) Energy level diagram of the ^{85}Rb Rydberg-EIT transitions, where the Ω_P and Ω_C are the probe and coupling Rabi frequencies, respectively, and Γ is the intermediate-state decay rate. [5]

5.2 Setup

For the experiments presented in this chapter, the setup can be seen in Fig. 5.1. It is a slightly modified version of the setup described in Chapter II and used in Chapter IV. A primary difference is that the microwave horn is replaced with two metal plates parallel to the cell in order to create a stronger, more homogeneous field. The room-temperature vapor cell is suspended between two aluminum plate electrodes that are separated by 2.8 cm, slightly larger than the cell diameter. When a RF signal is applied to the plates, an electric field is generated at the location of the atoms in the cell. The RF is supplied by a signal generator, the output of which is passed through a 40 dB amplifier and split by a 180° power splitter.

Before the cell, the probe beam is split into two paths: one through the vapor cell (the signal beam) and one parallel to but outside of the cell (the reference beam). Each beam is incident on a photodiode, and the difference between the two signals is sent to the oscilloscope to be recorded. This arrangement is used in order to reduce noise due to laser power fluctuations. Unlike the previously described experiments, here the probe laser is locked to the $|5S_{1/2}, F = 3\rangle \rightarrow |5P_{3/2}, F = 4\rangle$ transition frequency of ^{85}Rb while the coupling beam is scanned over a range of $\sim$ 1 GHz around the $|5P_{3/2}, F = 4\rangle \rightarrow |Rydberg\rangle$ transition frequency at a rate of $\sim$ 1 Hz.

The coupler laser frequency is scanned instead of the probe frequency, which is more advantageous when performing strong field measurements. When applying a RF field to the atoms, the spectral lines shift, as seen in previous chapters. The stronger the field that is applied, the more the lines are shifted. When the blue frequency is locked, only a select velocity class is on-resonant with the field-shifted Rydberg line. As the line gets further shifted, the probe frequency that is on-resonant approaches the edge of the Doppler profile (since it is a thermal sample of atoms), meaning that the there are fewer atoms in the on-resonant velocity class. As a result the signal strength is reduced, which was seen in the previous chapter. To eliminate this effect,

the probe laser frequency is locked to be on-resonant with the center of the Doppler profile which gives the strongest signal. When the coupling laser frequency is scanned, a stronger signal is seen over a wider range.

The probe and coupling beams are each focused at the center of the cell. The probe is focused to a FWHM of 70 μm with a power of ≈ 5 μW. The coupling beam is focused to a FWHM of 84 μm with a power of ≈ 45 mW. Both optical beams are linearly polarized, with the polarizations parallel to the RF electric-field direction. As indicated in Fig. 5.1(b), the relevant frequencies characterizing the EIT system [45] are: the coupler Rabi frequency ($\Omega_{C,60S} \approx 2\pi \times 4$ MHz, $\Omega_{C,58D} \approx 2\pi \times 8$ MHz), the probe Rabi frequency ($\Omega_P \approx 2\pi \times 26$ MHz), the $|5P_{3/2}\rangle$ decay rate ($\Gamma = 2\pi \times 6$ MHz), and the laser linewidths ($\lesssim 1$ MHz). For the experiments presented in this chapter, the probe Rabi frequency was chosen to be higher at the expense of an increased EIT linewidth. This decision was made in order to have sufficient signal strength at higher fields, which was more important than reaching optimal spectral resolution to measure as strong of fields as possible.

5.3 Modulating $|60S_{1/2}\rangle$ with 50 MHz

First, the $|60S_{1/2}\rangle$ state modulated by 50 MHz RF fields is investigated. For this case, there is no fine structure and there are fewer spectroscopic lines than a D state. The signal generator power is varied from -43 to -25 dBm in steps of 0.2 dBm, and this is injected into the amplifier. Figure 5.2(a) shows the resulting experimental spectrum. As the RF power is increased, the main EIT line begins to shift lower in frequency. The first of the RF sidebands begins to emerge at about -38 dBm. These sidebands are of second order since they are separated from the main line by 100 MHz. At -31 dBm, the fourth-order harmonics appear. As expected, no odd harmonics are observed since an AC drive signal is used [65].

When the injected power reaches -28 dBm, the S line begins to mix with the

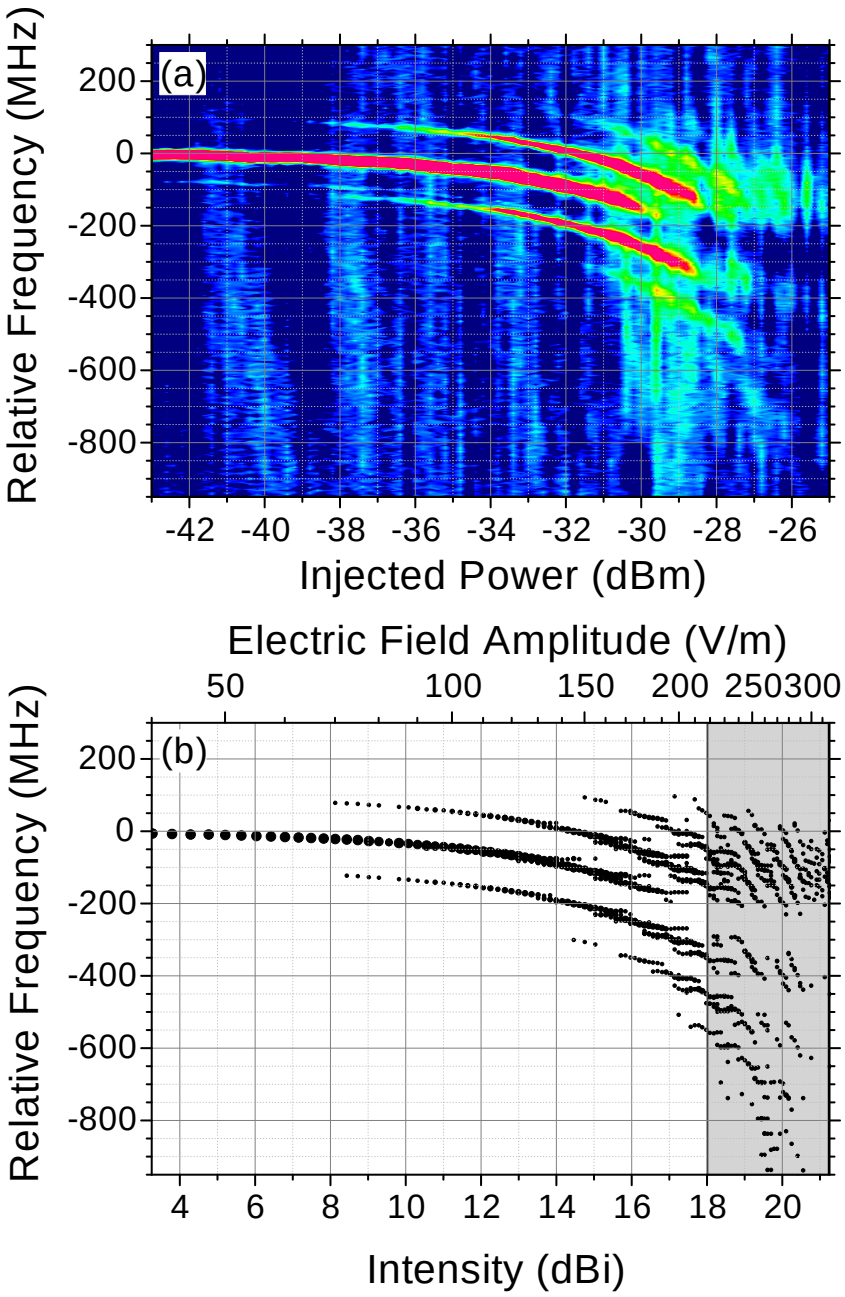

Figure 5.2: (a) Experimental and (b) calculated spectral maps of the $|60S_{1/2}\rangle$ state modulated by 50 MHz RF fields. (a) Linear color scale ranging from 0 (blue) to ≥ 0.01 (pink) in arbitrary units. (b) The area of each dot is proportional to the calculated excitation rate at that point. The dBi-value for intensity I is $10\log_{10}[I/(1\ \mathrm{W/m^2})]$. The gray shaded region indicates the domain in which the $|60S_{1/2}\rangle$ level mixes with the fan of hydrogenic states. [5]

hydrogenic states [see corresponding gray shaded box of Fig. 5.2(b)]. In this region, the signal strength is significantly reduced because the coupler-transition oscillator strength spreads over an increasing number of RF-dressed Rydberg levels. Because of this, the signal drops below the experimental sensitivity limit at about -26 dBm.

5.4 Modulating $|58D_{5/2}\rangle$ with 100 MHz

While the S states provide interesting spectroscopic features, it is desirable to go to states with higher angular momentum in order to study a regime where stronger mixing occurs. To do so, the nearby $|58D_{5/2}\rangle$ state is investigated. D ($\ell = 2$) states have higher angular momentum than S ($\ell = 0$) states. Hence, they couple with the hydrogenic lines in first order, so the mixing is stronger in the D case than the S case. Furthermore, the $|58D_{5/2}\rangle$ level is more strongly coupled to the $|5P_{3/2}\rangle$ intermediate level than the $|60S_{1/2}\rangle$ level is, which results in an improved signal-to-noise ratio.

Here, the $|58D_{5/2}\rangle$ state is driven with 100 MHz instead of 50 MHz in order to have increased separation between the RF-dressed Rydberg levels. Figure 5.3(a) shows the experimental spectrum of the modulated $|58D_{5/2}\rangle$ state for RF powers ranging from -34 to -25 dBm in steps of 0.1 dBm. At low fields, the two lines are the $|m_j| = 1/2$ and $3/2$ components. The weaker $|58D_{3/2}\rangle$ fine structure component also appears in the spectrum (for $|58D\rangle$ the fine structure splitting is 58.7 MHz). Both $|m_j|$ components are present in the RF-dressed sidebands as well. At high fields, multiple lines of the fan of hydrogenic states [see corresponding gray shaded box of Fig. 5.3(b)] are visible. These lines are very steep, and their slopes provide excellent spectroscopic features for calibrating the RF field.

In Fig. 5.3(a) at higher RF powers, the experimental signal appears to be spotted. This is an artifact resulting from the utilized 0.1 dBm step size of the signal generator. The spots are not clearly visible in Fig. 5.2(a) due to the lower signal strength.

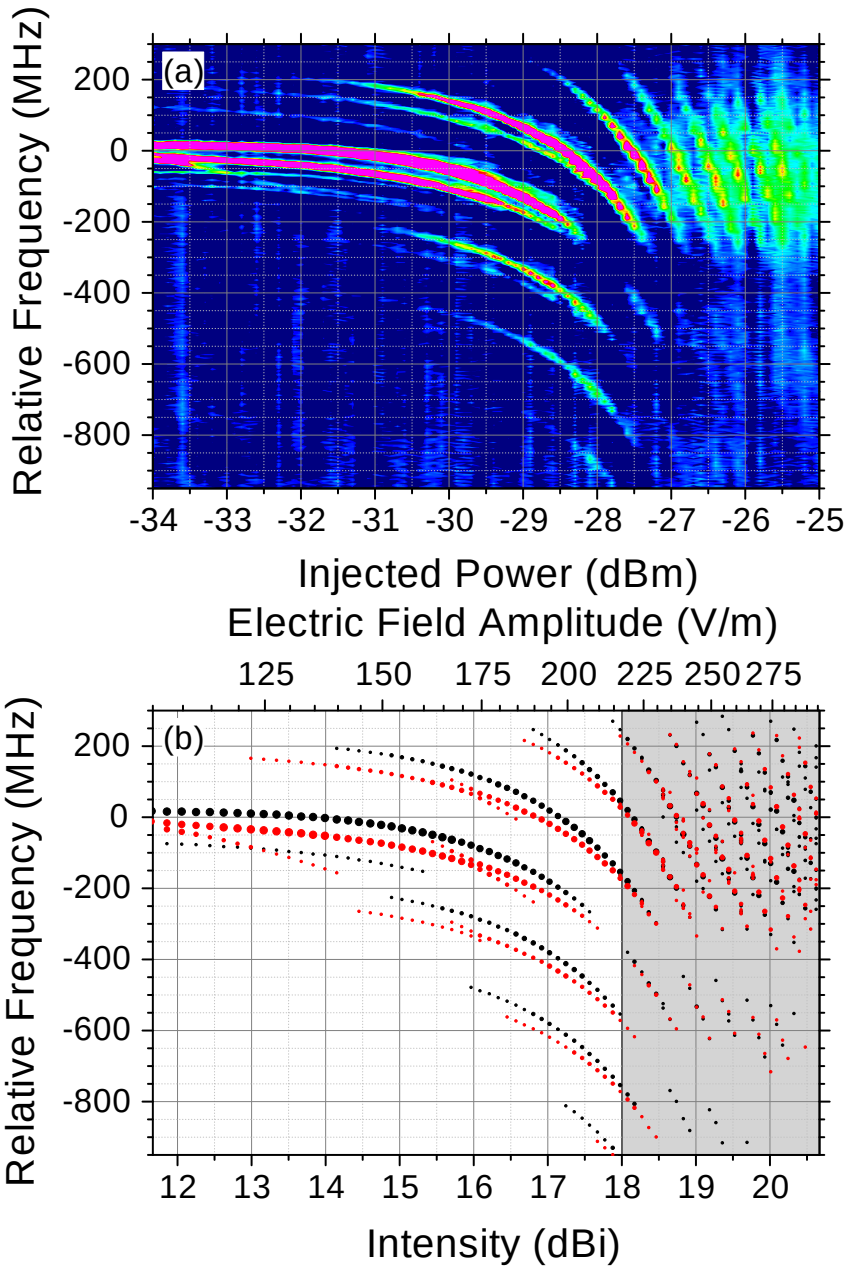

Figure 5.3: (a) Experimental and (b) calculated spectral maps of the $|58D\rangle$ state modulated by 100 MHz RF fields. (a) Linear color scale ranging from 0 (blue) to $\geq$0.01 (pink) in arbitrary units. (b) Black dots are $|m_j| = 1/2$ and red dots are $|m_j| = 3/2$. The gray shaded region indicates the domain in which the $|58D\rangle$ levels mix with the fan of hydrogenic states. The area of each dot is proportional to the calculated excitation rate. The dBi-value for intensity I is $10\log_{10}[I/(1\ \mathrm{W/m^2})]$. [5]

5.5 Calculated Floquet Map

Figures 5.2(b) and 5.3(b) show the spectra calculated from Floquet theory for the $|60S_{1/2}\rangle$ and $58D_{5/2}\rangle$ states, respectively. Each laser frequency $\omega_{\nu,N}$ where a Floquet

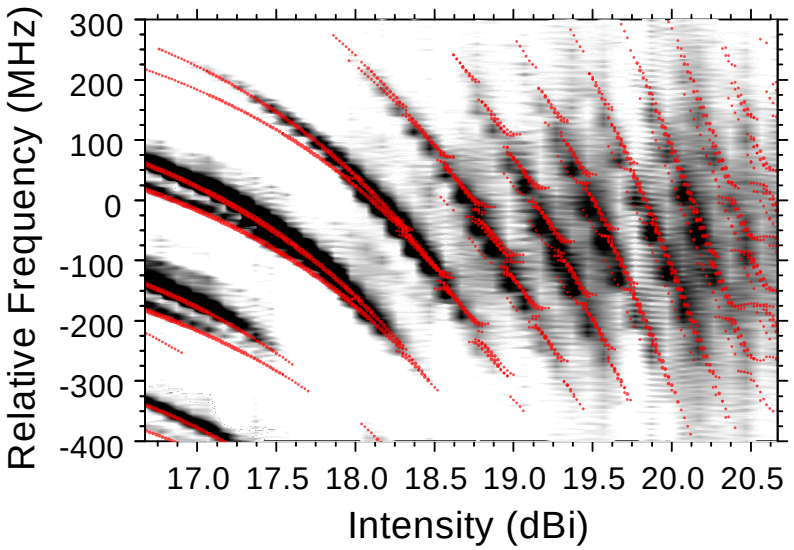

Figure 5.4: Enlarged section of Fig. 5.3(a) overlaid with a higher-resolution calculated spectral map. Experimental signal ranges from 0 (white) to $\geq$0.007 (black) in arbitrary units, and the calculated values are overlaid in red dots. The area of each dot in the calculation is proportional to the excitation rate. The dBi-value for intensity I is $10\log_{10}[I/(1\ \mathrm{W/m^2})]$. [5]

level is excited by two optical and N RF photons is represented as a circle with an area proportional to the excitation rate of that level. The x-axis is the RF intensity expressed in units of dBi = $10\mathrm{log}_{10}(\mathrm{I/I_0})$, where $\mathrm{I_0} = 1\ \mathrm{W/m^2}$.

The excitation rates are taken into account as well in the Floquet maps. When the rates are neglected, then many additional Floquet levels are present in the calculated spectra. To illustrate this, Fig. 5.5 shows all Floquet levels (represented as small symbols (+) from a high-resolution calculated spectral map for $|58D_{5/2}, |m_j| = 1/2\rangle$ and $|58D_{5/2}, |m_j| = 3/2\rangle$ [parts (a) and (b), respectively] modulated by 100 MHz and how they vary in strong RF fields over a range of 1 dBi. All the spectral lines are plotted, not just those that are experimentally seen. The plot area of Fig 5.5 is a subset of the plot area of Fig. 5.3(b). The area of the circles is proportional to the excitation rates of the Floquet levels. This figure further illustrates that only a very small subset of levels are optically detectable. Moreover, the avoided crossings seen

in both Fig. 5.3(a) and (b) involve a large number of undetectable Floquet states that originate from the adjacent manifold of high angular momentum Rydberg states.

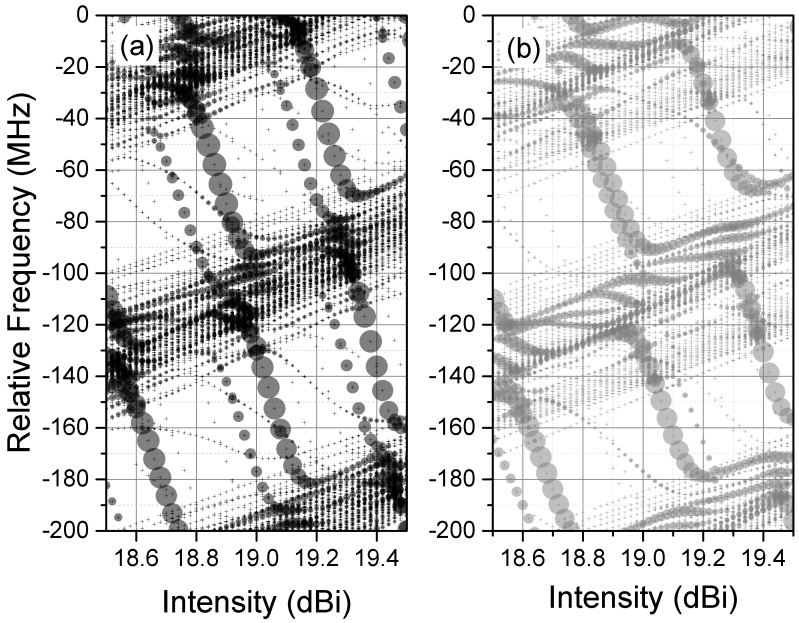

Figure 5.5: Higher-resolution calculated spectral maps of (a) $|58D_{5/2}, |m_j| = 1/2\rangle$ and (b) $|58D_{5/2}, |m_j| = 3/2\rangle$ modulated by 100 MHz RF. Calculation is performed in steps of 0.02 dBi. Small symbols (+) indicate the energies of all Floquet levels in the calculation. The areas of the dots are proportional to the excitation rates of the Floquet levels with measurable oscillator strengths. [5]

5.6 Analysis

Experimental and calculated spectra in Figs. 5.2 and 5.3 are in excellent quantitative agreement. Figure 4.9 shows a subset of the overlap of the two spectra of Fig. 5.3 in the region where the hydrogenic states are present. Comparing experiment and theory, it is determined that a maximum field strength of 317 V/m for $|60S_{1/2}\rangle$ and 296 V/m for $58D_{5/2}\rangle$ is reached. While both states are exposed to the same maximum injected RF power level of -25 dBm into the same input of the 40 dB power amplifier, the maximum fields reached differ by 20 V/m. This is attributed to a slight frequency dependence in the RF transmission line and generator performance (measured separately and not presented here).

By comparing the experimental and calculated maps for both of the measured S and the D states, the measured field (power) is determined to within $\pm 0.88\%$ ($\pm 1.75\%$) for the $|60S_{1/2}\rangle$ state and to within $\pm 0.35\%$ ($\pm 0.70\%$) for the $|58D_{5/2}\rangle$ state. This level of precision is about a factor of ten better than that achieved by traditional dipole probes used as standard references for RF field calibration [28, 29]. The level of precision is determined by the number of distinct spectral features. Moreover, states with larger dynamic dipole moments enable higher precision because they provide a tighter bound on the uncertainty in the alignment of experimental and calculated spectra. For the maps presented here, high precision is achieved because of the high density of the RF-modulated hydrogenic fan and the large dipole moments of the hydrogenic states.

For the $|60S_{1/2}\rangle$ state, the hydrogenic lines are less defined due to the signal-to-noise ratio. Aside from the steep hydrogenic lines, the dropouts in the $N = 0$ band (*i.e.* the main Rydberg-EIT line) and the locations at which the $|N| = 2$ and $|N| = 4$ bands develop large negative slopes (equivalent to large AC dipole moments) provide features for determining the precision as well. The $N = 0$ band dropout is centered at 18.0 dBi, corresponding to an RF-field amplitude of $E_{RF} = 218$ V/m. In comparison, the low-field perturbative model [65], which applies to isolated levels with fixed DC-polarizability α, predicts the first dropout of the $N = 0$ band to be at $E_{RF} = 231$ V/m. This is when $\alpha E_{RF}^2/(8\hbar\omega_{RF}) = 2.40$ (where the numerical value 2.40 is the first root of the first-kind Bessel function J_0). In this equation, the polarizability of $\alpha = 18.2$ kHz/(V/m)^2 and a 50 MHz modulation frequency are used. The occurrence of the dropout at a smaller field than the low-field model predicts is due to the increase in polarizability of the $|60S_{1/2}\rangle$ state at higher fields because of level repulsion from the hydrogenic states.

The $|58D_{5/2}\rangle$ spectrum has more features and higher overall signal strength than the $|60S_{1/2}\rangle$ spectrum, allowing for higher measurement precision than in the $|60S_{1/2}\rangle$

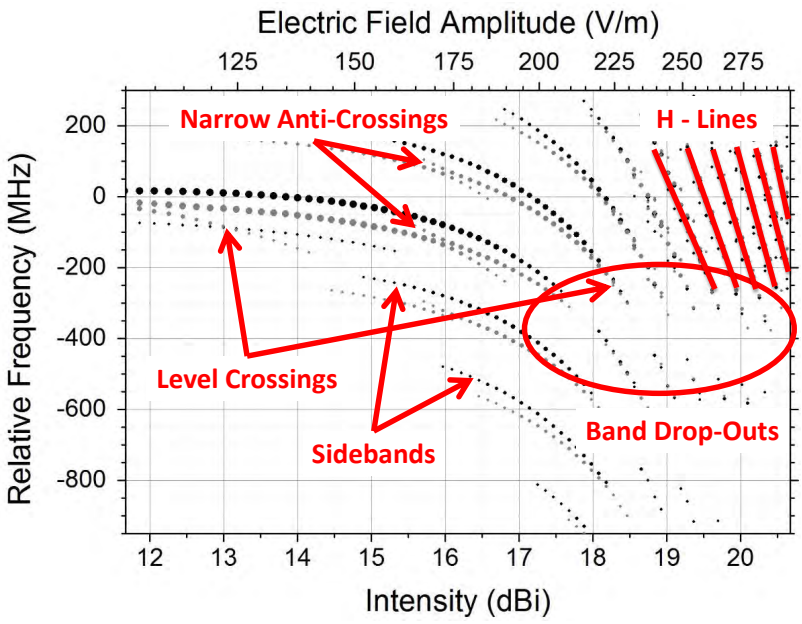

Figure 5.6: Calculated Floquet map of the $|58D\rangle$ state modulated with 100 MHz [the same plot as Fig. 5.3(b)]. The spectral features that are used for calibrating the RF electric field are indicated by the red markings and labels.

case. Figure 5.6 shows the same Floquet map as Fig. 5.3(b) (the $|58D\rangle$ state modulated with 100 MHz). The spectral features that are used for calibrating the RF electric field are indicated by the red markings and labels. One feature in particular is where the $|m_j| = 1/2$ and $3/2$ levels intersect, both in the main line as well as in the sidebands. The low field models, such as that of [65], are based on a fixed polarizability of the D Rydberg levels of Rb. However, this is not very accurate due to the large variation of the polarizability α of these levels already at small fields (below 100 V/m in the present case). Floquet theory is needed once again to accurately model the levels.

Another important feature that is more visible in the $|58D_{5/2}\rangle$ case is the hydrogenic lines. Since they are so steep, they provide excellent features for calibrating the field to high precision. Slight variations in alignment of the calculated spectra against the experimental ones lead to very noticeable variations in the achieved level of agreement. Figure 5.4 illustrates this point since there is excellent agreement be-

tween the two. Although the experimental data appears beaded due to the RF step size, resulting in blurring of the fine features, the avoided crossings of some of the RF-modulated hydrogenic levels manifest as a corresponding variation in the separation between the spots observed in the experiment.

In each of the scans taken, the bands are broadened to several tens of MHz wide due to saturation broadening of the probe transition. In these measurements, a slightly high probe intensity (about 11.5 $I_{\rm sat}$ with $I_{\rm sat} = 3.9$ mW/cm^2 [41]) was used in order to achieve satisfactory signal levels at the higher RF fields. An alternative approach that could be used in the future is to heat the cell and reduce the probe power. This would also allow avoided crossings [such as those in the $|m_j| = 3/2$ line at 16 dBi in Figs. 5.3(b)] to be better resolved. In future work, one may also consider a reduction of the coupler Rabi frequency in order to reduce the weak-probe EIT bandwidth, Ω_c^2/Γ (which applies when $\Omega_p \lesssim \Omega_c \lesssim \Gamma$).

Unlike the measurements of Chapter IV, the inhomogeneity of the RF field has negligible effect on the spectra here. This is because the diameter of the probe region (70 μm) is much smaller than the RF wavelength ($\geq$ 3 m). Moreover, the RF field does not vary significantly along the length of the cell (7.5 cm) since it is smaller than the length of the parallel-plate electrodes [see Fig. 5.1(a)].

5.7 DC Fields

In the spectra of Figs. 5.2 and 5.3, only even harmonics are present, meaning that there is no apparent DC field in the cell. Figure 5.7 shows a calculated $|58D_{5/2}\rangle$ spectrum as a function of an additional applied DC field polarized along the same axis as the AC component. Here, the RF field is 100 MHz and has a fixed field amplitude of 200 V/m. Both even and odd harmonics are present. The odd sidebands begin to appear at about 1-2 V/m, so this is the weakest DC field that would be resolvable in the current system. In order to obtain an upper limit for the amount of DC field

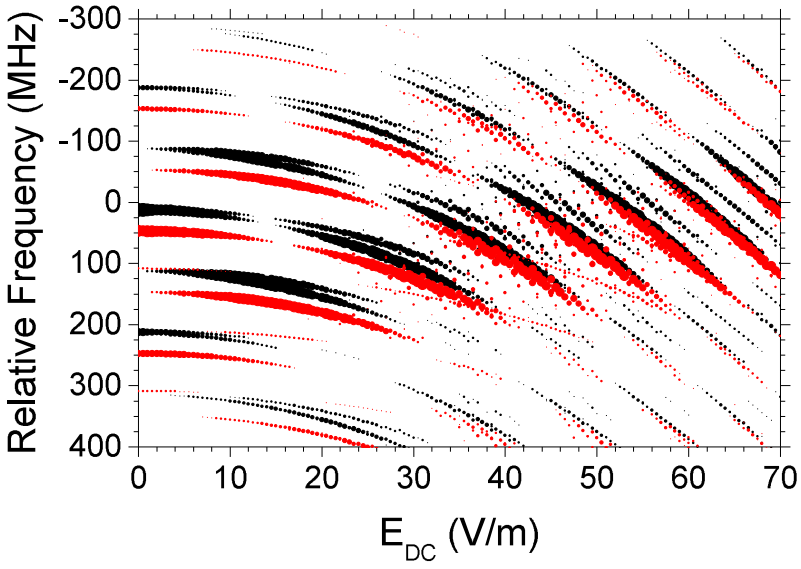

Figure 5.7: Calculated spectral map of the $|58D_{5/2}\rangle$ state modulated by 100 MHz RF with electric-field amplitude $E_{0,RF} = 200$ V/m as a function of applied DC field. Note that both even and odd sidebands are present. Black dots are for $|m_j| = 1/2$ and red dots are for $|m_j| = 3/2$. [5]

that could be present in the cell, a few additional measurements are taken.

A possible reason for the absence of DC fields within the cell is because of shielding by free charges within the cell, which has previously been suggested. These free charges can originate from a photoelectric effect on the inside surface of the glass and/or from thermal or Penning ionization of Rydberg atoms [65]. To test this, a pure DC voltage (no RF component) is applied across the two electrode plates. For both $|58D\rangle$ and $|82D\rangle$ Rydberg-EIT lines measured for several probe-beam powers (not shown here), there is no evidence of line broadening or shifting up to the experimental limit of the applied DC voltage of 1200 V. The corresponding DC test field of $\sim$400 V/cm (without cell) is about a factor of four higher than in a previous test [18]. The $|82D\rangle$ state is tested since states with higher principal quantum number are more sensitive to stray fields since the polarizability scales as $(n^*)^7$ [7].

To estimate the DC shielding factor for this setup, the required DC field to shift the energy of the state by the linewidth of the EIT line is calculated. In this

case, the EIT linewidth is ∼10 MHz. The calculated DC polarizability of the relevant D-states is several 100 MHz/(V/cm^2) to several GHz/(V/cm^2). A field of $\sqrt{(10\text{ MHz})(\frac{(\text{V/cm})^2}{100\text{ MHz}})} \approx 0.3$ V/cm would be expected to cause this shift in energy. However, no shift in the line is seen up to 400 V/m, resulting in a shielding factor of $\frac{400\text{ V/m}}{0.3\text{ V/m}} \approx 10^4$. Simulations of the field both with and without the presence of the dielectric glass cell give a shielding of only $\sim 4\%$. This result reiterates the ubiquitous finding that the interior volumes of spectroscopic alkali vapor cells are practically DC-field-free.

5.8 Conclusion

In this chapter, investigation of $|60S_{1/2}\rangle$ and $|58D_{5/2}\rangle$ Rydberg states in the presence of RF fields at 50 MHz and 100 MHz, respectively, using an all-optical readout method was presented. The driving field was purely harmonic, determined by observation of sidebands at only even multiples of the RF driving frequency. At high fields, the modulated low-ℓ Rydberg levels intersect with a hydrogenic fan of high-ℓ states.

The spectral maps are modeled with non-perturbative Floquet theory since low-field perturbation theory is not valid in this instance. Comparison of the measured $|58D_{5/2}\rangle$ spectral map with the calculated map results in determining that the electric-field measurement goes up to 296 V/m to within a $\pm 0.35\%$ relative uncertainty. This comparison is made using the unique spectroscopic features including the signal dropouts of modulation bands at certain fields, intersections of low-ℓ Rydberg lines with steep levels that are part of the hydrogenic fan of states, and level crossings and narrow anti-crossings in the spectral maps. A separate measurement allows for obtaining the lower bounds of the shielding factor of DC fields to be 10^4, agreeing with findings elsewhere.

Related work in cesium has been performed by Jiao *et al* [43].

CHAPTER VI

EIT and Ion Imaging in Cold-Atom Samples

Another project that I worked on during the entire duration of my graduate school career was the construction and implementation of a cold-atom experiment in a vacuum system. In addition to assembling all of the vacuum components, I set up all of the optics, electronics, and associated components to make the system operational. The system was designed for trapping and cooling of atomic samples, ultimately for Bose-Einstein condensate production. The design combines attributes of two other chambers of the Raithel group to be able to do a wide variety of experiments. Specifically, it combines the ability to create ultra-cold atom samples [68, 69] with the implementation of a tip imaging probe (TIP) which allows for high spatial magnification of the Rydberg atom positions [70].

Although optical molasses, optical pumping, and some magnetic trapping have been implemented in the chamber, at this point only magneto-optical traps (MOTs) are needed and utilized for the experiments presented here. Some of the unique components that are currently not in use will be discussed in this chapter as well.

EIT is slightly different in a cold atom sample than in a room-temperature vapor cell. After describing the setup used for the cold-atom samples, these differences will be discussed. Unlike in the previous two chapters, there is no RF field applied to the atoms here. One of the first experimental goals is to observe EIT in these cold

samples in conjunction with spatial imaging of the Rydberg atoms. By using a single-photon-counting module (SPCM) to detect the probe beam for EIT, the timing of the photon arrival is obtained. After recording and analyzing the resulting signals, the $g^{(2)}(\tau)$ function is obtained. The $g^{(2)}(\tau)$ function is a temporal correlation function which yields information about the timing between two different arbitrary photons. After the EIT optical pulse, the Rydberg atoms are field ionized and the positions of the resulting ions are detected. Processing these images yields information about the spatial correlation function $g^{(2)}(\mathbf{r})$ which relates the separation between two arbitrary Rydberg atoms. Experiments have been performed using EIT in cold samples and have found anti-bunching of the photons, meaning that two photons are less likely to occur at times less than the correlation time [10]. While such an effect has been seen for Rydberg S states [10], it has yet to be seen for D states [52]. Additionally, measurements have been made investigating spatial correlations of Rydberg atoms under various conditions [70–72]. The experiment presented for this chamber plans to simultaneously look at the $g^{(2)}(\tau)$ and $g^{(2)}(\mathbf{r})$ functions of Rydberg atoms in an EIT configuration, which has yet to be investigated.

One point to note is that the EIT curves presented in this chapter are preliminary. Many curves were taken to observe relative effects rather than obtain absolute measurements. Additionally, the curves were used as diagnostics and to get an overview of the settings. Enough averages were taken to see the curve shape, but not necessarily enough to result in a smooth curve. Many of these curves were taken as preliminary checks of the system, with the final goal of getting EIT with Rydberg states of $|70S\rangle$ and higher, knowing that significant optimization and averaging would be needed at this point.

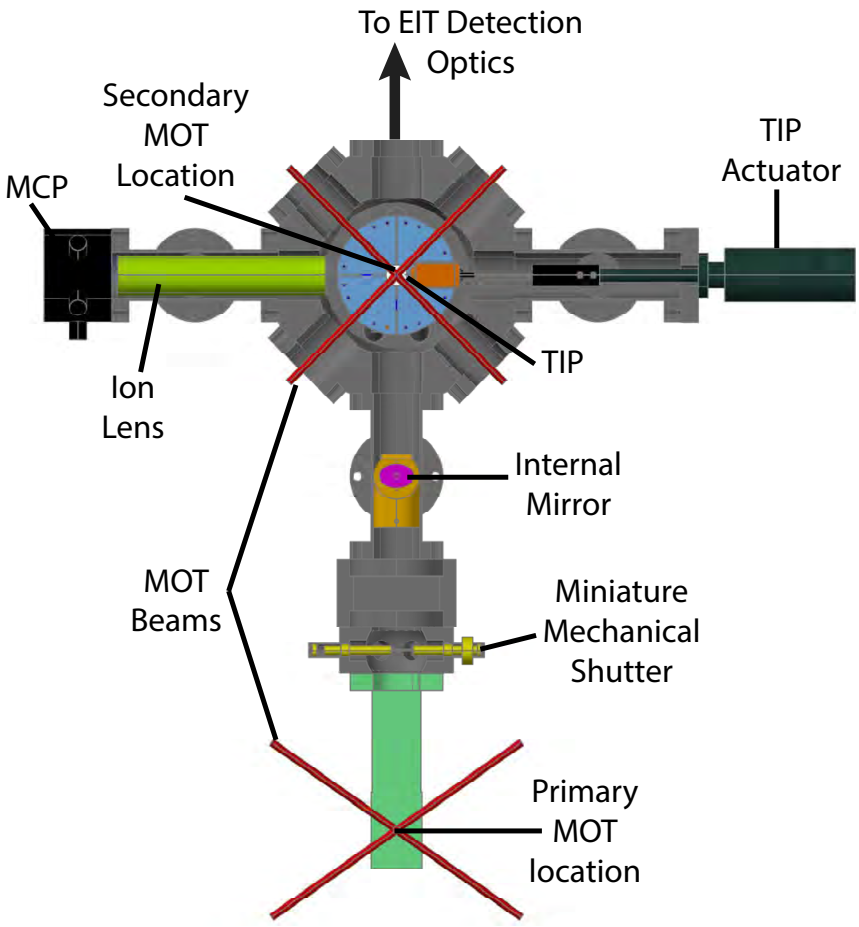

Figure 6.1: Cross-section of vacuum chamber with relevant components shown. Coloring is artificial to highlight various components. See text for details.

6.1 Design

A cross-section of the vacuum system can be seen in Fig. 6.1 with associated components labeled. It is a double-MOT system that uses ^{87}Rb. This isotope is chosen with BEC creation in mind because a positive s-wave scattering length is needed, ruling out ^{85}Rb as an easy choice. However, as mentioned in Chapter II, a variety of elements and isotopes can be used for EIT. Thus, the experiments in this chapter could have easily have been performed with ^{85}Rb as well.

The atoms are initially trapped in the primary MOT in the glass cell. A pusher beam then launches the atoms to the main chamber where a secondary MOT is

formed. The atoms pass through a miniature mechanical shutter (see Section 6.1.2 and Fig. 6.3), as well as the hole in a mirror in the intermediate vacuum cross. This mirror is used for additional optical access.

The features that are unique to this system are outlined in the following sections and the applications to future experiments are discussed in Chapter VII.

6.1.1 Lasers

For the cold atom setup, a different set of lasers is used than in the previous chapters. Since ^{87}Rb is chosen, slightly different laser frequencies are required (still ≈ 780 nm). This issue is a minor point since the lasers have a sufficiently wide scan range to access the transitions for both isotopes. Figure 6.2 shows the energy level diagram used in the cold atom setup. The arrows indicate the transitions required to cool and trap the atoms, as well as the EIT scheme.

To drive the cooling transitions, two different distributed Bragg reflector (DBR) lasers, known as the Master and Repumper lasers, are used. The choice to use DBR lasers instead of the external-cavity diode lasers (ECDLs) used previously is simply due to availability in the lab. Each laser beam is split off into multiple branches that are then fiber coupled, with the fiber outputs located close to the chamber. There are four branches: primary, secondary, pusher, and imaging probe. In each of these branches, the Master path passes through a double-pass AOM setup in order to control the slight frequency differences between each branch. The primary and secondary branches refer to the paths used for the first and second MOTs. The Repumper is only in MOT beam paths. For both of these fibers, the Master and Repumper paths are coupled into the same fiber input. The pusher path is used for launching the atoms from the primary MOT to the secondary MOT. The imaging probe (not to be confused with the EIT probe) is used for shadow imaging [68, 70] for diagnostics of the MOT location and density.

A different ECDL laser is used for the lower excitation beam for the creation of Rydberg atoms and for EIT. The laser used for the coupling beam in the previous chapters is fiber coupled over a significantly longer distance. Despite this, there is still ample power at the fiber output.

The polarizations of the fiber outputs for the EIT beams are not set, but they are approximately linearly polarized at an arbitrary angle with respect to each other. The polarizations will be set during optimization of the EIT signal.

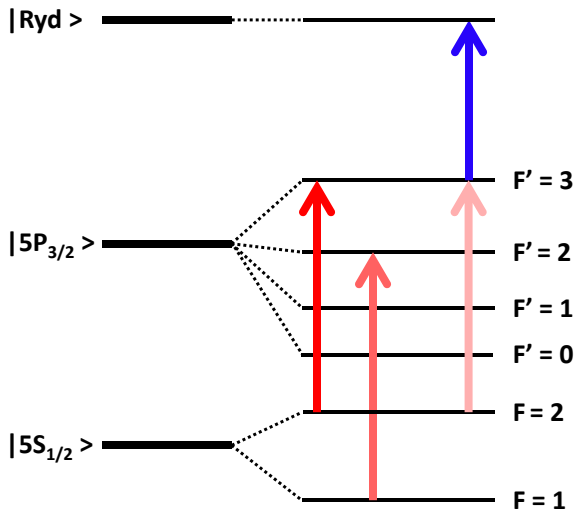

Figure 6.2: Energy level diagram used for the cold atom sample laser cooling and EIT. The left half shows the main levels and the right half shows the hyperfine states, as well as the transitions that the lasers are locked to. The far left arrow indicates the cooling transition, which the Master laser is locked to. The middle arrow indicates the Repumper transition. The far right arrows indicate the probe (faint red) and coupling (blue) transitions used for Rydberg excitation and EIT.

6.1.2 Miniature Mechanical Shutter

An in-vacuum miniature mechanical shutter of my design was developed for use in the chamber [6]. A diagram and photo of it can be seen in Fig. 6.3 (left and right, respectively). The shutter was developed for use in Bose-Einstein condensate (BEC) production. When making a BEC, background pressure, radiation pressure, and temperature are factors that need to be considered to minimize atom loss. Optical

beams, such as the pusher, can be blocked with shutters that are external to the vacuum. However, some atoms can still reach the secondary chamber due to the pressure differential between the two chambers of the setup. Although this effect is not enough to be able to load the secondary MOT, it is enough to decrease the number of atoms in the BEC magnetic trap due to collision of the "hot" atoms with the very cold atoms of the BEC.

The shutter is made from a stainless steel tube, glass tube segments, neodymium magnets, and vacuum chamber components for housing. The tube is flattened in the center and a hole is drilled into half of it. The ends of the rod rest and travel on the glass segments. These segments reduce the amount of contact the rod has, resulting in a lower resistance and better translation. A magnet is glued into each end of the stainless steel tube. One of these magnets is axially magnetized and the other is diametrically magnetized. The end that contains the axially magnetized magnet has a solenoid located outside of the vacuum. Depending on the direction of the current in the solenoid, the magnet is pulled in or pushed out, resulting in the translation of the shutter. The direction of the current is controlled by a home-built H-bridge circuit [73]. The diametric magnet is at the other end of the rod and is used in conjunction with an additional small axial magnet external to the chamber in order to prevent rotation of the shutter.

The shutter was tested both in air and under vacuum with various timings, duty cycles, and currents in the solenoid. When the solenoid is driven too quickly, the shutter is unable to cover its full range of motion. When too little current is used, then the motion of the rod does not respond as quickly. The shutter is found to operate well with 8 V and 5 A for a duration of about 50 ms. These settings result in the shutter responding 10 to 15 ms after the pulse is initiated and a total shutter movement time of about 2 ms. The shutter is designed to be run at a rate of < 1 Hz and is sufficient for the applications here. Faster operation would require re-optimizing the

parameters.

During construction of the vacuum chamber, the miniature shutter was incorporated into the setup. As of yet, it has not been implemented in the experimental cycle, but will be in future experiments.

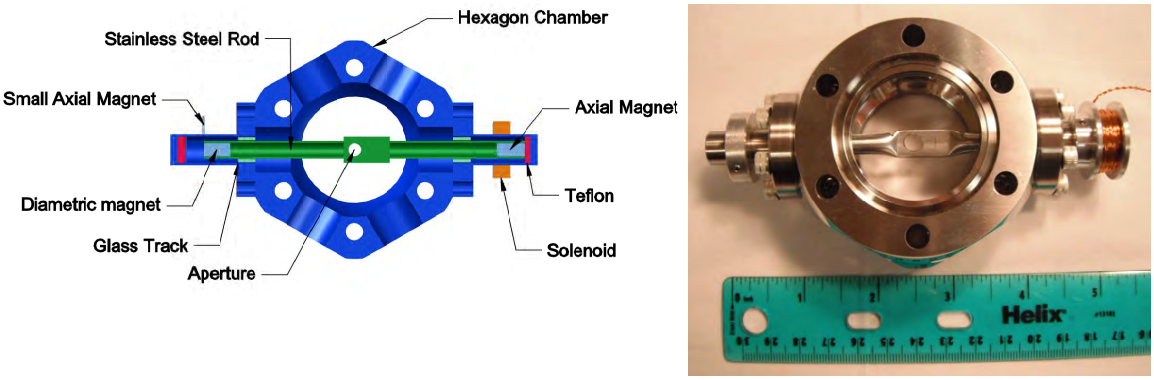

Figure 6.3: Left: cross-section of the miniature mechanical shutter with components labeled. Right: Photo of the actual shutter before being put into the vacuum system. [6]

6.1.3 Main Chamber

This system is designed with a quadrupole-Ioffe-configuration (QUIC) trap. In this configuration, there are two anti-Helmholtz (AH) coils, as well as an Ioffe coil which is smaller and perpendicular to those (see Fig. 6.4). All three coils are within the vacuum chamber, and the AH coils are within water-cooled heatsinks. Each heatsink has four electrodes used for electric-field control. These eight electrodes are independently controlled, so compensation of stray fields can be taken care of along each axis. For the experiments in this chapter, only the anti-Helmholtz coils and the electrodes are used.

To create the Rydberg atoms, two excitation beams are focused at the center of the secondary MOT. The energy-level diagram is shown in Fig. 6.2 (far right arrows) and is the same as in the EIT configuration. The lower-transition beam is 780 nm and the upper-transition is 480 nm. Once the Rydberg atoms are created, there are

two detection methods that can be implemented. One method is observation of the EIT window. However, observation of an EIT signal in a cold-atom sample is not as straight-forward as in vapor cells. The other method, which is initially preferred for Rydberg atom detection, is field ionization Both detection methods are implemented.

One important feature of the chamber is the beryllium-copper needle known as the tip imaging probe (TIP). By applying a high voltage ($\sim$ 1600 V) to the TIP, the Rydberg atoms are field ionized and the resulting ions are directed through an ion lens toward a microchannel plate (MCP). The resulting impact signals are then counted using a SR400 Photon Counter. (Note: the term SR400 will be used so it is not confused with the SPCM.) The TIP is advantageous for spatial magnification of the Rydberg atoms, the details of which are discussed below.

Specific details regarding MOTs and detection methods can be seen in previous works and are not discussed here [68, 70].

6.2 Imaging and Magnification

One important aspect of this vacuum chamber is its imaging capabilities. As mentioned before, the Rydberg atoms are ionized by applying a high voltage to the TIP and detecting the resulting ions on the MCP. For the experiments performed here, it is not sufficient to simply count the number of detected ions. It is also important to know their locations, and the MCP allows for this. In order to know the locations accurately, the imaging must be calibrated which includes the magnification and image characteristics.

When a high voltage is applied to the TIP, a radial electric field is created, resulting in a large magnification of the atom separations. To determine the magnification factor, a double slit mask is put in the 480-nm laser beam path before it is focused into the chamber. The resulting interference pattern is at the focus in front of the TIP. For a double slit, the fringe maxima are separated by $y = \frac{\lambda f}{d}$ where λ is the wavelength of

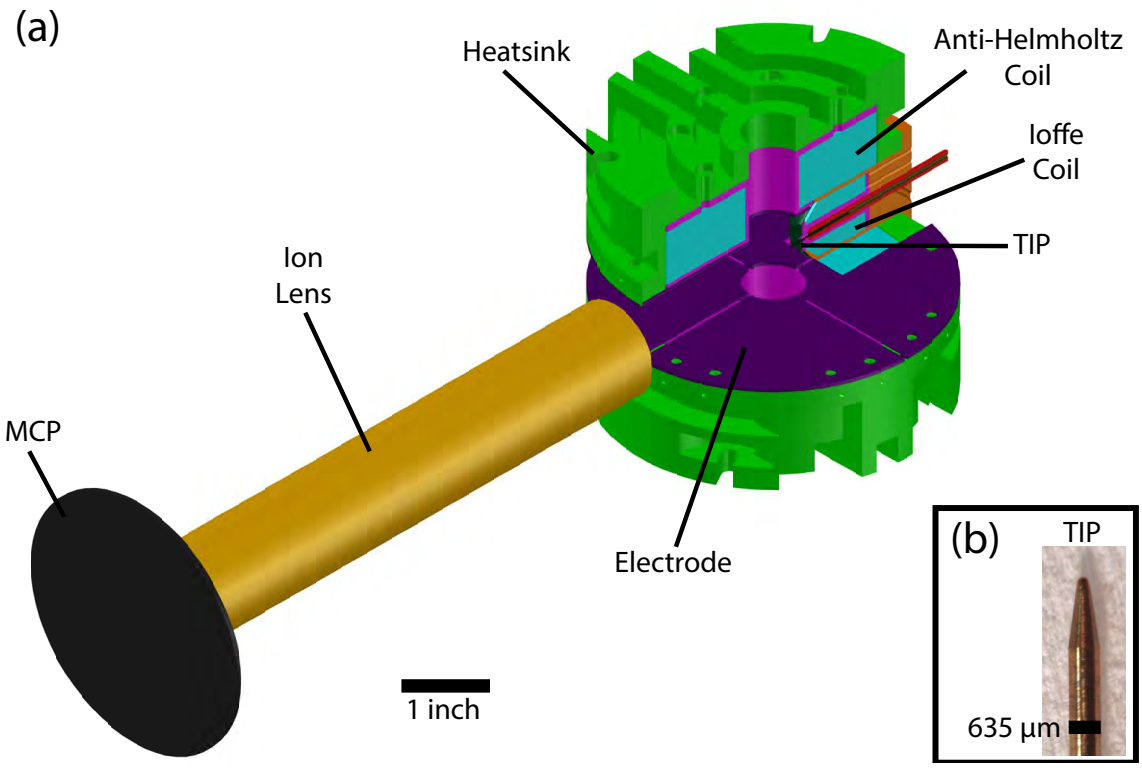

Figure 6.4: (a) Cutout of the internal components of the main chamber including MOT coils, Ioffe Coil, TIP, electrodes, ion lens, and MCP. Coloring is artificial to highlight various components. See text for details. (b) Photo of the tip imaging probe (TIP).

the light, f is the focal length of the lens (*i.e.* the location of the imaging plane), and d is the separation of the slits. In this case, $\lambda = 480$ nm, $f = 40$ cm, and $d = 12$ mm, resulting in fringes that are 16 μm apart. Using the double slit projection for the blue beam and with the MOT light providing the light for the lower transition, images of the ions hitting the MCP are recorded. When many of these images are summed, the interference pattern reveals itself. By measuring the spacing of these fringes and knowing the calibration of the imaging camera (44.4 μm/pixel), the magnification factor can be determined.

Figure 6.5(a-c) show the interference pattern revealed by summing 1,000 images for different distances of the TIP from the excitation volume using the $|31S\rangle$ Rydberg state. TIP distances of 0.5 mm, 0.75 mm, and 1.0 mm are shown for (a) to (c),

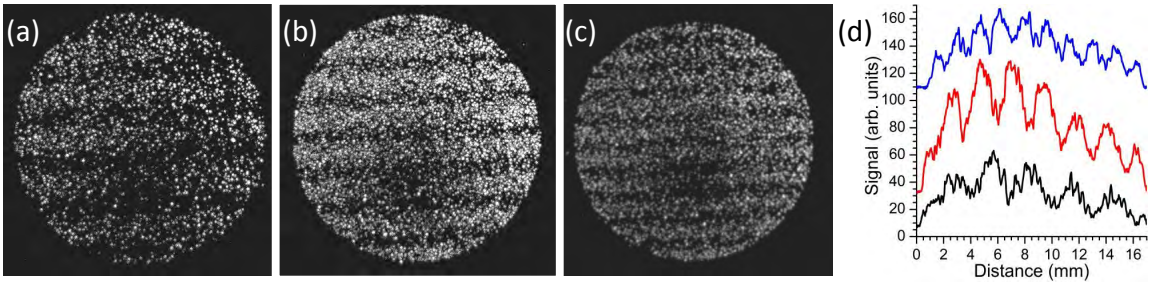

Figure 6.5: Fringe detection for various distances of the TIP from the excitation volume. The images are sums of images from 1,000 field ionization pulses of the $|31S\rangle$ Rydberg state. TIP distances are (a) 0.5 mm, (b) 0.75 mm, and (c) 1.0 mm. (d) Profiles of the fringes for 0.5 mm (black), 0.75 mm (red) and 1.0 mm (blue). The corresponding magnification factors are 170×, 135×, and 95×, respectively.

respectively. For each of these images, the optical beams were fixed and the location of the TIP was adjusted with the actuator (see Fig. 6.1). Figure 6.5(d) shows the profiles of the fringes for 0.5 mm (black), 0.75 mm (red) and 1.0 mm (blue). The corresponding magnification factors are 170×, 135×, and 95×. The separation of the fringes of a summed image divided by the separation of the fringes at the beam focus gives the magnification factor.

A high spatial magnification is needed in order to resolve two atoms close to each other. Two Rydberg atoms are separated by distances greater than the blockade radius due to the van der Waals interaction [71, 74]. Additionally, the blockade radius scales as $(n^*)^{11/6}$ where n^* is the effective principal quantum number [71], so Rydberg atoms with higher principal quantum numbers are easier to spatially resolve for a given magnification.

The closer the excitation volume is to the TIP, the more kinetic energy the ions receive, and the magnification is higher. This magnification comes at the cost of the size and density of the MOT due to scattering of MOT light off the TIP. There are experimental optimization techniques to circumvent this issue such that a sufficiently dense MOT may be obtained. These include adjusting the MOT gradient, magnetic bias fields, laser powers, laser detunings, and beam alignments.

6.3 EIT Configuration

For the EIT experiments performed in the vacuum chamber, the excitation beams pass in front of the TIP, only ~ 0.5 mm away. The 780-nm (probe) beam reflects off the internal vacuum mirror, is focused in front of the TIP, exits the chamber through a window, passes through a dichroic mirror, and is incident on a photodiode. For preliminary measurements, a standard photodiode is used. The 480-nm (coupler) beam reflects off the dichroic mirror and counter-propagates with the probe beam. The probe beam has a power of $\leq 1 I_{sat}$ and the coupler beam power can be $\geq$50 mW. The exact powers of each beam are varied to obtain an optimal EIT signal. Both beams are focused in front of the TIP to a waist ω_0 of 9 μm for the probe and 12 μm for the coupler. The beam sizes are chosen to be so small to reduce the likelihood of creating multiple Rydberg atoms along the diameter of the beams.

When using a thermal sample, continuous probing of the sample is simple because only the EIT lasers are present. However, for cold atom samples there are additional lasers for the trapping and cooling of the atoms. As a result, the EIT sample can only be taken in a pulsed mode after the MOT lasers are switched off. The repetition rate can be tens of Hz, provided that the sample does not undergo much motion when the MOT lasers are off. The atoms can be recaptured after each EIT pulse, so there is negligible loading time.

In the setup used here, both the probe and the coupling lasers are locked in order to know what their frequencies are during each optical pulse, as well as to have more control over the lasers. Since the 480-nm laser is locked using the Fabry-Pérot cavity, it is not ideal to scan this laser to obtain the EIT spectra. Stepping the frequency of this laser is relatively slow compared to the rest of the experimental cycle. Additionally, there is a greater chance of hysteresis in frequency due to the mechanical nature of the motor used with the cavity. For greater accuracy, the probe frequency is stepped using computer control of the frequency driver of the AOM in

the beam path. Using the AOM results in highly repeatable results, as well as quick switching.

To obtain the EIT curve, the probe frequency is set and the signal averaging is completed and recorded. The probe frequency is then stepped and the process is repeated. By stepping through a range of probe frequencies without the application of the coupling beam, the absorption line of the $|5S_{1/2}\rangle \rightarrow |5P_{3/2}\rangle$ transition is obtained. The linewidth for this system is slightly larger. Application of the coupling laser with sufficient power results in the emergence of the EIT window.

6.3.1 EIT in Thermal vs. Cold-Atom Samples

There are a few differences between thermal and cold-atom EIT. In a thermal sample, the direction that the beams propagate is very important for a few reasons. First, the Doppler factor (see Section 2.2.2 and Appendix A) depends on the directionality of the beams because they are substantially different in wavelength and the atoms have a significant velocity. Second, the quality of the EIT depends on the beam directions, particularly in 3-photon EIT [21]. For certain configurations, the amplitude of the EIT signal is very weak against the background level.

For a cold-atom sample, the direction of the laser beams do not matter. Because atoms are effectively stationary, there is no Doppler mismatch. Therefore, the beams can be co- or counter-propagating. For the vacuum chamber setup, the two beams are counter-propagating since it is the simplest way to allow the beams to enter the chamber.

While the Doppler profile of the thermal sample is $\sim$ 1 GHz, the background signal of the cold-atom sample is the $|5S_{1/2}, F = 2\rangle \rightarrow |5P_{3/2}, F = 3\rangle$ absorption line. The absorption linewidth is limited by the natural linewidth which is only 6 MHz [41], but is slightly larger for the measurements here. In terms of EIT, the signal is much narrower for cold atoms (widths of < 1 MHz are attainable). However, the conditions

to achieve cold-atom EIT are stricter than the conditions for thermal samples and challenges not present for vapor cell measurements must be overcome in order to obtain EIT which will be outlined below.

6.4 Detection Using a Photodiode

To initially observe the EIT line, a standard photodiode (similar to the one used in Chapter IV) is used. After the dichroic mirror, the probe beam is focused onto the photodiode. The signal is then sent though an amplifier and then to the oscilloscope for observation and recording. A longpass filter is placed immediately before the photodiode in order to eliminate stray blue light that would be detected otherwise.

The signal appears on the oscilloscope as a square pulse whose height depends on the amount of probe transmission instead of the spectra seen in previous chapters. Figure 6.6 shows examples of such pulse recordings for the maximum light signal (black), absorption (red), and EIT (blue). The pulse signals are initially averaged on the oscilloscope. For each averaged pulse, the value of its amplitude is extracted by averaging over the flat part of the signal. The ringing at the beginning and the end of the pulse is not included. Curves of the absorption profile and EIT are seen when plotting the PD voltage as a function of probe frequency.

During the EIT pulses, the path of the secondary MOT Master laser beam is blocked by turning off the amplitude of the AOM driver. The Repumper and primary MOT beams are not blocked and result in a constant offset in the PD voltage. This offset is subtracted and not included in the voltage measurements of the probe beam.

When the coupling laser is applied, the EIT window emerges. If too little coupler power is used, then the EIT window is not present. Figure 6.7 shows the $|30D_{5/2}\rangle$ EIT line for various coupling laser powers. As the coupling laser power is increased, the EIT signal strength increase. When too much power is in the coupling beam, the EIT signal becomes very broad (not shown). Both of these effects have been seen

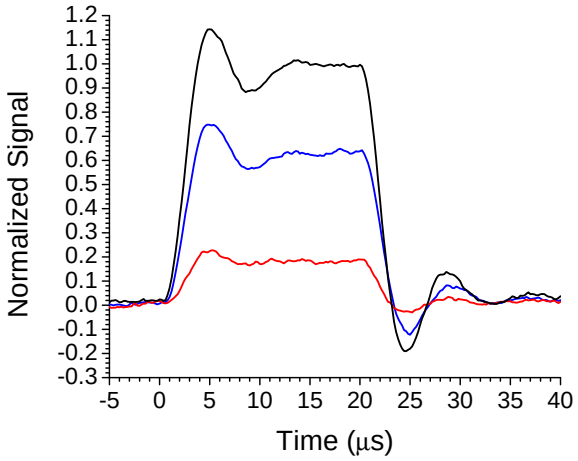

Figure 6.6: Normalized photodiode signals during the optical pulses for $|32S\rangle$ EIT. Signals are normalized by the maximum probe power. Scans are averages of 50 pulses. The black pulse is the maximum probe level taken with the secondary Master blocked so no atoms are present. The red pulse is the absorption of the atoms with the probe applied and no coupler. The blue pulse is the EIT signal with the coupling laser applied.

elsewhere as well [39], reiterating that the system is behaving as expected.

A series of neutral density filters are used to adjust the maximum power of the probe beam. Moreover, the power is too low to be measured with a standard power meter. For a cold-atom sample, the amount of probe power required to obtain a sufficient EIT signal depends on the principal quantum number n of the Rydberg atom. For higher values of n, lower probe power is required due to the Rydberg blockade effect [52]. Thus, EIT signals can only been seen using a standard photodiode up to $n \approx 40$ due to the photon rate limitation (see Section 6.5.1).

An alternative method of detection is required to obtain signals at higher values of n. Again, this is required because the experiment presented here also involves looking at the spatial image of the atoms, and a sufficiently high n is needed to resolve the blockade radius. To rectify the issue of detecting low probe powers, a single-photon-counting module is implemented in place of the photodiode.

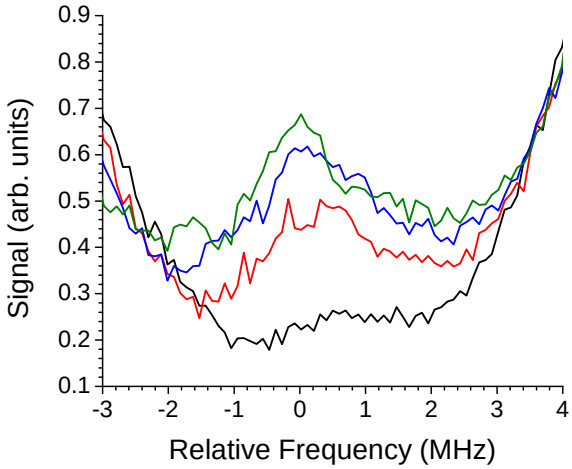

Figure 6.7: EIT signals for various coupling lasers powers applied to the $|30D_{5/2}\rangle$ state. The black curve is with the lowest coupler power and stronger signals are the result of more power in the laser beam. The probe power is kept constant. Signals are averages of 60 scans and given in arbitrary units.

6.5 Single-Photon-Counting Module (SPCM)

The single-photon-counting module (SPCM) detects single photons and outputs a 10 ns TTL pulse for each one. The output pulses of the SPCM are sent to the oscilloscope to monitor pulse timings, as well as to the SR400 (on a different channel than the MCP) to be counted. The value(s) of both devices can be individually recorded. Certain factors must be considered when using this device, as will be outlined in the following sections.

6.5.1 Photon Rates

The photon rate of the light determines the amount of light that is required for EIT. This parameter will be experimentally varied to see the effect on the signal, as well as to obtain the optimal signal.

To obtain an upper estimate on the allowed power for the probe, the following estimate is used. The photon rate is given by $\frac{v_c N_T}{2r_B}$ where v_c is the velocity of light in the EIT medium (< 1000 m/s) [45], N_T is the number of atoms per cross-section of the beam, and r_B is the Rydberg blockade radius. For $n \approx 70$ Rydberg atoms,

the blockade radius is ~ 10 μm [71, 75], so $N_T \lesssim 10$. Thus, the rate is $\frac{1000\ m/s*10}{2*10\mu m} \sim 10^9\ s^{-1}$. The energy of a each probe photon (E_{photon}) is $\frac{hc}{\lambda} = 2.5 \times 10^{-19}$ Joules. The power of the beam is determined to be (rate)*(E_{photon}) ~ 250 pW.

6.5.2 Light Shielding

When using the SPCM, it is important to avoid detecting any light other than the probe beam. Stray light will result in extra counts, and too much light could damage the device. When the PD is used, the amount of stray light is simply subtracted from the total signal. While this can be done during the setup of the SPCM, it is not permissible in the experiment. One of the objectives is to look at the correlation of when the photons exit the EIT medium and are detected. Signals from stray light will invalidate any results obtained. A few preventative measures are necessary when using the SPCM. The room lights are off and black-out curtains surround the chamber to shield lights from computers and other electronics. In the path of the probe beam after the dichroic mirror, there is a pinhole for further shielding. The SPCM and the pinhole setup are surrounded by black cardboard as well. The longpass filter previously used is no longer needed because stray blue light is shielded with the cardboard. While all of these measures may seem excessive, components were added over the course of setting the device up because they were required.

Despite all of the above preventative measures taken, some of the 780-nm light still reaches the SPCM from the laser cooling light, specifically the Repumper. To rectify this issue, all of the lasers paths are blocked with commercial shutters before the fiber input. This eliminates any 780-nm laser light during the EIT measurement while the SPCM is on. The addition of the shutters requires a slower repetition rate to ensure sufficient loading of the secondary MOT. Currently, the rate of the EIT optical pulses is 1 Hz.

6.5.3 Absorption and EIT Curves

When using the SPCM, absorption and EIT curves are taken while stepping the probe laser frequency, similar to what was done with the PD. Now, instead of recording an average voltage, the average number of photons per optical pulse is recorded using the SR400. Curves obtained using the SPCM are now seen when plotting the number of counts as a function of probe frequency, as seen in Fig. 6.8.

Another issue that must be considered when using the SPCM that was negligible for the PD is how the power of the probe beam changes as a function of frequency. This is due to the inherent efficiency of the AOM [76], as well as the angle of deflection. To mitigate this issue, normalized absorption and EIT curves are taken by first recording the number of counts from the SPCM as a function of probe frequency without the coupling laser on and no atoms present ("No Atoms"). This yields the background maximum light level. As expected, this signal is zero when the probe light is off. Next, the same signal is recorded with atoms present ("No Blue"). Finally, the coupling light is turned on and the EIT signal is obtained ("EIT"). As a result of these three scans, there are three normalized scans:

1. Normalized absorption curve: $\frac{\text{“No Blue”}}{\text{“No Atoms”}}$
2. Normalized EIT curve: $\frac{\text{“EIT”}}{\text{“No Atoms”}}$
3. Net EIT signal: $\frac{\text{“EIT”}}{\text{“No Atoms”}} - \frac{\text{“No Blue”}}{\text{“No Atoms”}}$.

Clean curves of the "No Blue" and "No Atoms" have been seen. Finding a clean EIT signal is in progress. Figure 6.8 shows the raw average of SPCM counts for 50 pulses with the "No Blue" curve in black and the "No Atoms" curve in red. Here, the change in power as a function of frequency due to the AOM is apparent. However, it is symmetric about the center of the absorption profile. The absorption curve is larger than the natural linewidth due to the laser linewidth. Further work will be required to reduce the width if it is needed.

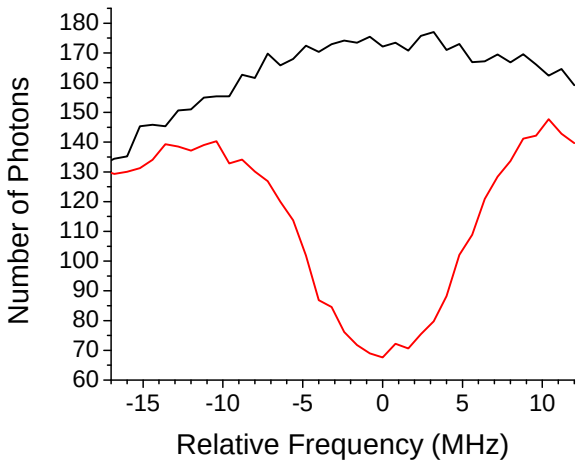

Figure 6.8: Raw average of SPCM counts for 50 pulses with the "No Blue" curve in black and the "No Atoms" curve in red.

6.6 Combining Field Ionization and EIT

Once the setup is able to obtain a sufficient EIT curve using the SPCM, the next step is to integrate EIT measurements with together with field ionization and detection of Rydberg atoms. The timing sequence must be carefully considered. Atoms are initially loaded from the primary MOT to the secondary MOT. During this time, the MOT lights are on, and the pusher has a period of 100 μs and duty cycle of 10%. The pusher is pulsed to allow the primary MOT to refill before loading. After the loading is complete, the MOT beams are shut off using an AOM for the Master laser beams, as well as the shutters for both the Master and Repumper beams.

Once the beams are extinguished, the EIT probe and coupling beam are turned on for about 20 μs. During this time, the SPCM is gated open and detects the probe photons. Once the optical excitation beams are off and the SPCM is gated closed, a high voltage (1600 V) is applied to the TIP to field ionize the Rydberg atoms. The ions are directed to the MCP where the MCP phosphor emits a bright spot at this location. A camera's exposure is gated during this detection time.

The above procedure is outlined for one experimental cycle. For each cycle, the trace from the SPCM and the picture from the MCP camera are recorded. After a

series of images is taken for one set of parameters, the next set is acquired. Once a complete series is taken, the results are processed and analyzed.

As of the publication of this thesis, implementation of combining these two features is in progress. The following sections discuss the analysis procedure that will occur when data has been obtained. Moreover, the expected outcomes will be discussed.

6.7 Correlation Analysis Procedure

The main goal of the current experiment is to observe the spatial and temporal correlations of the atoms and light, respectively, while they are in an EIT configuration. To observe two-body correlations, the second order correlation function is used. Conceptually, this can be understood as how the atoms (photons) are located in space (time) with respect to another atom (photon). The details of how this information is extracted is slightly different for the two properties, but the analyses are very similar.

6.7.1 Time Correlation

For the second-order temporal correlation function, the equation is given by

$$g^{(2)}(\tau) = \frac{\langle N(t)N(t+\tau)\rangle}{\langle N(t)\rangle\langle N(t+\tau)\rangle} \tag{6.1}$$

where $N(t)$ is the number of counts detected at time t [77]. Values of $g^{(2)}(\tau)$ less than 1 correspond to anti-bunched photons and values greater than 1 correspond to bunched photons.

In order to obtain $g^{(2)}(\tau)$, the signal from the SPCM is initially sent to an oscilloscope and recorded for analysis. The time of each peak is recorded into a new file. For each peak, the time separation of all of the other peaks is then calculated and recorded. The resulting histogram values are then multiplied by $\frac{T}{T-\tau}$, where T is the length of the SPCM gate and τ is the time between pairs of peaks, in order to give

proper weighting to the longer time intervals. The oscilloscope can take scans with a high sampling rate, so the time differences between photons may need to be binned into slightly larger time intervals in order to reduce the noise in the signal.

Since there are strong nonlinear effects in the EIT sample, anti-bunching of the photons is expected to occur on a timescale of < 500 ns [10, 52]. Thus, the fine temporal resolution of the SPCM and detection equipment is important. Anti-bunching has only been seen for strongly interacting S state Rydberg atoms and not D state atoms [10]. In this system, both S and D states will be investigated.

6.7.2 Spatial Correlation

The technique used for spatial imaging has previously been used in the Raithel group to investigate Rydberg-atom interactions [70–72, 78]. The process is similar to that used for temporal correlations, but with more required processing due to both the format of the raw signal and the extension from 1D (*i.e.* time) to 2D (*i.e.* x and y coordinates).

While the oscilloscope traces have clear peaks of near-uniform height with little background signal, the pictures taken of the MCP are more complex. The bright spots that indicate a detected ion are a few camera pixels in diameter and are not uniform in intensity. Moreover, for small enough principal quantum number, two spots that intersect on the camera can be recorded as one spot. This illustrates another reason why large magnification and sufficiently large quantum numbers are used.

After the images are pre-processed to remove the background and smooth the noise of the image, the peaks are detected using another algorithm and their positions are recorded. The radius between each pair of peaks is recorded, and the resulting 2D histogram is normalized. More details can be seen in Refs. [70, 71, 78]. Figure 6.9 shows a resulting correlation image after 1,000 images for the $|31S\rangle$ Rydberg state are processed.

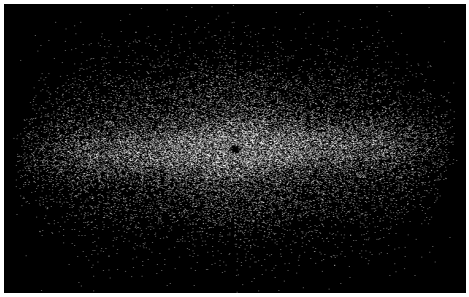

Figure 6.9: Experimental pair correlation image for Rydberg atoms for 1,000 field ionization pulses of the $|31S\rangle$ state.

One feature that may need to be addressed that has been observed is ion feedback [78, 79]. This occurs when the electron that is ionized from the Rydberg atom impacts the TIP and releases a secondary ion. The resulting ion impacts the MCP close to the primary ion. This manifests as a pattern within a few pixels of the center of the correlation image. To mitigate this issue, any two ions detected within a few pixels of each other (and a fraction of the blockade radius) are replaced by the center-of-mass position of the two apparent ions. This issue is not apparent in Fig. 6.9 but will need to be verified in correlations for large n Rydberg atoms when data is taken.

6.8 Conclusion

This chapter presented progress toward implementing cold-atom EIT. Unique aspects of the vacuum chamber were discussed. Preliminary measurements of EIT and imaging of Rydberg atoms were given.

Currently, work is being done to observe EIT with the SPCM and implement it in conjunction with field ionizing the Rydberg atoms and detecting their resulting positions. Code for image processing and analysis has been written but has yet to be tested with sample data. One check for the code is comparing correlation from this setup to published correlations obtained with similar experimental settings. From here, the correlation functions $g^{(2)}(\mathbf{r})$ and $g^{(2)}(\tau)$ for atoms and photons in the EIT configuration can be extracted and its physical implications discussed.

CHAPTER VII

Future Directions and Conclusion

7.1 Vapor Cell Measurements

The work presented in this thesis shows the development of using Rydberg atoms and electromagnetically induced transparency in order to measure strong RF fields with high sensitivity. The technique of using Rydberg-EIT to measure RF fields has recently been developed, and there are a wide range of possibilities for it. The performed measurements advance the progress toward using this technique to develop an atomic standard for electric fields at NIST and other National Metrology Institutes.

In the studies presented in the preceding chapters, a wide variety of electric-field measurements were performed and modeled, thus expanding the application of Rydberg-EIT. Various principal quantum numbers were investigated in order to study different RF frequencies, as well as to show the broadband nature of this all-optical measurement technique. $|Rydberg\rangle \rightarrow |Rydberg\rangle$ transitions were driven in the weak-field, moderate-field, and strong-field regimes to investigate the degree of state mixing and the resulting effect on the energy levels. Moreover, both one- and two-photon transitions were investigated in these regimes. For the weak-field cases, perturbation theory was used to model the spectra. Floquet theory is required to accurately model the spectra in the moderate- and strong-field regimes. This thesis presented modeling of the spectroscopic signal, as well as the associated line strength.

Spectral features resulting from field inhomogeneities within the measurement volume were accurately modeled as well using a straightforward procedure that accounted for the different weighting of the multiple field domains. In order to model arbitrary RF electric fields accurately, field domains need to be accounted for, and one method of doing so was presented here. The strong-field measurements performed were the highest field measurements done using this technique at the time of their publication. RF fields up to 296 V/m within a $\pm 0.35\%$ relative uncertainty were measured. This error is also more than an order of magnitude better than the current standard using dipole antennas. Such a small uncertainty is the direct result of unique spectroscopic features that allow for higher accuracy when comparing experimental and calculated spectral maps. Further work could be done to improve the uncertainty in the strong-field regime by utilizing other Rydberg states and transitions that provide higher-resolution spectral features.

Advancement in the frequency range, precision, and sensitivity of Rydberg-EIT make it a good candidate to become the new atomic standard for RF electric field measurements. This is because the splitting of the EIT line is linear in the weak-field regime and exclusively relies on fundamental constants (*i.e.* Planck's constant and dipole moments, the latter of which are know to within 0.1%). It is speculated that it may be possible to achieve measurements in a field of < 10 μV/m by using lasers with narrower linewidths, low-noise detection, and squeezing [25]. On the other end of the power range in the strong-field regime, fundamental limitations due to the underlying atomic physics eventually occur when the Rydberg atoms experience substantial microwave-ionization rates [7]. For the method to be limited by microwave ionization, the microwave power has to be much larger than what is used in this work.

Currently, there is an ongoing effort by a few groups to increase the sensitivity in very weak fields [25, 32, 34] and in strong fields [35]. Additionally, work is being done to make this technique portable, as well as development of commercial atom-

based sensors [80]. Furthermore, Rydberg-EIT is being used as a technique for strong magnetic field measurements as well [81, 82].

7.2 Vacuum Chamber Setup

The vacuum chamber presented in this thesis is at its beginning stages with regard to its scientific capabilities. Currently, the individual components of the experiment have been established and work is being done to fully implement them, including optimization of the settings. Field ionization and Rydberg ion detection with a high magnification is in place. EIT has been seen using a standard photodiode, but has yet to be conclusively observed with the single-photon-counting module. Once it is observed, the two observation techniques will be combined and the resulting $g^{(2)}(\mathbf{r})$ and $g^{(2)}(\tau)$, respectively, will be calculated and the results extracted.

There are many experiments that are planned to take place in this chamber that utilize unique attributes of the setup. Some of these experiments involve EIT, possibly with the addition of microwaves or other RF sources. The TIP in the chamber provides high magnification of the Rydberg atom positions. This is currently being implemented, and other experiments can be done that exploit this capability, both in MOTs and in ultra-cold atom samples. The chamber was designed for magnetic trapping and Bose-Einstein condensates. Cold, dense atomic samples provide a unique platform for investigation of various topics. One such topic is Rydberg-ground state molecules, which is another area I worked on during my graduate studies [83, 84]. Dense samples are needed for the production of such molecules. The chamber could further investigate the creation and properties of Rydberg-ground state molecules, as well as Rydberg-Rydberg molecules.

APPENDIX

APPENDIX A

Doppler Factor

When comparing the frequency separation between spectral features, it is important to account for the Doppler mismatch that the thermal sample of atoms sees. Consider the example energy level diagram seen in Fig. A.1. There is a ground state with a single sublevel, an intermediate state with multiple sublevels (*i.e.* hyperfine states), and a Rydberg state with multiple sublevels (*i.e.* fine structure).

Scanned Probe and Locked Coupler

Let the probe laser (driving the transition from the ground state to the intermediate state) be scanning and the coupling laser (driving the transition from the intermediate state to the Rydberg state) be fixed. Define the following frequencies with the subscript denoting the EIT line:

$$f^b = \text{frequency of coupling laser} \tag{A.1}$$

$$f_i^p = \text{frequency of probe laser} \tag{A.2}$$

$$f_i = \text{frequency of lower transition} \tag{A.3}$$

$$f_i' = \text{frequency of Rydberg transition.} \tag{A.4}$$

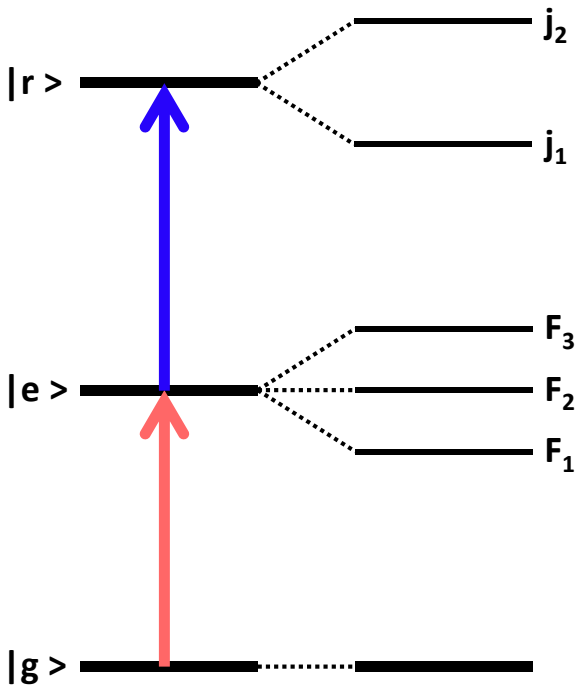

Figure A.1: Example energy level diagram. The left part show the two-photon transition from a ground state ($|g\rangle$), through an intermediate excited state ($|e\rangle$), to a Rydberg state ($|r\rangle$). The right part shows the break-down of each main level. The $|g\rangle$ state is one level while the $|e\rangle$ state has hyperfine levels and the $|r\rangle$ state has fine structure levels.

For atoms of a fixed velocity class,

$$f_i' = f^b + k_c v \tag{A.5}$$

$$f_i = f_i^p - k_p v \tag{A.6}$$

where k_p (k_c) is the wavenumber of the probe (coupling) beam. The equations have opposite sign because the two beams are counter-propagating. Removing v from the equations yields

$$f_i = f_i^p + \frac{k_p}{k_c}(f^b - f_i'). \tag{A.7}$$

The difference in frequency between two peaks ("i" and "j") is given by

$$(f_i - f_j) = (f_i^p - f_j^p) - \frac{k_p}{k_c}(f_i' - f_j') \tag{A.8}$$

$$\Delta f = \Delta f^p - \frac{k_p}{k_c}\Delta f' \tag{A.9}$$

$$\Delta f = \Delta f^p - \frac{\lambda_c}{\lambda_p}\Delta f' \tag{A.10}$$

If the intermediate state is fixed (*i.e.* $\Delta f = 0$), then $\Delta f^p = \frac{\lambda_c}{\lambda_p}\Delta f'$. Since $\Delta f'$ is the actual frequency of the transition, in this case the measured fine structure splitting between Rydberg states is scaled by $\frac{\lambda_c}{\lambda_p}$.

If the Rydberg state is fixed (*i.e.* $\Delta f = -\Delta f'$), then $\Delta f^p = (1 - \frac{\lambda_c}{\lambda_p})\Delta f$. This means that the actual hyperfine splitting (Δf) is scaled by $(1 - \frac{\lambda_c}{\lambda_p})$.

Locked Probe and Scanning Coupler

Let the probe laser be fixed and the coupling laser be scanning. Similarly, define the following frequencies with the subscript denoting the EIT line:

$$f_i^b = \text{frequency of coupling laser} \tag{A.11}$$

$$f^p = \text{frequency of probe laser} \tag{A.12}$$

$$f_i = \text{frequency of lower transition} \tag{A.13}$$

$$f_i' = \text{frequency of Rydberg transition.} \tag{A.14}$$

For atoms of a fixed velocity class,

$$f_i' = f_i^b + k_c v \tag{A.15}$$

$$f_i = f^p - k_p v \tag{A.16}$$

Removing v from the equations yields

$$f_i^c = f_i' + \frac{k_c}{k_p}(f_i - f^p) = f_i' + \frac{\lambda_p}{\lambda_c}(f_i - f^p) \tag{A.17}$$

The difference in frequency between two peaks ("i" and "j") is given by

$$\Delta f^c = \Delta f' + \frac{\lambda_p}{\lambda_c}\Delta f \tag{A.18}$$

If the intermediate state is fixed (*i.e.* $\Delta f = 0$), then $\Delta f^c = \Delta f'$, meaning the measured fine structure splitting is the actual splitting, without a scaling factor. If the Rydberg state is fixed (*i.e.* $\Delta f = -\Delta f'$), then $\Delta f^c = (\frac{\lambda_p}{\lambda_c} - 1)\Delta f$, meaning the actual hyperfine splitting (Δf) is scaled by $(\frac{\lambda_p}{\lambda_c} - 1)$.

BIBLIOGRAPHY

BIBLIOGRAPHY

[1] C.L. Holloway, J.A. Gordon, S. Jefferts, A. Schwarzkopf, D.A. Anderson, S.A. Miller, N. Thaicharoen, and G. Raithel. Broadband Rydberg atom-based electric-field probe for SI-traceable, self-calibrated measurements. *IEEE Transactions on Antennas and Propagation*, 62(12):6169–6182, Dec 2014.

[2] D. A. Anderson, S. A. Miller, G. Raithel, J. A. Gordon, M. L. Butler, and C. L. Holloway. Optical measurements of strong microwave fields with Rydberg atoms in a vapor cell. *Phys. Rev. Applied*, 5:034003, Mar 2016.

[3] D. A. Anderson, A. Schwarzkopf, S. A. Miller, N. Thaicharoen, G. Raithel, J. A. Gordon, and C. L. Holloway. Two-photon microwave transitions and strong-field effects in a room-temperature Rydberg-atom gas. *Phys. Rev. A*, 90:043419, Oct 2014.

[4] Christopher L. Holloway, Joshua A. Gordon, Andrew Schwarzkopf, David A. Anderson, Stephanie A. Miller, Nithiwadee Thaicharoen, and Georg Raithel. Sub-wavelength imaging and field mapping via electromagnetically induced transparency and Autler-Townes splitting in Rydberg atoms. *Applied Physics Letters*, 104(24):–, 2014.

[5] D. A. Anderson S. A. Miller and G Raithel. Radio-frequency-modulated Rydberg states in a vapor cell. *New Journal of Physics*, 18(5):053017, 2016.

[6] Stephanie A. Miller, David A. Anderson, Andrew T. Cadotte, and Georg A Raithel. Miniature mechanical shutter, September 17 2015. US Patent 20,150,263,595.

[7] T.F. Gallagher. *Rydberg Atoms*. Cambridge University Press, New York, NY, USA, 1994.

[8] A. Osterwalder and F. Merkt. Using high Rydberg states as electric field sensors. *Phys. Rev. Lett.*, 82:1831–1834, Mar 1999.

[9] Y. O. Dudin and A. Kuzmich. Strongly interacting Rydberg excitations of a cold atomic gas. *Science*, 336(6083):887–889, 2012.

[10] Thibault Peyronel, Ofer Firstenberg, Qi-Yu Liang, Sebastian Hofferberth, Alexey V Gorshkov, Thomas Pohl, Mikhail D Lukin, and Vladan Vuletić. Quantum nonlinear optics with single photons enabled by strongly interacting atoms. *Nature*, 488(7409):57–60, 2012.

[11] M. D. Lukin. Colloquium: Trapping and manipulating photon states in atomic ensembles. *Rev. Mod. Phys.*, 75:457–472, Apr 2003.

[12] D. Maxwell, D. J. Szwer, D. Paredes-Barato, H. Busche, J. D. Pritchard, A. Gauguet, K. J. Weatherill, M. P. A. Jones, and C. S. Adams. Storage and control of optical photons using Rydberg polaritons. *Phys. Rev. Lett.*, 110:103001, Mar 2013.

[13] Jonathan D. Pritchard. *Rydberg Atom Interactions*, pages 27–36. Springer Berlin Heidelberg, Berlin, Heidelberg, 2012.

[14] T. Cubel Liebisch, A. Reinhard, P. R. Berman, and G. Raithel. Atom counting statistics in ensembles of interacting Rydberg atoms. *Phys. Rev. Lett.*, 95:253002, Dec 2005.

[15] Kilian Singer, Markus Reetz-Lamour, Thomas Amthor, Luis Gustavo Marcassa, and Matthias Weidemüller. Suppression of excitation and spectral broadening induced by interactions in a cold gas of Rydberg atoms. *Phys. Rev. Lett.*, 93:163001, Oct 2004.

[16] R. F. Stebbings. *Rydberg states of atoms and molecules*. Cambridge University Press, 1983.

[17] S. E. Anderson, K. C. Younge, and G. Raithel. Trapping Rydberg atoms in an optical lattice. *Phys. Rev. Lett.*, 107:263001, Dec 2011.

[18] A. K. Mohapatra, T. R. Jackson, and C. S. Adams. Coherent optical detection of highly excited Rydberg states using electromagnetically induced transparency. *Phys. Rev. Lett.*, 98:113003, Mar 2007.

[19] Michael Fleischhauer, Atac Imamoglu, and Jonathan P. Marangos. Electromagnetically induced transparency: Optics in coherent media. *Rev. Mod. Phys.*, 77:633–673, Jul 2005.

[20] A. Krishna, K. Pandey, A. Wasan, and V. Natarajan. High-resolution hyperfine spectroscopy of excited states using electromagnetically induced transparency. *EPL (Europhysics Letters)*, 72(2):221, 2005.

[21] Christopher Carr, Monsit Tanasittikosol, Armen Sargsyan, David Sarkisyan, Charles S. Adams, and Kevin J. Weatherill. Three-photon electromagnetically induced transparency using Rydberg states. *Opt. Lett.*, 37(18):3858–3860, Sep 2012.

[22] Surajit Sen, Tushar Kanti Dey, Mihir Ranjan Nath, and Gautam Gangopadhyay. Comparison of electromagnetically induced transparency in lambda, cascade and vee three-level systems. *Journal of Modern Optics*, 62(3):166–174, 2015.

[23] K.-J. Boller, A. Imamoğlu, and S. E. Harris. Observation of electromagnetically induced transparency. *Phys. Rev. Lett.*, 66:2593–2596, May 1991.

[24] L Essen and JVL Parry. An atomic standard of frequency and time interval: a caesium resonator. *Nature*, 176(4476):280–282, 1955.

[25] Jonathon A. Sedlacek, Arne Schwettmann, Harald Kübler, Robert Löw, Tilman Pfau, and James P. Shaffer. Microwave electrometry with Rydberg atoms in a vapour cell using bright atomic resonances. *Nat. Phys.*, 8:819–824, November 2012.

[26] Dmitry Budker and Michael Romalis. Optical magnetometry. *Nature Physics*, 3:227–234, April 2007.

[27] D. Sheng, S. Li, N. Dural, and M. V. Romalis. Subfemtotesla scalar atomic magnetometry using multipass cells. *Phys. Rev. Lett.*, 110:160802, Apr 2013.

[28] K. Matloubi. A broadband, isotropic, electric-field probe with tapered resistive dipoles. In *Instrumentation and Measurement Technology Conference, 1993. IMTC/93. Conference Record., IEEE*, pages 183–184, May 1993.

[29] D.A. Hill, M. Kanda, E.B. Laren, G.H. Koepke, and R.D. Orr. Generating standard reference electromagnetic fields in the nist anechoic chamber, 0.2 to 40 GHz. *NIST Technical Note 1335, National Institute of Standards and Technology, Boulder, CO, USA*, 1990.

[30] Ieee standard letter designations for radar-frequency bands. *IEEE Std 521-2002 (Revision of IEEE Std 521-1984)*, 2003.

[31] H. Q. Fan, S. Kumar, R. Daschner, H. Kübler, and J. P. Shaffer. Subwavelength microwave electric-field imaging using Rydberg atoms inside atomic vapor cells. *Opt. Lett.*, 39(10):3030–3033, May 2014.

[32] Harald Kübler Jiteng Sheng James P. Shaffer Santosh Kumar, Haoquan Fan. Atom-based sensing of weak radio frequency electric fields using homodyne readout. *arXiv:1610.09550*, October 2016.

[33] J. A. Sedlacek, A. Schwettmann, H. Kübler, and J. P. Shaffer. Atom-based vector microwave electrometry using rubidium Rydberg atoms in a vapor cell. *Phys. Rev. Lett.*, 111:063001, Aug 2013.

[34] Christopher L. Holloway David A. Anderson Stephanie A. Miller Matt T. Simons, Joshua A. Gordon and Georg Raithel. Using frequency detuning to improve the sensitivity of electric field measurements via electromagnetically induced transparency and Autler-Townes splitting in rydberg atoms. *Applied Physics Letters*, 108(17), 2016.

[35] D. A. Anderson and G. Raithel. Continuous-frequency measurements of high-intensity microwave electric fields with atomic vapor cells. In Preparation, 2017.

[36] D. Barredo, H. Kübler, R. Daschner, R. Löw, and T. Pfau. Electrical readout for coherent phenomena involving Rydberg atoms in thermal vapor cells. *Phys. Rev. Lett.*, 110:123002, Mar 2013.

[37] Jens Grimmel, Markus Mack, Florian Karlewski, Florian Jessen, Malte Reinschmidt, Nóra Sándor, and József Fortágh. Measurement and numerical calculation of rubidium Rydberg stark spectra. *New Journal of Physics*, 17(5):053005, 2015.

[38] Danielle A. Braje, Vlatko Balić, Sunil Goda, G. Y. Yin, and S. E. Harris. Frequency mixing using electromagnetically induced transparency in cold atoms. *Phys. Rev. Lett.*, 93:183601, Oct 2004.

[39] Jason J. Clarke, William A. van Wijngaarden, and Hongxin Chen. Electromagnetically induced transparency using a vapor cell and a laser-cooled sample of cesium atoms. *Phys. Rev. A*, 64:023818, Jul 2001.

[40] K J Weatherill, J D Pritchard, R P Abel, M G Bason, A K Mohapatra, and C S Adams. Electromagnetically induced transparency of an interacting cold Rydberg ensemble. *Journal of Physics B: Atomic, Molecular and Optical Physics*, 41(20):201002, 2008.

[41] D Steck. Rb D line data. *available online at http://steck. us//alkalidata (Revision 2.1. 4, 23 December 2010)*, 85.

[42] Matt T. Simons, Joshua A. Gordon, and Christopher L. Holloway. Simultaneous use of Cs and Rb Rydberg atoms for dipole moment assessment and RF electric field measurements via electromagnetically induced transparency. *Journal of Applied Physics*, 120(12):123103, 2016.

[43] Yuechun Jiao, Xiaoxuan Han, Zhiwei Yang, Jingkui Li, Georg Raithel, Jianming Zhao, and Suotang Jia. Spectroscopy of cesium Rydberg atoms in strong radio-frequency fields. *Phys. Rev. A*, 94:023832, Aug 2016.

[44] Christopher J Foot. *Atomic physics*, volume 7. Oxford University Press, 2005.

[45] Paul R. Berman and Vladimir S. Malinovsky. *Principles of Laser Spectroscopy and Quantum Optics*. 2011.

[46] Daryl W Preston. Doppler-free saturated absorption: Laser spectroscopy. *American Journal of Physics*, 64(11):1432–1436, 1996.

[47] E. Hansis, T. Cubel, J.-H. Choi, J. R. Guest, and G. Raithel. Simple pressure-tuned fabryprot interferometer. *Review of Scientific Instruments*, 76(3):033105, 2005.

[48] Armen Sargsyan, David Sarkisyan, Ulrich Krohn, James Keaveney, and Charles Adams. Effect of buffer gas on an electromagnetically induced transparency in a ladder system using thermal rubidium vapor. *Phys. Rev. A*, 82:045806, Oct 2010.

[49] R. R. Jones and T. F. Gallagher. Autoionization of Ba $6p_{1/2}$nk states in static and microwave fields below the Inglis-Teller limit. *Phys. Rev. A*, 39:4583–4590, May 1989.

[50] S. H. Autler and C. H. Townes. Stark effect in rapidly varying fields. *Phys. Rev.*, 100:703–722, Oct 1955.

[51] J. R. Boon, E. Zekou, D. McGloin, and M. H. Dunn. Comparison of wavelength dependence in cascade-, Λ-, and vee-type schemes for electromagnetically induced transparency. *Phys. Rev. A*, 59:4675–4684, Jun 1999.

[52] Rajiv Boddeda, Imam Usmani, Erwan Bimbard, Andrey Grankin, Alexei Ourjoumtsev, Etienne Brion, and Philippe Grangier. Rydberg-induced optical nonlinearities from a cold atomic ensemble trapped inside a cavity. *Journal of Physics B: Atomic, Molecular and Optical Physics*, 49(8):084005, 2016.

[53] Bibhas K Dutta and Prasanta K Mahapatra. Nonlinear optical effects in a doubly driven four-level atom. *Physica Scripta*, 75(3):345, 2007.

[54] S. N. Sandhya and K. K. Sharma. Atomic coherence effects in four-level systems: Doppler-free absorption within an electromagnetically-induced-transparency window. *Phys. Rev. A*, 55:2155–2158, Mar 1997.

[55] Robert J Barker and Edl Schamiloglu. *High-power microwave sources and technologies*. Wiley-IEEE Press, 2001.

[56] S. Yoshida, C. O. Reinhold, J. Burgdörfer, S. Ye, and F. B. Dunning. Photoexcitation of $n \simeq 305$ Rydberg states in the presence of an rf drive field. *Phys. Rev. A*, 86:043415, Oct 2012.

[57] Haoquan Fan, Santosh Kumar, Jiteng Sheng, James P. Shaffer, Christopher L. Holloway, and Joshua A. Gordon. Effect of vapor-cell geometry on Rydberg-atom-based measurements of radio-frequency electric fields. *Phys. Rev. Applied*, 4:044015, Oct 2015.

[58] T. Baluktsian R. Löw H. Kübler, J. P. Shaffer and T. Pfau. Coherent excitation of rydberg atoms in micrometre-sized atomic vapour cells. *Nature Photonics*, 4.

[59] T. G. Euser N. Y. Joly T. Pfau P. St. J. Russell G. Epple, K. S. Kleinbach and R. Löw. Rydberg atoms in hollow-core photonic crystal fibres. *Nature Communications*, 5.

[60] Ravi Kumar, Vandna Gokhroo, Kieran Deasy, and Síle Nic Chormaic. Autler-Townes splitting via frequency up-conversion at ultralow-power levels in cold ^{87}Rb atoms using an optical nanofiber. *Phys. Rev. A*, 91:053842, May 2015.

[61] R. Daschner, H. Kübler, R. Löw, H. Baur, N. Frühauf, and T. Pfau. Triple stack glass-to-glass anodic bonding for optogalvanic spectroscopy cells with electrical feedthroughs. *Applied Physics Letters*, 105(4):041107, 2014.

[62] M. Haas, U. D. Jentschura, and C. H. Keitel. Comparison of classical and second quantized description of the dynamic stark shift. *American Journal of Physics*, 74(1), 2006.

[63] L. Sirko, M. Arndt, P. M. Koch, and H. Walther. Microwave ionization of Rb Rydberg atoms: Frequency dependence. *Phys. Rev. A*, 49:3831–3841, May 1994.

[64] Myron L. Zimmerman, Michael G. Littman, Michael M. Kash, and Daniel Kleppner. Stark structure of the Rydberg states of alkali-metal atoms. *Phys. Rev. A*, 20:2251–2275, Dec 1979.

[65] M. G. Bason, M. Tanasittikosol, A. Sargsyan, A. K. Mohapatra, D. Sarkisyan, R. M. Potvliege, and C. S. Adams. Enhanced electric field sensitivity of rf-dressed Rydberg dark states. *New Journal of Physics*, 12(6):065015, 2010.

[66] M. Tanasittikosol and R. M. Potvliege. Sidebands shifts and induced sidebands in rf-dressed Rydberg systems. *arXiv:1206.5951v1*, June 2012.

[67] Y. Zhang, M. Ciocca, L.-W. He, C. E. Burkhardt, and J. J. Leventhal. Floquet spectroscopy of hydrogenic states: Classical and quantum descriptions. *Phys. Rev. A*, 50:4608–4617, Dec 1994.

[68] Rachel Elizabeth Sapiro. *Bose-Einstein Condensate Experiments in Optical Lattices*. PhD thesis, University of Michigan, 2010.

[69] David Alexander Anderson. *Rydberg Molecules and Circular Rydberg states in Cold Atom Clouds*. PhD thesis, University of Michigan, 2015.

[70] Andrew D. Schwarzkopf. *Imaging Spatial Correlations of Rydberg Excitations in Cold Atom Clouds*. PhD thesis, University of Michigan, 2013.

[71] A. Schwarzkopf, R. E. Sapiro, and G. Raithel. Imaging spatial correlations of Rydberg excitations in cold atom clouds. *Phys. Rev. Lett.*, 107:103001, Aug 2011.

[72] N. Thaicharoen, L. F. Gonçalves, and G. Raithel. Atom-pair kinetics with strong electric-dipole interactions. *Phys. Rev. Lett.*, 116:213002, May 2016.

[73] Chuck McManis. H-bridge theory and practice; Chuck's robotics notebook, Dec 2006.

[74] F. Robicheaux and J. V. Hernández. Many-body wave function in a dipole blockade configuration. *Phys. Rev. A*, 72:063403, Dec 2005.

[75] A. Schwarzkopf, D. A. Anderson, N. Thaicharoen, and G. Raithel. Spatial correlations between Rydberg atoms in an optical dipole trap. *Phys. Rev. A*, 88:061406, Dec 2013.

[76] ISOMET CORP. 1205c-x-804b acousto-optic modulator.

[77] Lukas Novotny and Bert Hecht. *Principles of nano-optics*. Cambridge university press, 2012.

[78] Nithiwadee Thaicharoen. *Spatial Imaging of Strongly Interacting Rydberg Atoms*. PhD thesis, University of Michigan, 2017.

[79] A. Schwarzkopf N. Thaicharoen and G. Raithel. Control of spatial correlations between Rydberg excitations using rotary echo. *arXiv:1607.01398*, July 2016.

[80] Rydberg Technologies LLC.

[81] L. Ma, D.A. Anderson, and G. Raithel. Paschen-Back effect and Rydberg-state diamagnetism in vapor-cell electromagnetically induced transparency. *arXiv preprint arXiv:1702.05556*, 2017.

[82] Linjie Zhang, Shanxia Bao, Hao Zhang, and Georg Raithel. Nonlinear Zeeman effect in electromagnetically induced transparency. *arXiv preprint arXiv:1702.04842*, 2017.

[83] D. A. Anderson, S. A. Miller, and G. Raithel. Photoassociation of long-range nD Rydberg molecules. *Phys. Rev. Lett.*, 112:163201, Apr 2014.

[84] D. A. Anderson, S. A. Miller, and G. Raithel. Angular-momentum couplings in long-range Rb_2 Rydberg molecules. *Phys. Rev. A*, 90:062518, Dec 2014.